



Universität Hamburg
DER FORSCHUNG | DER LEHRE | DER BILDUNG

Master Thesis

Laboratory and Simulation studies of Pulse Shape Discrimination in pure CsI and CsI(Tl)

Munira Khan

Studiengang Physik M. Sc.

Matr.-Nr. 6894864

Erstgutachterin: Professor Dr. Kerstin Tackmann

Zweitgutachter: Professor Dr. Torben Ferber

Abgabefrist: 14.10.2021

Contents

1	Introduction	7
2	Physics Motivation	9
2.1	Standard Model of particle physics	9
2.2	Caesium iodide calorimeters in particle physics experiments	11
2.2.1	CP violation in kaons at the KOTO experiment	11
2.2.2	PSD for improved particle identification at Belle II	13
3	Electromagnetic calorimeter theory	17
3.1	Particles passage through matter	17
3.1.1	Heavy charged particles	18
3.1.2	Neutron interactions with matter	19
3.2	Scintillation detectors	21
3.2.1	Scintillators	21
3.3	The Belle II Electromagnetic Calorimeter	24
4	Experimental setup	27
4.1	Detector assembly	28
4.2	Obtaining of neutron data samples	32
5	Pure CsI simulation studies in GEANT4	35
5.1	Detector construction	35
5.2	Event Generation	36

6	Waveform analysis	41
6.1	Waveform processing	41
6.2	Preselection	43
6.3	Energy calibration	48
7	Pulse shape discrimination	55
7.1	Energy spectra recorded at XFEL	55
7.2	Charge ratio method in CsI(Tl)	57
7.3	Optimization of short time window in pure CsI	60
7.4	Charge ratio method in pure CsI	68
8	Conclusions and Outlook	73
A	Shielding of the crystal setup	75
B	Short time gate for pure CsI	79

Abstract

In the search for physics beyond the Standard Model, research in particle physics aims to probe particle interactions at high energies and strives for better precision on measurements. Experiments such as Belle II target higher luminosities to push the precision frontier. This requires stable detector performance and reliable identification of particles in environments with a large number of background processes, which leads to growing interest in new detector technologies.

Pure caesium-iodide (CsI) scintillators are characterised by their fast scintillation time and high robustness against radiation, making them a promising calorimeter material. One of the first quantitative studies on the pulse shape discrimination (PSD) capabilities of pure CsI is performed in this thesis with the goal to distinguish electromagnetically and hadronically interacting particles. An experimental setup with a Thallium-doped CsI crystal, which is used at Belle II, and a single pure CsI crystal was designed and commissioned. Measurements near the beam dump of the European XFEL are performed. The charge ratio method, where the pulse shape is characterized based on the ratio of the integrated scintillation light output over different time gates, is applied in the analysis of the recorded data.

It is found that pure CsI has PSD abilities in the probed energy range from 12 to 70 MeV. The separation power to distinguish between muon-like and neutron-like pulse shapes is investigated for various short time gates from 40 to 200 ns to determine the optimal integration time for PSD. The ideal short time gate is found to be at 100 ns, which offers a separation of up to 95% purity between the neutron-like and muon-like samples.

Zusammenfassung

Auf der Suche nach Physik jenseits des Standardmodells zielt die Forschung in der Teilchenphysik darauf ab, Prozesse bei hohen Energien zu untersuchen und eine höhere Messgenauigkeit zu erreichen. Experimente wie Belle II zielen auf höhere Luminositäten ab, um die Präzisionsgrenze zu überschreiten. Dies erfordert stabile Detektorleistung und zuverlässige Teilchenidentifizierung in Umgebungen mit einer großen Anzahl von Hintergrundprozessen. Dies resultiert in wachsendem Interesse an neuen Detektortechnologien. Reine Cäsium-Iodid (CsI)-Szintillatoren zeichnen sich durch ihre schnelle Szintillationszeit und hohe Robustheit gegenüber Strahlung aus, was sie zu einem vielversprechenden Kalorimetermaterial macht. In dieser Arbeit wird eine der ersten quantitativen Studien zur Pulsformunterscheidung (PSD) mit reinem CsI durchgeführt, mit dem Ziel, elektromagnetisch und hadronisch wechselwirkende Teilchen zu unterscheiden. Ein Versuchsaufbau mit einem Thallium-dotierten CsI-Kristall, welcher bei Belle II verwendet wird, und einem reinen CsI-Kristall wurde entworfen und in Betrieb genommen. Messungen in der Nähe des Beam Dumps des europäischen XFEL wurden durchgeführt. Bei der Analyse der Daten wird die Ladungsverhältnismethode angewandt, bei der die Pulsform anhand des Verhältnisses der integrierten Szintillationslichtleistung über verschiedene Zeitintervalle charakterisiert wird. Es wird festgestellt, dass reines CsI PSD-Fähigkeiten im untersuchten Energiebereich von 12 bis 70 MeV besitzt. Das Trennvermögen zur Unterscheidung zwischen muon-artigen und neutron-artigen Pulsformen wird für verschiedene kurze Zeitintervalle von 40 bis 200 ns untersucht, um die optimale Integrationszeit für PSD zu bestimmen. Das ideale kurze Zeitintervall liegt bei 100 ns, was eine Trennung von bis zu 95% Reinheit zwischen den muon-artigen und neutron-artigen Proben ermöglicht.

Disclaimer

The pulse shape discrimination studies presented in this thesis were proposed to me by my supervisors, Prof. Dr. Torben Ferber and Dr. Savino Longo. The planning of the experimental setup and the measurement campaigns at XFEL was done according to the proposal of Prof. Dr. Torben Ferber, Dr. Savino Longo and Dr. Belina von Krosigk.

The housing of the experimental setup was designed by Kasten Gadow and his team at DESY. Figure 4.4 was done by him. The studies of the neutron flux at the measurement location in Section 4.2 were carried out by Dr. Taiee Liang, Dr. Albrecht Leuschner, Dr. M. Schmitz, Dr. Norbert Tesch. The Figures 4.6, 4.6 and 4.7 were produced by Taiee Liang.

The t_0 algorithm described in Section 6.2 was done based on the ideas and data processing of Sukeerthi Dharani. The preselection criteria were designed by Sukeerthi Dharani and me. The template seen in Figure 7.11 was also done by Sukeerthi Dharani.

All results are worded by me and all pictures are produced by me, unless otherwise specified.

Chapter 1

Introduction

Scintillators emit light in the visible or UV spectrum when an incoming particle deposits energy within them. Due to this property, they are often used as calorimeter material for particle physics experiments. Among many typical applications, such as energy and timing measurements, calorimeters can serve the purpose of particle identification. The Belle II experiment is the first high energy particle physics experiment that implemented pulse shape discrimination (PSD) in its CsI(Tl) electromagnetic calorimeter as novel technique to improve particle identification [1].

For future particle physics experiments, it is of interest to study the PSD properties of other scintillators and whether currently used techniques can be applied to them as well. Pure CsI shows a very fast scintillation decay time of 16 ns and robust performance in the presence of high radiation [2], which makes it a promising option for experiments e.g. the Mu2e experiment [3]. The KOTO experiment has recently implemented PSD in its pure CsI calorimeter [4]. In this thesis, PSD properties of pure CsI are further investigated. For this purpose, a test setup was designed and commissioned to record data for pulse shape analysis. The detector setup was operated close to a beam dump of the European XFEL, which offered a sample of high energetic neutrons that were to be differentiated from the flux of cosmic muons. The measurements of the experimental setup are compared to a simulation of the pure CsI.

Chapter 2 offers an overview on the Standard Model of particle physics and introduces the Belle II electromagnetic calorimeter which uses CsI(Tl) in comparison with

other experiments that use a pure CsI calorimeter. Chapter 3 describes the theoretical background of calorimeters, specifically of scintillation detectors. Specifications on the experimental setup used for the studies of PSD properties in pure CsI and CsI(Tl) are given in chapter 4. An overview of simulation studies with a single pure CsI crystal that were done in GEANT4 is given in chapter 5. The processing of the raw data and a preselection of waveform events is described in chapter 6. Chapter 7 displays the results of the PSD studies in the CsI(Tl) and pure CsI, based on the charge ratio method. It is found that pure CsI has PSD abilities which are optimized by adjusting the short time gate. Finally, chapter 8 gives a summary of the results of this thesis.

Chapter 2

Physics Motivation

2.1 Standard Model of particle physics

Elementary particles are the smallest known building blocks of nature. The Standard Model of particle physics is the established model to describe elementary particles. It has been experimentally verified to a very high precision over the past decades. This chapter gives a short introduction to the Standard Model, based on [5]. The Standard Model classifies particles based on their properties and how they interact with each other. Each particle is characterized by its spin, its mass, and its charge. This is shown in Figure 2.1.

Bosons have integer spin and are the mediators of fundamental interactions between fermions. The electromagnetic force is mediated by photons, the weak force by W^\pm and Z^0 , and the strong force by gluons. Particles are able to interact with a force if they have the corresponding charge. All fermions besides neutrinos have electromagnetic charge, so they can all interact electromagnetically. Only gluons couple to color charge, so only quarks interact through the strong force. The electromagnetic and weak interaction can be combined to the electroweak interaction. W^\pm and Z^0 couple to hypercharge, which is carried by all fermions.

Fermions have half integer spin and are classified into two types: quarks and leptons. Quarks exist in six flavour states that are differentiated into up-type, with electrical charge of $+\frac{2}{3}e$, and down-type, with charge $-\frac{1}{3}e$. Free quarks have never been ob-

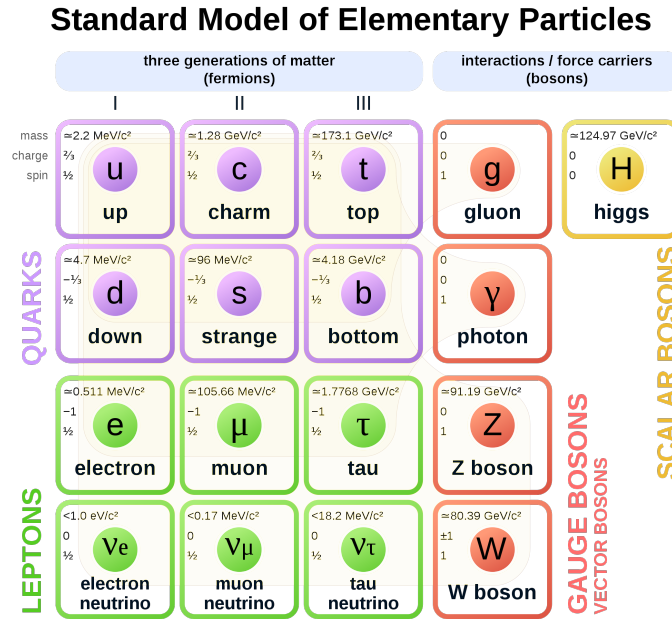


Figure 2.1: The particles of the Standard Model, listed with their respective spin, mass and charge. From [6].

served due to color confinement of the strong force. They can only be observed in bound states as hadrons. The most common hadrons are the proton and neutron, the components of an atomic nucleus. Hadrons can be further classified as mesons, bound states of a quark and its anti-quark, or as baryons, which are constellations of three or more quarks.

The remaining fermions are the charged leptons (electron, muon, tau) with electric charge $-1e$ and their corresponding neutrinos which all have an electric charge of 0. Due to their very small mass and lack of electrical or color charge, neutrinos can only interact through weak interactions, while charged leptons can also interact via the electromagnetic force. In this thesis, the differences in the behaviour of hadronic particles and electromagnetically interacting particles are studied.

The Standard Model is not a complete theory, as many open questions still cannot be answered. One of the unanswered phenomena is the problem of matter-antimatter asymmetry that originated on observations of Charge-Parity (CP) violation [5]. Another open question is the long standing discrepancy between the Standard Model prediction and experimental measurements of the anomalous magnetic moment $g - 2$

of the muon [7]. Current research is therefore dedicated to look for physics beyond the Standard Model to solve these questions. In the following section, the KOTO experiment, which studies processes on CP violation, and measurements that have an impact on the anomalous magnetic moment $g - 2$ of the muon will be discussed. A common point of these experiments is that they apply pulse shape discrimination in their respective pure CsI or CsI(Tl) calorimeter.

2.2 Caesium iodide calorimeters in particle physics experiments

Research and development on current detector designs is of interest for the search of physics beyond Standard Model. New techniques to improve particle identification and methods to discriminate between signal events and background interactions in detector material are a central issue as the experiments move to higher energies or to higher precision. The following section provides an outline of the research of experiments that use pulse shape discrimination (PSD) in their caesium iodide calorimeters. The KOTO experiment uses a calorimeter made of pure caesium iodide (CsI) [8]. They have recently implemented PSD to improve separation of signal photons and background neutrons [4]. The Belle II experiment uses a calorimeter with thallium-doped caesium iodide (CsI(Tl)) and applies PSD there [1]. Furthermore, the upcoming Mu2e experiment will use a pure CsI calorimeter [3].

2.2.1 CP violation in kaons at the KOTO experiment

The KOTO experiment is located at the Hadron Experimental Facility of Japan Proton Accelerator Research Complex (J-PARC). It studies the CP violation of kaons in the process $K_L \rightarrow \pi^0 \nu \bar{\nu}$, searching for new processes beyond the Standard Model that would break the CP symmetry [8]. CP violation can arise in the Standard Model, but it is not large enough to account for the observed matter-antimatter asymmetry observed in the universe.

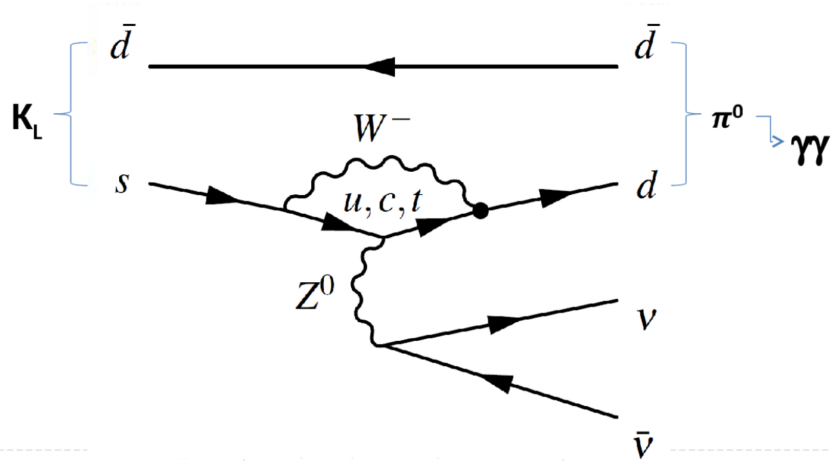


Figure 2.2: Feynman diagram of $K_L \rightarrow \pi^0 \nu \bar{\nu}$. An up-type quark mediates the decay of a strange quark to a down quark through a loop process [9].

The process $K_L \rightarrow \pi^0 \nu \bar{\nu}$ occurs when the strange quark of the kaon decays to a down quark through a loop process, as seen in Figure 2.2. It is very rare according to Standard Model predictions. Deviations from this prediction could show hints towards processes of physics beyond the Standard Model. The KOTO collaboration performs high precision measurements of the branching fraction of this process. The current experimental limit at $\text{BR}(K_L \rightarrow \pi^0 \nu \bar{\nu}) < 3.0 \times 10^{-9}$ at a 90% confidence level was set by KOTO from the data collected in 2015 [10]. To obtain the K_L beam, a 30 GeV proton beam is striking a fixed gold target, producing a neutral beam after the charged particles are filtered away by a collimator and sweeping magnets [9].

The pure CsI calorimeter of the KOTO experiment consists of a hermetic system of scintillating veto detectors and a pure CsI calorimeter. The fast decay component of pure CsI allows for the reduction of pileup of the signal and makes it possible to separate two pulses with more than 30 ns time difference [11]. The signature of $K_L \rightarrow \pi^0 \nu \bar{\nu}$ is a pair of photons from the π^0 decay that have a finite transverse momentum due to the momentum carried away by the pair of neutrinos. Neutron interactions with detector material are one of the main backgrounds to this process [8].

PSD has been implemented in the pure CsI calorimeter as method to improve the separation of signal photons and the neutron background [4]. According to their study, pure CsI had been reported to have capabilities for PSD of photons and neutrons with

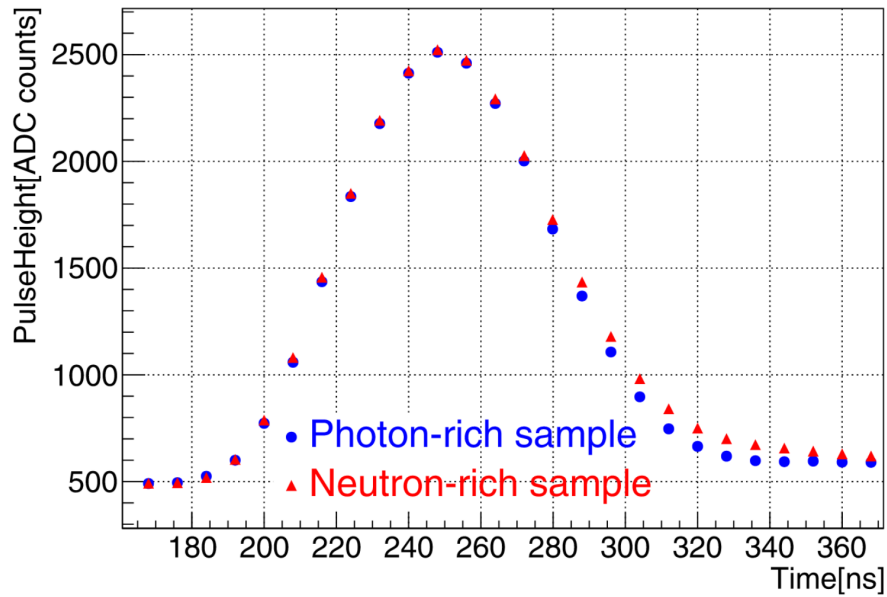


Figure 2.3: Comparison of two typical waveforms in the KOTO calorimeter, from [4]. Blue circles are from a photon-rich sample, while red triangles are from a neutron-rich sample.

up to 45 MeV, but their results now observe pulse shape differences for energies between 0.05 GeV to 0.5 GeV in a single crystal.

When comparing the waveforms of a photon-rich sample with a neutron-rich sample, the waveform from the neutron-rich sample shows a larger tail component. This difference is utilized to perform PSD. Possible origins for the pulse shape differences are assumed to be scintillation processes or differences in the profile of the shower [4]. This thesis presents a study of the performance of PSD on single crystal level with the aim to perform the first quantitative study of the scintillation processes within single pure CsI crystals.

2.2.2 PSD for improved particle identification at Belle II

The Belle II experiment uses an electromagnetic calorimeter consisting of 8736 CsI(Tl) crystals that were originally used in the Belle experiment. A detailed description of the Belle II calorimeter is given in section 3.3 of this thesis.

Many physics analyses at Belle II can benefit from improved particle identification. An example of an analysis that relies on good particle identification is the measurement

of the cross-section of $e^+e^- \rightarrow \pi\pi\gamma$. This process requires a good discrimination of the signal pions against a muon background. The process is relevant to the theoretical predictions of the anomalous magnetic moment of the muon a_μ .

As the muon carries spin \vec{s} and electromagnetic charge e , it has a magnetic moment \vec{M}_μ ,

$$\vec{M}_\mu = g_\mu \frac{e}{2m_\mu} \vec{s} \quad (2.1)$$

with the muon mass m_μ and the g -factor g , which indicates the magnetic strength of the muon and gives information on its rotation quantities [5]. Based on the Dirac equation of relativistic quantum mechanics, the g -factor for elementary particles with spin $\frac{1}{2}$ should be equal to 2. Small corrections to this value are predicted, based on quantum vacuum fluctuations [12]. These corrections are called the *anomalous magnetic moment* and are related to the g -factor as $a_\mu = \frac{(g_\mu - 2)}{2}$.

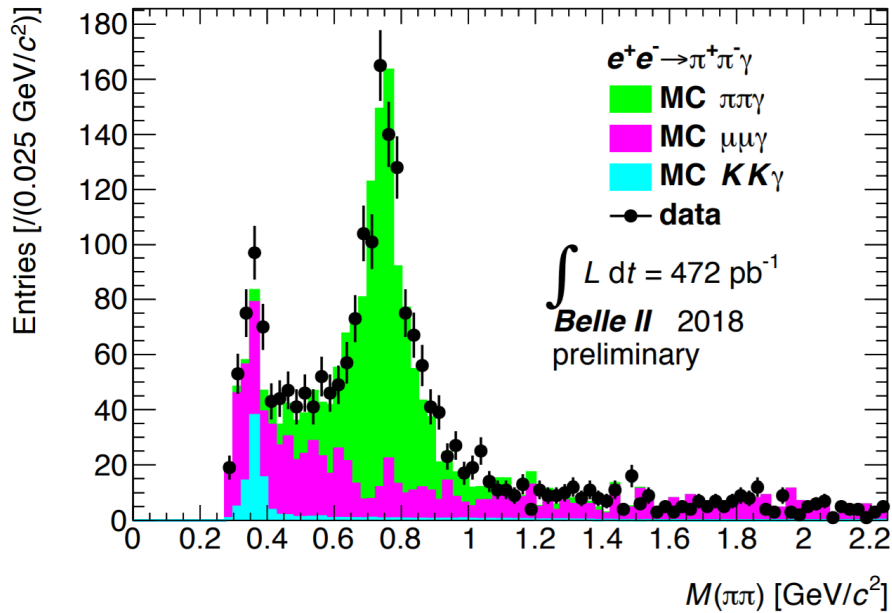


Figure 2.4: Mass spectrum of two pions using 2018 Belle II data sets. It is compared to the Monte Carlo simulation of the signal and the main backgrounds $ee \rightarrow \mu\mu\gamma$ and $ee \rightarrow KK\gamma$, [13].

The $g-2$ experiment at Fermilab, which was originally performed at Brookhaven, gives a very precise measurement of the experimental value of a_μ . On April 7, 2021, Fermilab presented new results, showing an discrepancy of 4.2σ [7]. Further results with more

data are anticipated, but to resolve the discrepancy, it is also necessary to improve the uncertainty on the theoretical prediction.

Various factors influence the SM predictions of a_μ . A detailed description of $g-2$ in the SM is given in [12]. The dominant contribution of the Standard Model prediction for uncertainty of a_μ comes from the hadronic vacuum polarisation (HVP). The value of the HVP can be expressed through the production cross-section for various processes of e^+e^- going to hadrons. Contributions from light hadrons dominate this calculation. As for data-driven methods to determine HVP, it can be extracted from the cross-section of $ee \rightarrow \pi\pi$ which, in the Standard Model, is the same as $\mu\mu \rightarrow \pi\pi$ due to lepton universality.

An established approach to performing this analysis that will be applied at Belle II is the initial state radiation (ISR) method in order to indirectly scan the center-of-mass energy. The electron or positron emit a photon before the annihilation, which then leads to a decreased collision energy. This makes it possible to scan a whole region of energies below the fixed beam energy. The most precise ISR measurements of the $\pi^+\pi^-$ cross-section have been done by KLOE and BABAR [12]. Preliminary results of the analysis at Belle II can be seen in Figure 2.4, which shows the invariant mass spectrum of two charged particles which were assigned with the pion mass. A large background comes from the process $e^+e^- \rightarrow \mu\mu\gamma$, which is a main challenge in the $e^+e^- \rightarrow \pi\pi\gamma$ measurement. The particle identification of pions and muons has been a main factor of uncertainty in the ISR measurements at the BaBar experiment [14, 15]. Therefore good particle identification is needed to reduce this background and lower the systematic uncertainties. In case of the The electromagnetic calorimeter can contribute to improving the particle identification.

In 2018, the Belle II experiment became the first e^+e^- collider in high energy physics to implement PSD as method to improve particle identification with its CsI(Tl) calorimeter [1]. The example of two waveforms recorded by the Belle II calorimeter can be seen in Figure 2.5.

In general, the high levels of beam-induced backgrounds in collider experiments becomes a challenge as existing experiments move to higher luminosity. Pure CsI ex-

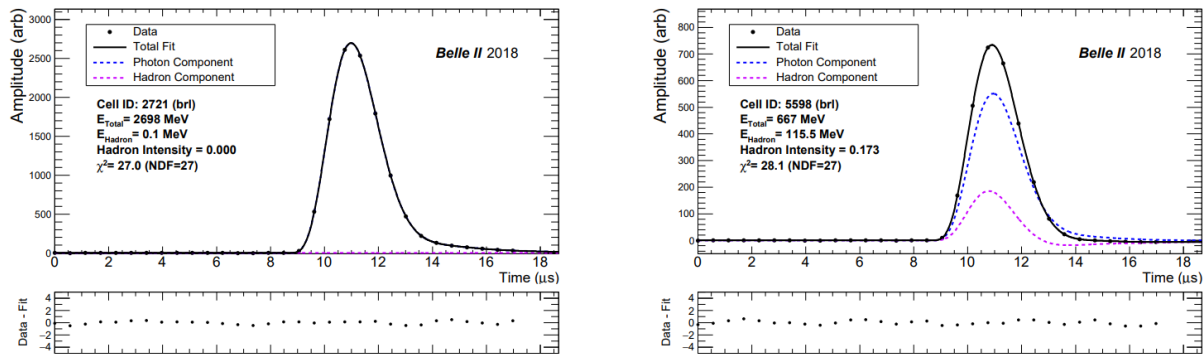


Figure 2.5: Typical waveforms from Belle II fitted with a photon and hadron template. The left figure shows a waveform of an electromagnetic interaction and negligible hadron component. The right side shows the waveform of a hadronic interaction. From [1]

hibits a fast scintillation time in the order of nanoseconds and shows robust performance with high beam-induced backgrounds [2]. As Belle II strives to reach a higher luminosity, pure CsI has been proposed as a candidate for a possible calorimeter upgrade [16]. Due to its fast scintillation time, the pile-up of beam-induced background could be reduced. However due to its low light yield and emission maximum in the UV-range, new electronics for the optical read-out would be required. The replacement of the crystals therefore would be very expensive. Nevertheless, the Belle II collaboration is doing various studies on pure CsI as scintillator material.

Chapter 3

Electromagnetic calorimeter theory

In particle physics, a calorimeter is a detector with the main task of measuring the energy of particles and the direction of electromagnetic or hadronic showers [17]. Particles entering the calorimeter interact with its material, leaving energy deposits within the material.

This chapter first discusses of how particles lose their energy through interactions with matter. Scintillation detectors are then introduced as a way to measure these energy losses. The last section gives an overview of the Belle II experiment and its electromagnetic calorimeter, which is made up of CsI(Tl) scintillator crystals.

3.1 Particles passage through matter

Constructing particle detectors relies on understanding how particles interact with matter as they travel through it. There are a variety of possible interactions, depending on the particle type, its energy, and the material it is going through. All of these processes are discussed in detail in literature, such as [17] and [18].

Electromagnetic interactions are the common processes for charged particles and photons. This frequently takes place through inelastic collisions with atomic electrons. Neutrons interact via the strong force in most cases [18].

In the following section, the interactions of heavy charged particles, such as muons, and the interactions of neutrons are discussed.

3.1.1 Heavy charged particles

In the energy regions of few keV and higher, charged particles generally interact via two characteristic processes when they travel through matter:

1. Energy loss of the particle occurs due to inelastic collisions with atomic electrons of the material.
2. The particle elastically scatters from the atomic nuclei of the material, changing its direction of flight.

Other possible processes, such as the emission of Cherenkov radiation, bremsstrahlung or nuclear reactions, can occur too. However compared to the first two, these are much more rare [18].

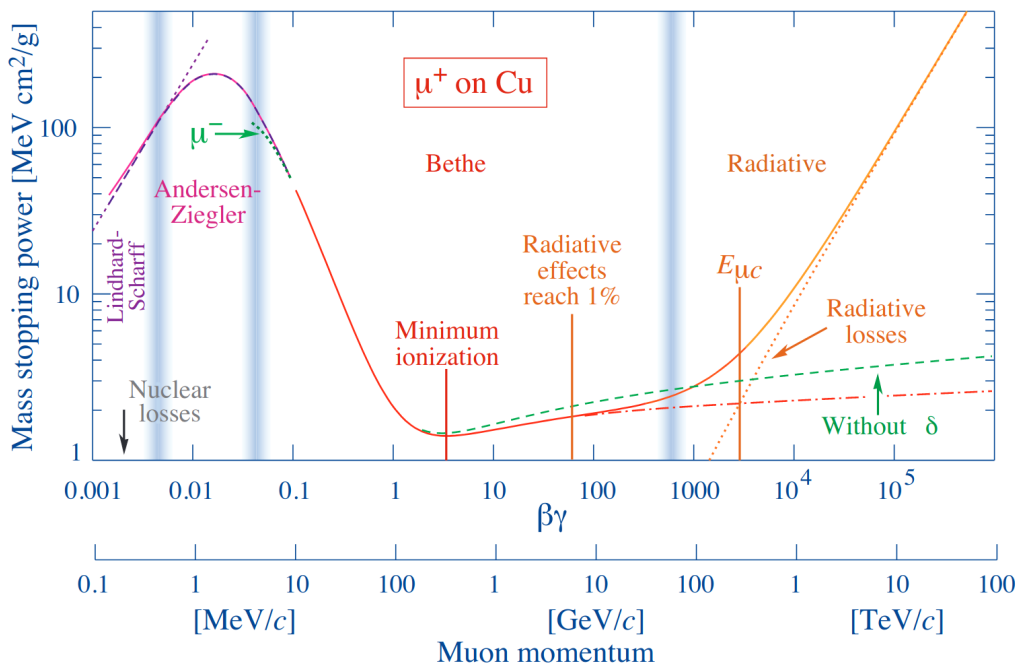


Figure 3.1: Muon interactions in copper as function of the muon's momentum [17].

Heavy charged particles refers to particles with masses higher than the electron mass, such as muons, pions or protons. These particles mainly lose their energy through inelastic collision, leading to ionization or excitation of the atoms in the material. Only

a small fraction of the particle's total kinetic energy is transferred in a single collision [18]. However due to the density of matter, a large number of collisions per unit path length can take place. The sum of these collisions results in a high energy loss. Elastic collisions with nuclei occur frequently too, but since the mass of nuclei in the material is much higher than the mass of the particle, only little energy is transferred.

During the ionization process, a charged particle transfers energy to an atomic electron, which is then freed. In general, the energy loss in inelastic collisions for moderately relativistic charged heavy particles is described by the Bethe-Bloch equation [18]:

$$\left\langle -\frac{dE}{dx} \right\rangle = Kz^2 \frac{Z}{A} \frac{1}{\beta^2} \left[\frac{1}{2} \ln \frac{2m_e c^2 \beta^2 \gamma^2 W_{max}}{I^2} - \beta^2 - \frac{\delta(\beta\gamma)S}{2} \right], \quad (3.1)$$

with $K = 4\pi N_A r_e^2 m_e c^2$, Avogadro's number N_A , the classical electron radius r_e , the electron mass m_e , the speed of light c , the charge of the incident particle z , the atomic number of the material Z , the atomic mass of the material A , the speed of the incident particle β , the mean excitation energy of the material I , and as the maximum energy transfer in a single collision W_{max} .

Equation 3.1 is valid in the region $0.1 \lesssim \beta\gamma \lesssim 1000$ [17]. It shows how the energy loss through ionization depends on various properties of the incident particle and the material [17]. For muons, Figure 3.1 shows the stopping power $\langle -\frac{dE}{dx} \rangle$ in copper with respect to the muon's energy [17]. Charged particles at low energies mainly lose their energy through bremsstrahlung, while at higher energies, ionization becomes the dominant process. There is a critical energy E_c where $(\frac{dE}{dx})_{brems} = (\frac{dE}{dx})_{ionization}$ [2].

3.1.2 Neutron interactions with matter

Neutron interactions are mostly limited to interactions with the nuclei via the strong force, since neutrons carry no electric charge. These interactions occur rarely due to the short range of the strong force. Neutrons can therefore often pass through matter without reactions.

The mean free path length of a neutrons is given by

$$\frac{1}{\lambda} = N\sigma_{tot} = \frac{N_A\rho}{A}\sigma_{tot} \quad (3.2)$$

where σ_{tot} is total probability for a neutron to interact with matter in units of cm^{-1} and ρ is the material density.

A beam of collimated neutrons going through matter will get weakened according to

$$N = N_0 \exp(-x/\lambda) \quad (3.3)$$

where x is the thickness of the material.

There are a variety of processes that can occur when a neutron interacts with matter, depending on the neutron's energy.

1. **Scattering:** This can happen as elastic or inelastic process. *Elastic scattering* takes place between the incoming neutron and an atomic neutron, no atomic excitation takes place. This is the main source of energy loss for neutrons in the MeV region. During *inelastic scattering*, the incoming neutron passes energy to a neutron or proton within the nucleus, leaving it in an excited state which then later decays e.g. by the emission of a photon [19].
2. **Capture:** In these processes, the neutron is absorbed by the nucleus. This results in a new compound nucleus, which can de-excite in various ways. The cross-section for these processes is roughly proportional to $\frac{1}{v}$ where v is the velocity of the neutron [18]. It is therefore most likely at low energies in the range of eV to keV. *Radiative capture* describes the case where the compound nucleus decays into its ground state by emitting a photon. *Fission* occurs when the compound nucleus splits into lighter nuclei, neutrons and photons. A high amount of energy is released in this process [19].

Since the type of interaction strongly depends on the energy of the neutron, they are classified by their energy. Neutrons with energies around 100 MeV are considered as

highly energetic, while *fast* neutrons have energies around few tens MeV until few hundreds keV. In the region around 100 keV to 0.1 eV neutrons are *epithermal*. At energies around room temperature, neutrons are called *thermal* or *slow*. Neutrons with even lower energies are called *cold* or *ultra-cold*.

3.2 Scintillation detectors

In the previous section, it has been discussed how particles lose energy when passing through matter. To measure the energy deposited within a material, it is necessary to produce an electric signal that behaves in correlation to the energy loss.

In a scintillation detector, the scintillator emits light in the visible spectrum or UV range when it is struck by an incoming particles. The scintillator is optically coupled to an electric light sensor. The light sensor, e.g. a photomultiplier tube (PMT) or a photodiode, amplifies the photons emitted by the scintillator and turns them into an electrical signal. This makes it possible to measure the energy loss of the particles.

3.2.1 Scintillators

Scintillators are materials that emit light after absorbing energy. They are classified as organic or inorganic. Organic scintillators have a high light output and very rapid decay times in the order of few nanoseconds. However, they show poor linearity when converting energy deposits to light. Their typical application lies in triggering to get accurate timing information when a particle hits the scintillator. Inorganic scintillators are typically used to measure energy deposits from incoming particles. Inorganic scintillators are generally slower and have varying light yields. However they have high density, which gives them a greater stopping power. Combined with a high light output, this results in a good energy resolution. They are suitable for the detection of photons and high energy electrons and positrons [18].

The scintillation mechanism of organic scintillators is based on molecular excitations. In inorganic scintillators, it is due to the electronic band structure of the crystal lattice

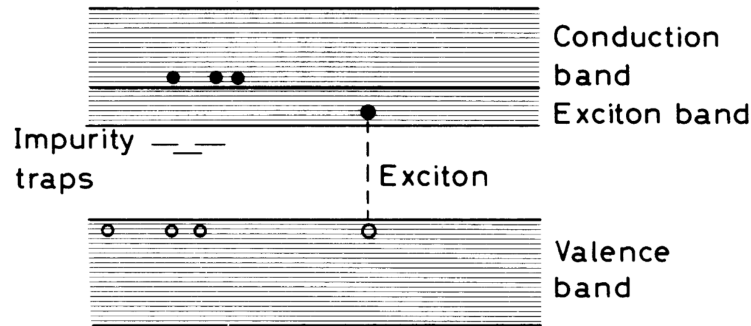


Figure 3.2: Band structure of a typical organic crystal. Excitons, which are loosely coupled electron-hole pairs move through the crystal and can be captured in luminescent centers [18].

as seen in Figure 3.2. An incoming particle leads to the excitation of an electron from the valence band up to the conduction band. The ionization leads to a free electron and free hole. The excitation can also happen to a band just below the conduction band, the exciton band. This state behaves like a loosely coupled electron-hole pair, which can freely move through the crystal. If these meet a luminescent center of the crystal, energy is transferred, leading to the emission of scintillation photons [17, 18]. The decay time of a scintillator is mainly dominated by the decay time of the luminescent center. Some crystals intrinsically exhibit scintillation properties, while others require the addition of a dopant such as thallium (Tl) to increase the light output [17].

Scintillation signals provide a variety of information. The main applications is to measure the energy of the particle entering the scintillator. The total scintillation light output is directly proportional to the energy deposited within it [18]. Scintillators also provide timing information due to their fast response time and short recovery time that makes it possible to perform precise measurements of time for e.g. fast consecutive events.

Scintillating materials are characterized by their scintillation decay times, light yield and linearity. The number of scintillation photons that are emitted per unit is described by the light yield. The linearity characterizes the relation between the energy deposit and the light output. The scintillation decay times refer to the time it takes for the scintillator to emit 63% of its light after an energy deposit [2].

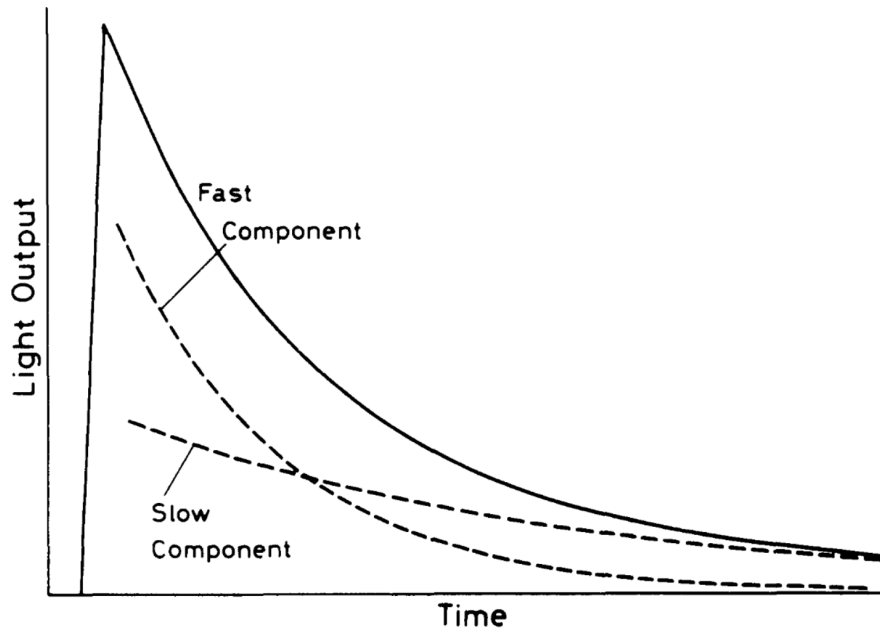


Figure 3.3: The typical time evolution of the light emission in a scintillator [18]. The dashed lines represent the exponential decays of the slow and fast scintillation components. The solid line represents the resulting total scintillation emission.

The number of scintillation photons emitted per time can be expressed as sum of exponential decays with different decay constants

$$N = A \exp\left(\frac{-t}{\tau_f}\right) + B \exp\left(\frac{-t}{\tau_s}\right) \quad (3.4)$$

where N is the number of scintillation photons emitted at time t , τ_f and τ_s are the fast and slow scintillation decay constants and A and B are their relative magnitudes. The scintillation decay constants and their magnitudes depend on the material, but the fast component dominates over the slow in the general case. The relation of these components is seen in Figure 3.3. The existence of multiple decay constant is the core property that allows pulse shape discrimination (PSD).

The scintillation decay constants can also be dependant on the incoming particle's dE/dx , which is the case in CsI(Tl) [20]. If there is a strong dependency, the overall scintillation emission will vary depending on the type of particle that caused the emission of scintillation light. Using this to distinguish between the particle types makes it possible to apply pulse shape discrimination. Pulse shape discrimination refers to the

ability of a scintillator to identify the particle that is responsible for an energy deposit based on the shape of the waveform of the emitted light output. For CsI(Tl), overall decay times of $0.435 \mu\text{s}$ for α -particles, $0.519 \mu\text{s}$ for protons and $0.695 \mu\text{s}$ for electrons are found [18].

3.3 The Belle II Electromagnetic Calorimeter

The Belle II experiment is located at SuperKEKB, an asymmetric e^+e^- collider in the Japanese city Tsukuba. It has a collision energy of 10.58 GeV in the center of mass frame. This energy corresponds to the $\Upsilon(4S)$ resonance, making Belle II a B-factory. Main goals of the experiment are studies of Charge-Parity violation, searches for rare processes or for physics beyond the Standard Model and precision measurements, mainly in the flavour sector of the Standard Model.

Particle collisions happen at the interaction region of the SuperKEKB collider. The detector system is arranged in a cylindrical geometry around the interaction region, as pictured in Figure 3.4. The Belle II detector strives to identify particles that were produced in these collision and therefore measures their tracks, momentum and energy. It consists of several concentric layers of sub-detectors, each of them dedicated to one of these tasks. Detailed descriptions of all Belle II sub-detectors can be found in [22–24]. The electromagnetic calorimeter (ECL) will be discussed here.

The Belle II ECL consists of 8736 thallium doped caesium iodide (CsI(Tl)) crystals. Its main task is to measure the energy of charged particles and photons. These particles interact with the crystals, leading to the emission of scintillation light. The light output of the crystals is directly proportional to the energy deposited in the crystal.

The CsI(Tl) crystals are re-used from the Belle experiment. In the barrel region, they have a trapezoidal geometry with a front face area of $4.5 \times 4.5 \text{ cm}^2$, a rear face area of $5 \times 5 \text{ cm}^2$ and a length of 30 cm , corresponding to around 18 times the radiation length of CsI(Tl), which is at 1.65 cm . The shapes of crystals in the endcap regions are more

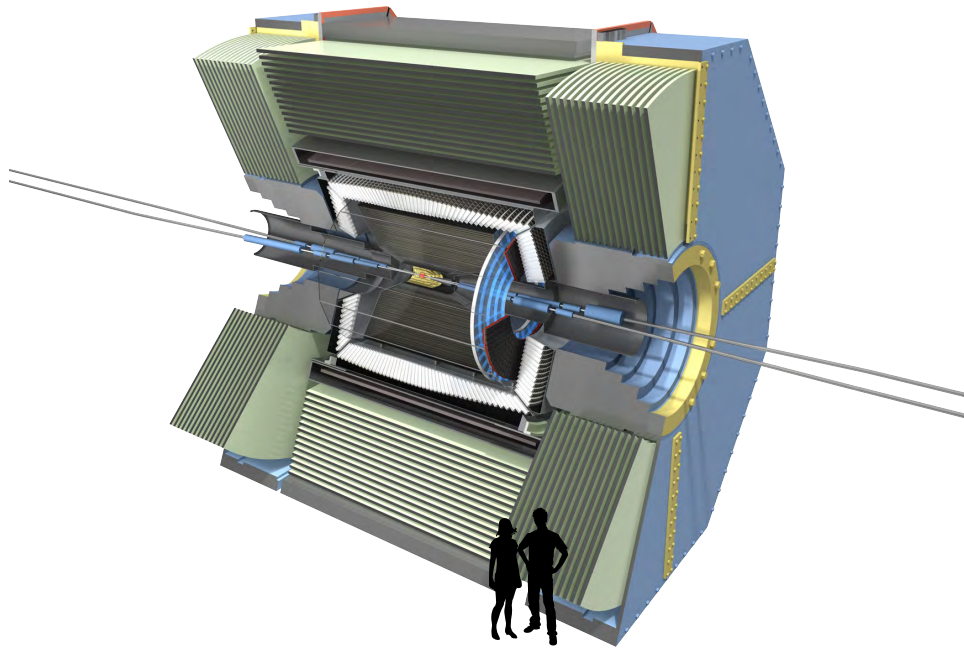


Figure 3.4: The Belle II detector [21]. The interaction point in the center is surrounded by a system of sub-detectors which are, from innermost to outermost, the Pixel Detector, the Vertex Detector, the Central Drift Chamber, Time Of Propagation detector, Aerogel Ring-Imaging Cherenkov detector, the Electromagnetic Calorimeter and finally the K_L -and-Muon system.

complex. In total, the ECL entails 29 different crystal shapes in the barrels and 69 in the endcap regions [16].

Each crystal is wrapped in a $200\ \mu\text{m}$ layer of Teflon and then covered by a laminated sheet that consists of $25\ \mu\text{m}$ aluminium and $25\ \mu\text{m}$ Mylar. The wrapping improves the scintillation light yield due to internal reflections of the scintillation photons. Two Hamamatsu S2744-08 photodiodes are glued to the rear end of the crystal. Each of them are connected to its own pre-amplifier. This provides two independent output signals from each crystal. The pre-amplifiers filter, shape and integrate the electric signal from the photodiodes. The signal chain electronics from the Belle experiment were upgraded for Belle II, leading to a reduced shaping time and the possibility to record the digitized waveforms [16].

CsI(Tl) as scintillator was chosen due to its high light yield, overall good mechanical properties and a moderate price. As the SuperKEKB accelerator aims to achieve a higher luminosity, it is expected that the higher beam induced backgrounds will lead

to a decreased energy and time resolution of the ECL. To improve timing resolution, the readout electronics have been upgraded to allow shorter sampling times, to fight back against the increased pile up noise from beam background. This is however limited by the slow scintillation time of CsI(Tl). Degraded energy resolution is a result from radiation damage of the crystals. Pure CsI has a much faster scintillation time and better radiation hardness. Therefore, it is investigated as a candidate for a possible detector upgrade, motivating the topic of this thesis.

Based on the work completed in [25], Belle II has become the first e^+e^- collider experiment applying pulse shape discrimination in CsI(Tl) to improve particle identification. This allows to differentiate between hadronic and electromagnetic showers in the ECL. It is especially relevant when it comes to the identification of photon vs. long lived neutral kaon or of muons vs. pions. This work investigates whether this technique can be implemented in pure CsI crystals and to obtain a better understanding of the scintillation mechanism that allows pulse shape discrimination on the level of a single crystal.

Chapter 4

Experimental setup

An experiment setup is designed to investigate pulse shape discrimination in a single pure CsI crystal. It uses a single pure CsI crystal, and a CsI(Tl) crystal for reference. The crystals have the same geometry. The detector assemblies and the readout of the signal are identical. The setups only differ in the scintillation crystal used, Since the scintillation properties of CsI(Tl) are well known from various previous studies [1, 20, 26], it offers a sufficient reference of the experimental observations.

A conceptual overview of the experiment is shown in Figure 4.1. Incoming particles hit the crystals and generate scintillation light, which is recorded by a photo-multiplier tube (PMT). The analogue signal output of the PMT is converted into digital format by a waveform digitizer (ADC). The data recorded by the ADC is saved on a PC and used for offline analysis.

Data of electromagnetic and hadronic particles are needed to perform pulse shape discrimination. Samples of electromagnetically interacting particles are obtained through the continuous flux of cosmic muons. To obtain samples for hadronic interactions, measurements with the detectors were done at XS1 UG2 at the X-Ray Free-Electron Laser Facility (XFEL), which is described in detail in Section 4.2.

The details of the experimental setup are listed in the first section of this chapter. The second section provides details on the measurement location at XFEL and the expected neutron spectrum there.

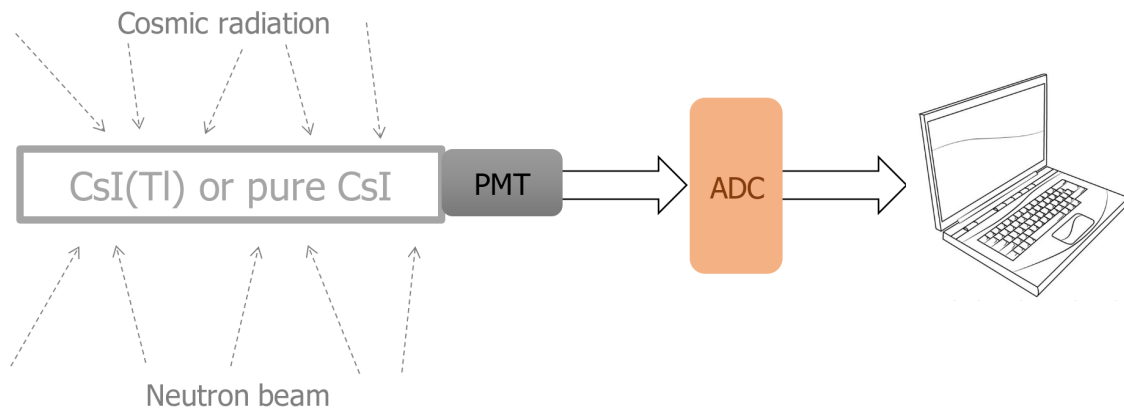


Figure 4.1: A schematic overview of the experimental setup. Cosmic rays or a neutron sample hit the crystal. A photo-multiplier tube (PMT) is attached to one end of the crystal. The output signal is supplied to a waveform digitizer (ADC), which is connected to a local computer.

4.1 Detector assembly

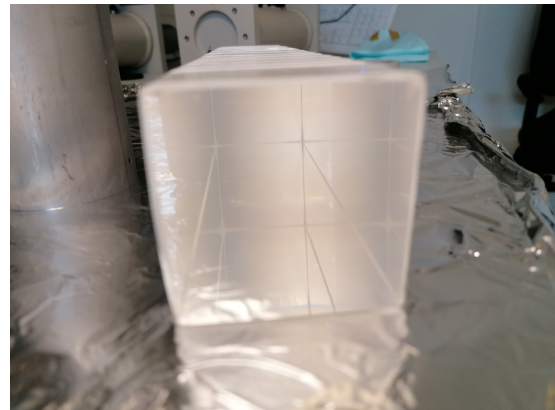
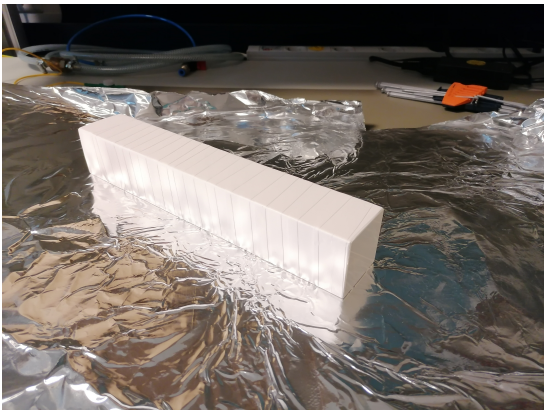


Figure 4.2: The left image shows a side view of the pure CsI crystal and its wrapping in reflective Teflon tape. The right image shows the front side of the crystal where it was unwrapped.

A pure CsI and a CsI(Tl) crystal are used for the detector setup. They have a size of $5 \times 5 \times 30 \text{ cm}^3$ and were manufactured by Saint Gobain. Both crystals have similar chemical properties, as they are both mainly consist of caesium iodide. However, they exhibit vastly different scintillation properties. A comparison of the relevant properties of pure CsI and CsI(Tl) according to [27, 28] is listed in Table 4.1. Both crystals have

multiple scintillation components. For CsI(Tl), the fastest is at $0.6 \mu\text{s}$ and the slowest at $3.5 \mu\text{s}$ [28]. When highly ionizing particles deposit energy, further scintillation components are present, which depend on the energy of the particle [28]. For pure CsI, the decay time is at 16 ns, at which 70 to 80 % of the total light output are emitted, and a slower component of around 1000 ns [27]. However it has a very low yield of only 2 photons per keV, while the doped CsI(Tl) is one of the brightest scintillators known, as it has a high conversion efficiency of 54 photons per keV deposited in the scintillator [28]. To increase the light yield, the crystals are wrapped in a layer of reflective Teflon. The wrapping on the front side was undone to attach the PMT there, as seen in Figure 4.2.

Table 4.1: Overview of relevant scintillation properties for pure CsI and CsI(Tl) according to [27, 28].

	Max. emission	Decay time	Light yield [photons/keV $_{\gamma}$]
Pure CsI	315 nm	1000 ns	54
CsI(Tl)	550 nm	16 ns	2

Photo-multiplier tubes (PMT) are used for the readout of the scintillation signals. A standard PMT does not offer optimal conditions for pure CsI, which has its maximum emission wavelength in the UV-range, at 315 nm [27]. *Hamamatsu* R5113-02 PMT were chosen to adjust to this. They correspond to the model R329-02, but they are additionally equipped with a UV window, offering a spectral response for wavelengths from 300 to 650 nm [29]. One PMT is mounted to each crystal at the unwrapped 5×5 cm end. The PMT has an effective area of 4.6 cm^2 [29]. The crystal and PMT are optically coupled by a small air gap between both. Therefore, the quantum efficiency of the PMT is only impacted by the scintillation emission of the crystal. The DT8031 *CAEN* HV supply is used for the PMTs. The PMT on the pure CsI crystal is operated with a voltage of 1500 V, while the CsI(Tl) is operated with 1700 V. Different numbers were chosen as the light output is different for each of the crystals, the details on the calibration are given in Section 6.3.

The crystals and their PMTs are placed in a housing to offer a light-proof surrounding. A 3D model of its design is shown in Figure 4.4. Technical drawings from various

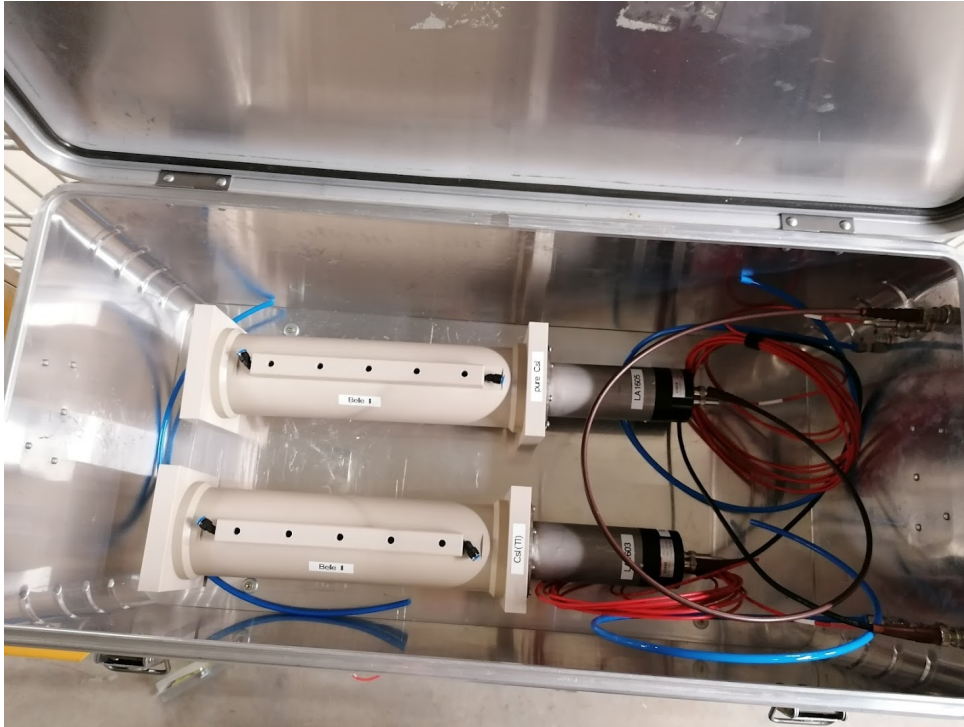


Figure 4.3: The assemblies for both crystals at XFEL XS1 UG2. They are in a light-proof metal box. The crystals and PMTs are in their housing.

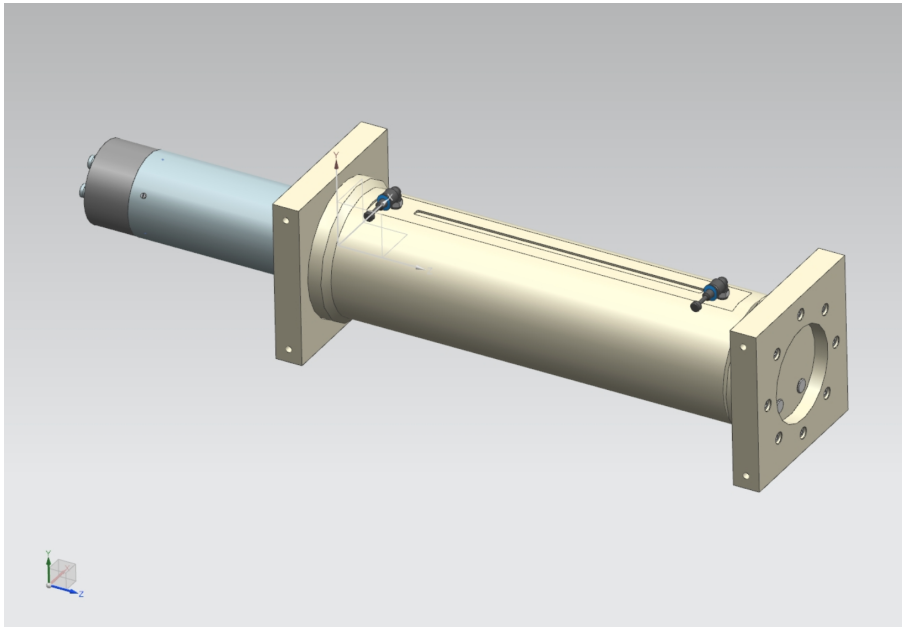


Figure 4.4: 3D model of the shielding for the setup.

angles are furthermore shown in the Appendix A. The housing holds the crystal close to the PMT and is designed to slightly push the PMT against the crystal. This ensures

a minimal distance between the two and maximizes the efficiency of the PMT.

To furthermore ensure no external light reaches the setup, the crystals within their housing are placed in a metal box. The whole detector setup of the crystals in their housing placed within the box can be seen in Figure 4.3.

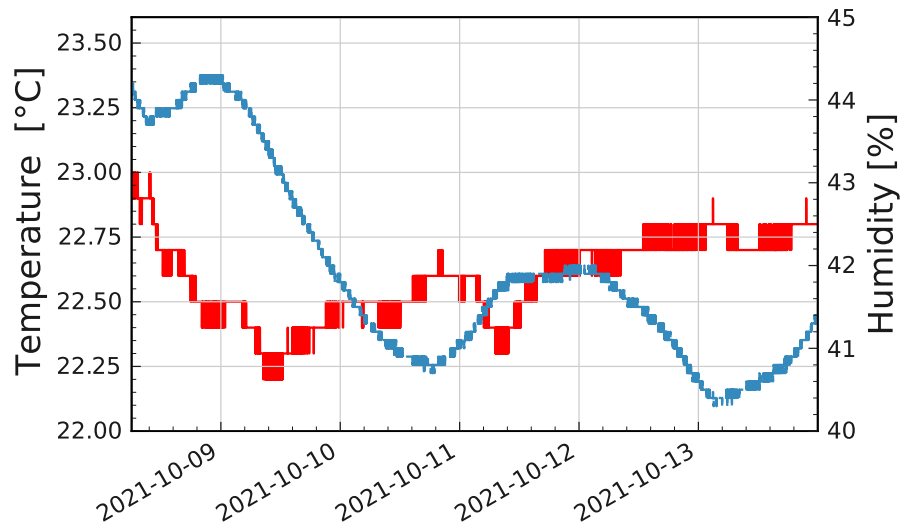


Figure 4.5: Temperature and humidity inside the housing of the crystals at the measurement location at XFEL.

The output signal of each PMT is provided to a DT5730SB CAEN digitizer. The analogue signal from the PMT is converted into a digital signal at a resolution of 14 bit and a sampling rate of 500 MS/s on each channel, resulting in a sampling time of 2 ns [30]. It is operated in self-triggering mode on a constant voltage threshold. The digitized signal is saved for offline analysis.

Since the crystals are sensitive to high humidity and their scintillation properties depend on the outside temperature, temperature and humidity are monitored. This is done by an Arduino Uno controlling board setup according to [31]. The temperature and humidity sensors are placed within the shielding right next to crystals. Figure 4.5 shows the temperature and humidity data close to the CsI(Tl) crystal when it was located at the laboratory on the DESY campus.

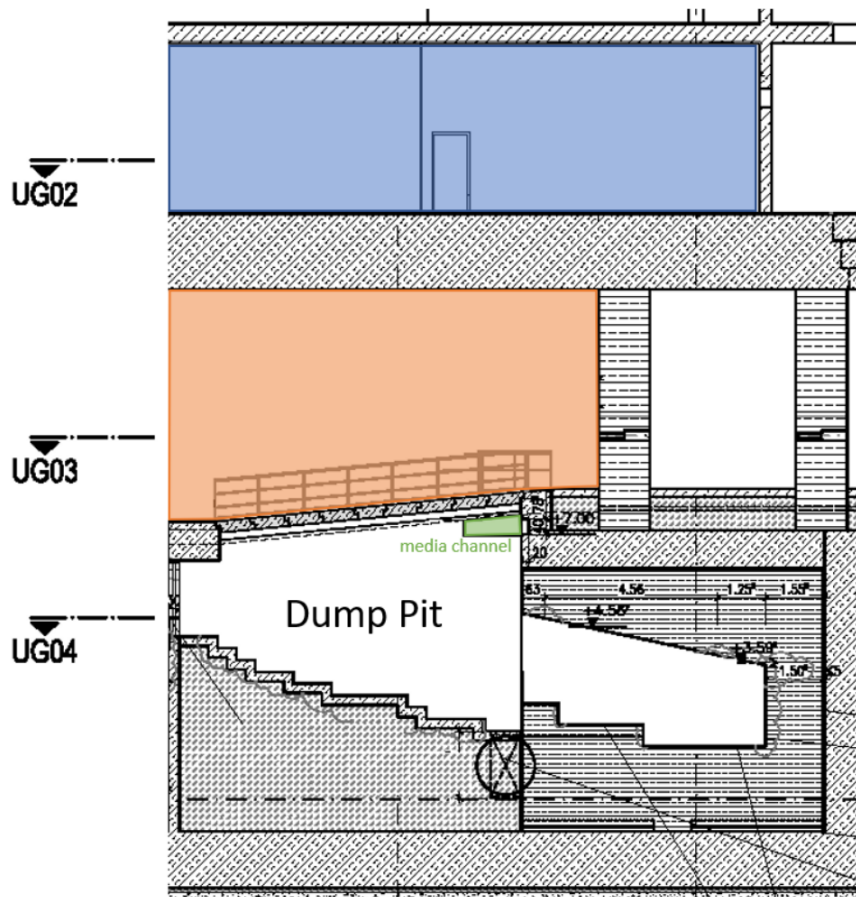


Figure 4.6: A vertical view of the XS1 UG2 at XFEL. Shaded in orange is U3, which is connected to the dump pit in UG4 through a media channel (green). UG2 is highlighted in blue. From [32].

4.2 Obtaining of neutron data samples

The experimental setup is located close to a beam dump pit at the XS1 location of the XFEL facility in the UG2 level. The location of UG2 with respect to the beam dump is illustrated in Figure 4.6. Electron beam losses of the XFEL accelerator occur at the UG4 level within the dump pit. Directly above is the UG3, which is 6.3 m high and shielded by a 30 cm layer of heavy concrete from the dump pit directly below. The UG2 level is located above UG3 with 2 m of additional shielding with normal concrete between them [32].

During the operation of XFEL, electrons with energies up to 17.5 GeV can be guided to the dump pit at XS1 to terminate the beam. Out of the 460 bunches that are produced

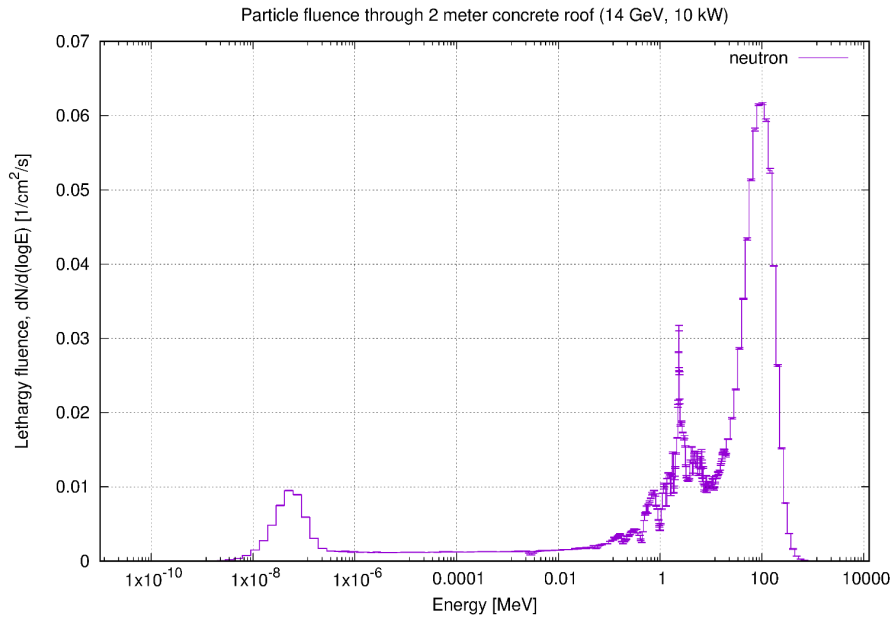


Figure 4.7: Neutron lethargy flux spectrum entering XS1 UG2 at XFEL campus. High energetic neutrons with 100 MeV are the dominant component of the spectrum. From [32].

in the accelerator, about 430 of them are typically dumped into the beam dump [33]. Secondary particles such as photons or neutrons are produced in the beam dump, which have sufficient energies to go through the layers of concrete housing and reach UG2 level. When high energy neutrons pass through massive shielding, such as thick concrete walls, a spectrum of high energetic neutrons with a peak at 100 MeV is expected [34]. The cross section of neutrons with the concrete has a minimum at this energy, therefore neutrons with this energy will pass through the concrete layers [34]. The crystal setup is placed directly next to a Pandora detector, which monitors the radiation at several locations of XFEL. Pandora detectors consist of He-3/plastic scintillator detectors and are described in detail in [35]. A typical spectrum of the neutrons at XS1 UG2 is shown in Figure 4.7. It shows the expected peak for neutrons at 100 MeV. The neutron dose rate at the location of the crystal setup can be seen from a horizontal perspective in Figure 4.8.

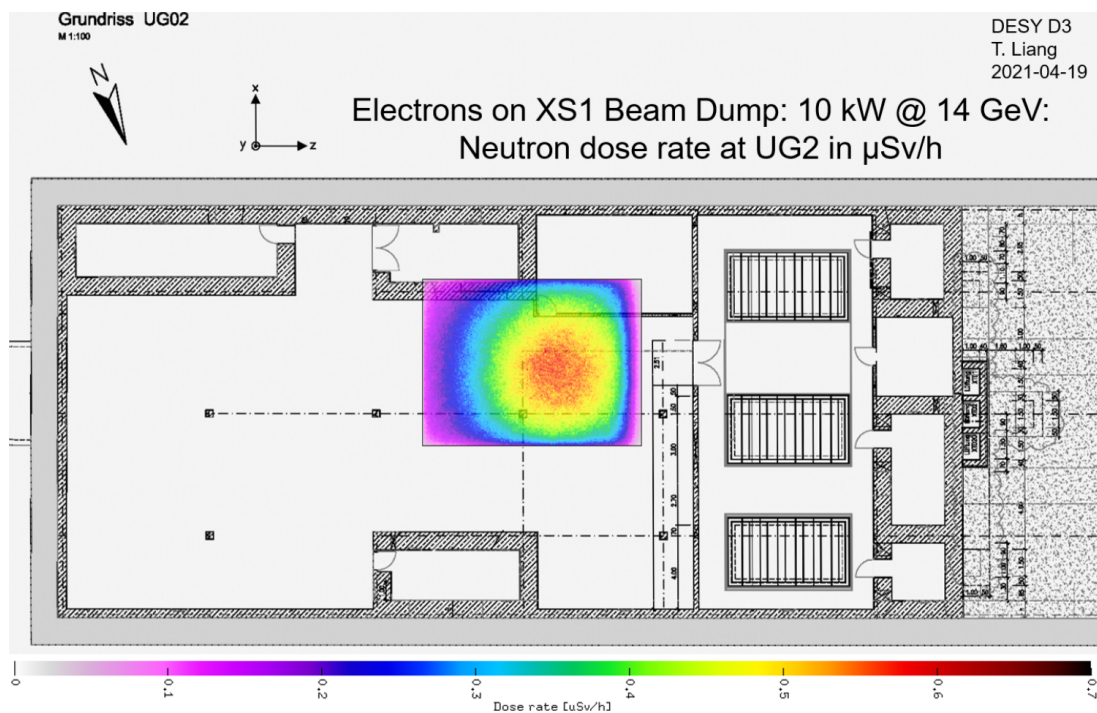


Figure 4.8: Horizontal view of the XS1 UG2 location at XFEL campus. The neutron dose rate is pictured in the case where the electron beam at XFEL is operated at an energy of 14 GeV [32]. The setup is placed in the middle of the area marked in red, where neutron dose rate is highest.

Chapter 5

Pure CsI simulation studies in GEANT4

Simulations of the experimental setup described in Chapter 4 are performed. Scintillation processes in an ideal pure CsI crystal are simulated with the GEANT4 toolkit [36]. The first section of this chapter describes the properties of the detector setup in the simulation. The second section supplies details on the used event generators and describes the resulting waveform and scintillation process.

5.1 Detector construction

Samples for waveforms in a pure CsI crystal are simulated. The pure CsI crystal has volume cuboid volume of the dimensions $5 \times 5 \times 30 \text{ cm}^3$. A cylindrical volume is placed at one of the short ends of the crystal volume to simulate the PMT volume.

To simulate scintillation effects in the volume, optical photon processes are included in the simulation, since GEANT4 differentiates between photons at high energies and optical photons at low energies [36]. They are treated as different classes and therefore interact via different processes. Photons are to be considered as optical when their wavelength is much greater than the typical atomic spacing. They can be produced through the Cherenkov effect or scintillation. Possible interactions for optical photons are absorption, Rayleigh scattering, mie scattering, wave-length shifting and boundary scattering [37].

To simulate scintillation effects within the scintillator, optical properties need to be

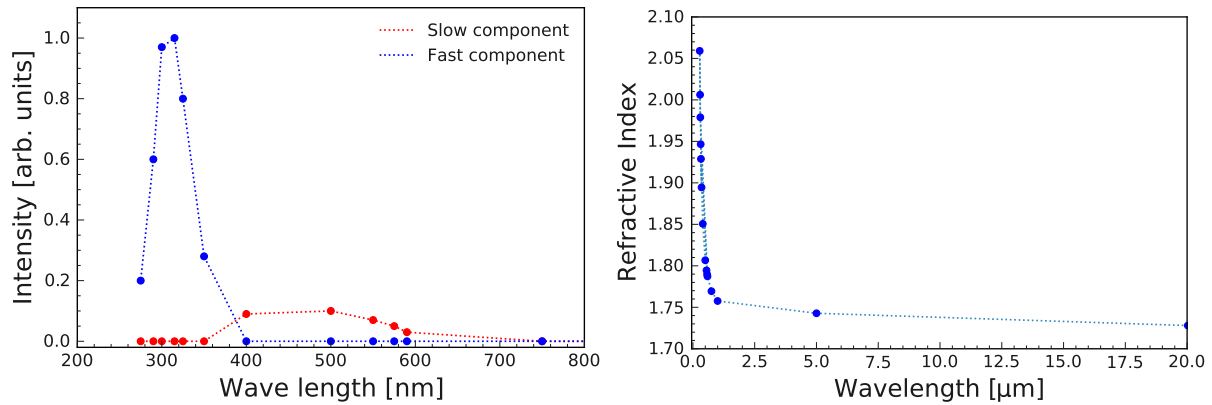


Figure 5.1: The relative intensity (left) and the refractive index (right) of pure CsI, dependant on the wavelength of incoming light.

assigned to the material and its surfaces. Figure 5.1 shows the inputs given to the simulation based on the material properties of pure CsI regarding its refractive index [38] and its scintillation properties [27]. The scintillation response of the crystal is split into a longer scintillation component, which is set to be at $1 \mu\text{s}$, and a slower component at 16 ns , which is responsible for 80% of the scintillation light output [27].

5.2 Event Generation

The simulation of cosmic radiation is done with the CRY event generator [39]. The Monte Carlo sample consists of all types of particles possible in cosmic radiation. The cosmic radiation is mostly due to galactic protons and, to a minor level, due to alpha particles and heavier particles. The CRY simulation however simulated only the effects from primary protons [40].

The expected energy spectrum left by cosmic radiation in the pure CsI crystal is shown in Figure 5.2, which mainly consists of muons but also includes a small number of hadrons, such as pions [17].

The distribution shows a single peak, showing that most of the particles in the cosmic radiation deposit a similar energy within the crystal. The peak corresponds to the energy deposits by cosmic muons. A fit is applied to this distribution to determine the expected energy deposits. The sum of a function for the background and a signal

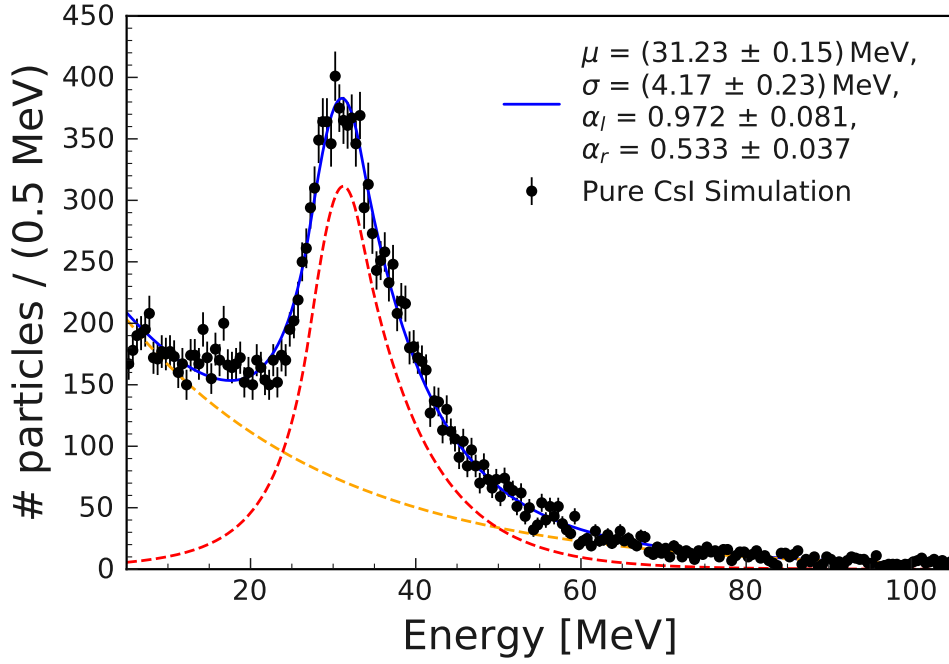


Figure 5.2: Fitted spectrum of energy deposits in a pure CsI using events the CRY event generator. The black points show the data, while the blue curve shows the total fit. The dotted red line shows the double-sided Crystal Ball component of the total fit, while the yellow dotted line shows the exponential component of the total fit.

component for the peak is chosen for the fit. The background is modeled with an exponential function

$$f(x) = \frac{e^{\lambda x}}{\int_{lower}^{upper} e^{\lambda x} dx'} \quad (5.1)$$

where λ is the decay constant of the exponential and *upper* and *lower* refer to the fitting boundaries. The exponential function is normalized over a finite range between the lower and upper fitting boundaries.

The peak is modeled by a double sided Crystal Ball function

$$f(x; \mu, \sigma, \alpha_L, n_L, \alpha_R, n_R) = \begin{cases} A_L \cdot (B_L - \frac{x-\mu}{\sigma})^{-n} & \text{for } \frac{x-\mu}{\sigma} < -\alpha_L \\ \exp(-\frac{(x-\mu)^2}{2\sigma^2}) & \text{for } -\alpha_L \leq \frac{x-\mu}{\sigma} \leq \alpha_R \\ A_R \cdot (B_R - \frac{x-\mu}{\sigma})^{-n} & \text{for } \frac{x-\mu}{\sigma} > \alpha_R \end{cases} \quad (5.2)$$

with $A_{L/R} = (\frac{n_{L/R}}{|\alpha_{L/R}|})^n \cdot e^{-\frac{|\alpha_{L/R}|^2}{2}}$ and $B_{L/R} = \frac{n_{L/R}}{|\alpha_{L/R}|} - |\alpha_{L/R}|$.

A waveform in pure CsI is shown in Figure 5.3. It corresponds to the number of

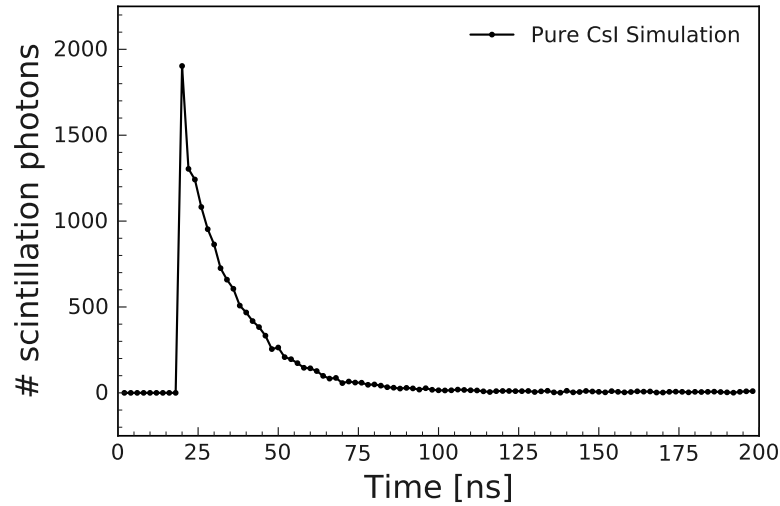


Figure 5.3: Typical waveform in pure CsI from the the CRY cosmic event generator. The dots show the data points, the lines are connected to guide the eye.

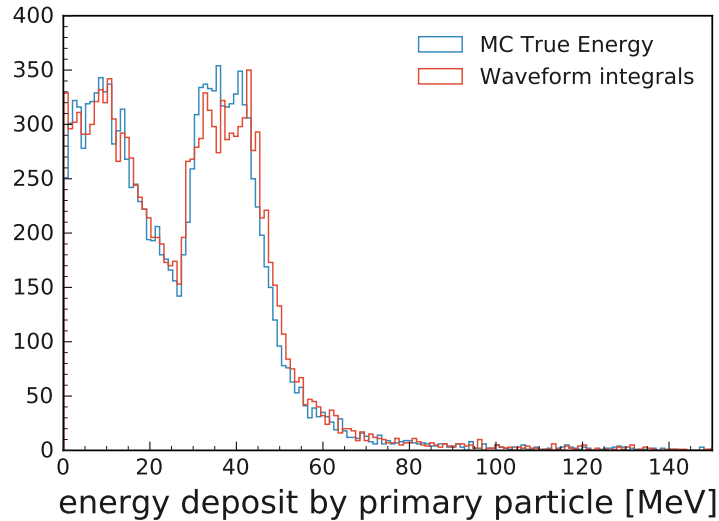


Figure 5.4: Spectrum of energy deposits in a pure CsI using events particle gun muons (left). The right side shows the comparison of energies computed as integrals of the scintillation photons with Equation 6.1 and the MC truth information.

scintillation photons emitted at a certain time. The optical properties of the material determine the decay time of the waveform. As the main goal of this thesis is to perform pulse shape discrimination, the method using charge ratios will be applied. This takes into account waveforms, integrated over different time windows. It will be introduced furthermore in Section 7.2 of this thesis. Figure 5.4 shows the result of a toy study using particle gun muons, hitting a pure CsI crystal. It shows that the main amount

of energy deposits by muon is dedicated by the track length of muons through the crystal, as in this case, the source of primary particles comes from a fixed location. Most of the energy deposits are in the range from 30 to 40 MeV. It can also be seen that the integration over the scintillation pulse shape leads to qualitatively the same energy spectrum as the energy deposited in the crystal.

Chapter 6

Waveform analysis

This chapter specifies the processing of the raw waveforms and the event selection applied to the recorded data set. The first section of this chapter describes the processing of the individual waveforms. Details on the preselection of events, which removes noisy signal, waveforms with pile-up and other types of distorted waveforms, are given in the second section. A calibration of the setup is performed in the third section of the chapter.

6.1 Waveform processing

All waveform are recorded over a span of $30\ \mu\text{s}$ with a sampling time of $2\ \text{ns}$. This results in 15000 data points from the ADC. The time of $30\ \mu\text{s}$ was chosen to accommodate the scintillation time of the CsI(Tl) crystal. Properties of each recorded raw ADC waveform are determined before any other step of the analysis. Generic properties such as the baseline level, the start of the signal t_0 and the integral of the waveform are determined.

The baseline correction is applied for each individual waveform. The baseline is obtained by averaging over the first $\frac{1}{8}$ th of the waveform, which corresponds to 1875 data points entries or $3.75\ \mu\text{s}$. This offers a sufficient number of ADC samples before the triggering of the signal, which is set to be at 25 % after the beginning of the recorded ADC waveform ($7.5\ \mu\text{s}$). Figure 6.1 shows unprocessed recorded signal waveforms and

the corresponding values for the baselines, which will be subtracted from the recorded ADC signal. This provides waveforms with ADC values aligned around zero in case of no signal.

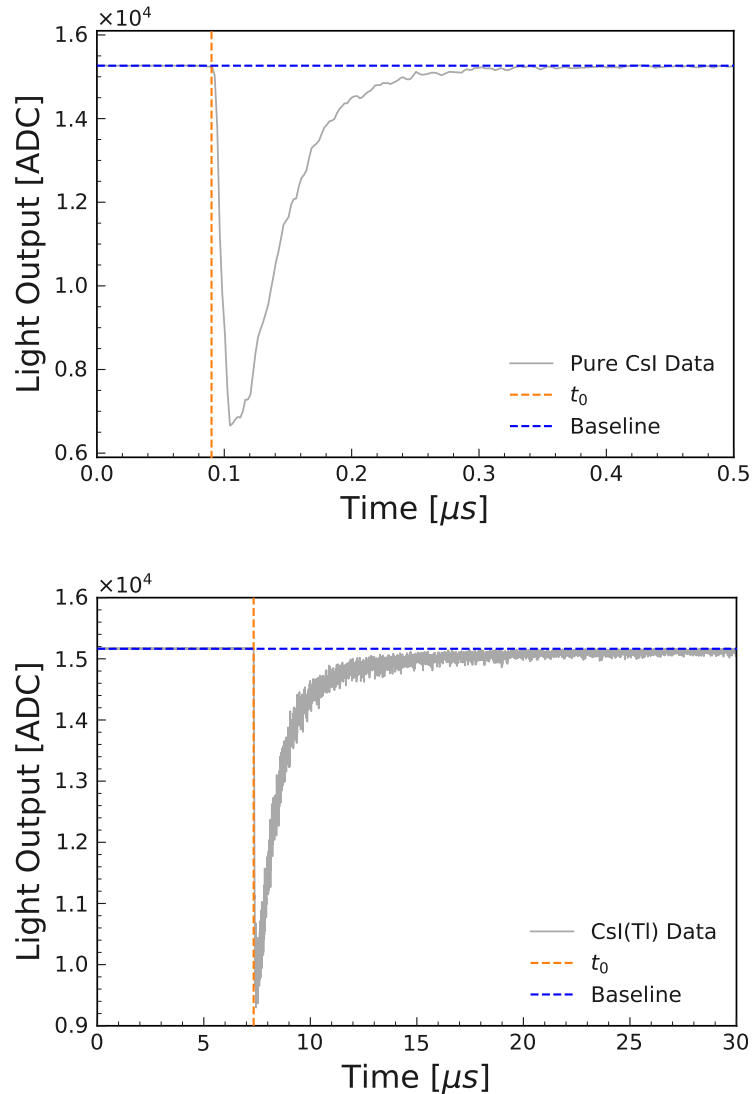


Figure 6.1: Typical ADC waveform recorded with the pure CsI crystal (top) and with the CsI(Tl) crystal (bottom). Data is shown in gray. The blue dashed line indicated the baseline, while the orange dashed line shows the determined beginning of the event t_0 .

Figure 6.1 also shows the t_0 of the waveforms. The t_0 corresponds to the precise starting point of the signal, which needs to be determined precisely to carry out the future analysis. An Optimum Filter fit is performed on the waveforms to obtain the t_0 . The fits are done with the code framework from the QETpy analysis tools from [41]. Every

single waveform is separately fit to a template, which has been created from a sample of waveforms that were taken in laboratory environment and therefore correspond to mainly waveforms of cosmic muons.

The energy deposit by an incoming particle in the scintillation crystal is obtained via

$$E = \sum_{t=t_0}^{t_{long}} x(t) \cdot C \quad (6.1)$$

where $x(t)$ is the light output of the scintillator in ADC units during the time t , t_{long} is the end of the time interval of the integration and C is the energy calibration factor.

Equation 6.1 can be applied since the integral of the waveform directly relates to the energy deposited within the scintillation crystal [18].

The length of the full waveform t_{long} is dominated by the scintillation properties of the crystal. This corresponds to 500 ns for pure CsI and 22 μ s for CsI(Tl), to include as much of the waveform tail as possible.

6.2 Preselection

A preselection is applied to ensure the quality of the waveforms. Various cases can occur that result in a waveform not suitable for further analysis. The three main types of not suitable waveforms are the following:

1. sudden spike in amplitude over a few data points, shaped like a delta distribution ("glitches"),
2. waveforms with a tip that is cut off, since its maximum amplitude exceeds the maximal possible value that can be recorded ("clipped waveform"),
3. waveforms with multiple scintillation pulses ("pile-up").

Example waveforms for each of these cases are shown in Figure 6.2. Glitches and clipped waveforms are selected through numeric conditions on the raw data. The maximal amplitude height of the raw waveform is known as property of the digitizer as it

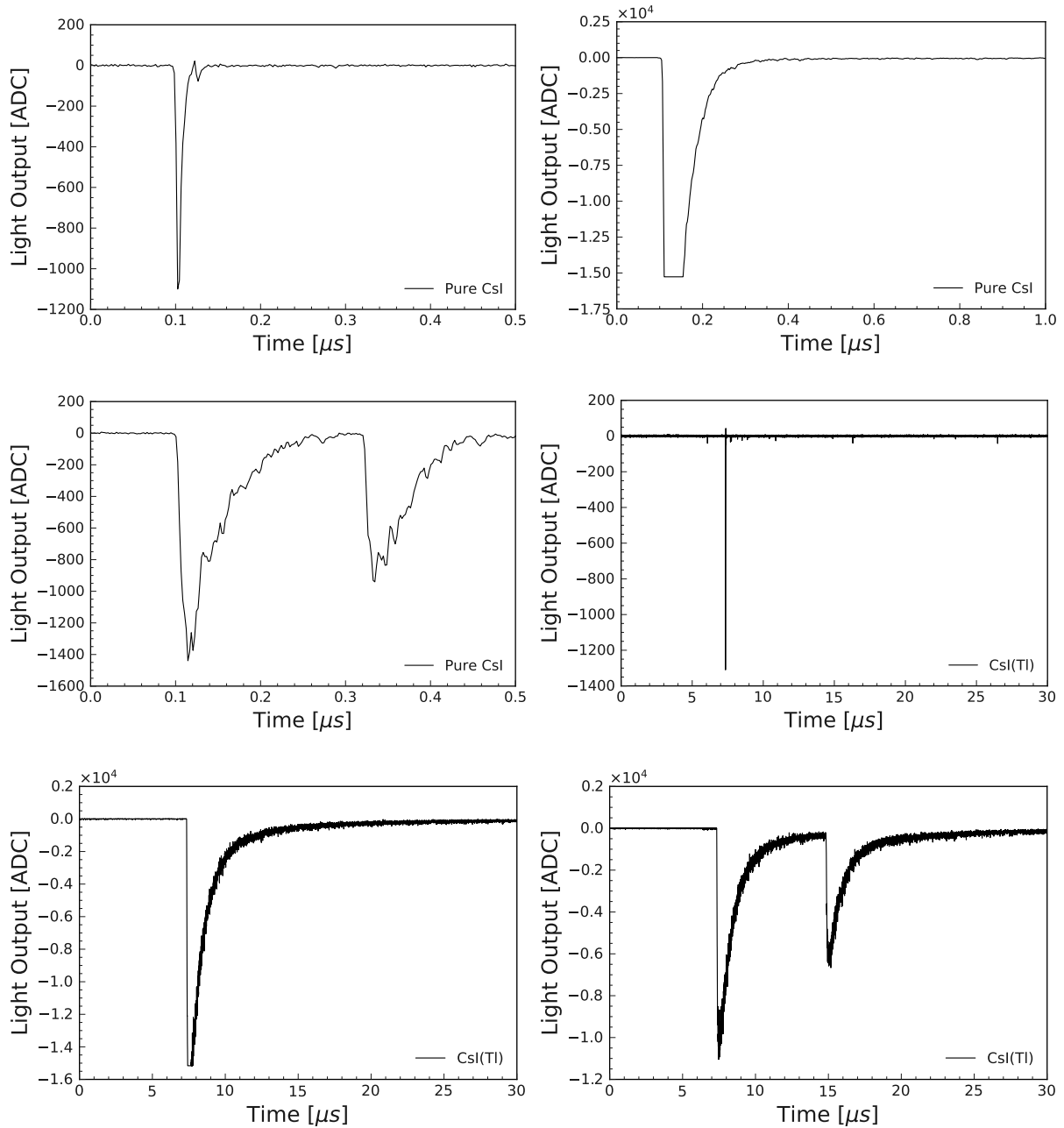


Figure 6.2: A glitch waveform (top), a clipped waveform (middle) and a pile-up waveform (bottom). The left column shows waveforms recorded with the pure CsI crystal, while the right one shows the waveforms in the CsI(Tl).

only allows ADC values between 0 and 16000. Fully recorded waveforms are within this range, but clipped waveforms will reach these limits. If the waveform has its lowest ADC value at 0, it is classified as clipped. Since the waveforms in this study are of negative polarity, the highest possible amplitude of the waveform corresponds to

a numeric minimum, therefore the critical value is at 0. For the glitches, a rapid rise time is observed. The timing difference between the starting point t_0 and the overall minimum value in the waveform is required to be at least 10 ns. If the difference is lower than 10 ns, the waveform is classified as glitch.

The `scipy find_peaks` tool [42] is used to determine the peaks of each waveform. The peaks are required to be at least 30 ns apart for the pure CsI waveforms and $0.4 \mu\text{s}$ for CsI(Tl). This requirement ensures that the same peak will not be selected twice, which is possible due to noise fluctuations between data points in the waveform. Furthermore, the peaks are also required to show a certain prominence. The prominence refers to how much the peak stands out from the surrounding baseline of the signal. It is defined as the vertical distance between the peak and the lowest contour of the baseline [43]. In this analysis, the vertical distance is required to be at least 8.5% of the minimum value of the waveform for pure CsI waveforms and of 40% for CsI(Tl) waveforms. These percentages differ between the crystals due to the different scintillation characteristics of each crystal. The CsI(Tl) crystal has a longer scintillation times, so more fluctuations are present between the individual data points, which make it necessary to require a higher percentage. Meanwhile the waveforms in pure CsI show less fluctuations between the different time points, which allows a lower threshold for the prominence.

The final criteria of the preselection serves to filter out "noisy" waveforms. A requirement is placed on integral of the normalized waveform, which is computed by normalizing each waveform by its minimum and then computing the integral according to Equation 6.1 without using any energy calibration ($C = 1$). Pile-up waveforms can be filtered out by this condition since their normalized integrals will be larger than the integral of a waveform with just one event. The energy distributions of the full data set used for this analysis is shown in Figure 6.3. It entails a total number of 11 981 837 events in the pure CsI scintillator, out of which around 75.98 % pass the preselection. In the CsI(Tl) crystal, 89.22 % of the total 11 194 699 recorded events pass the preselection. The exact numbers of events that did not pass the preselection, listed according to the

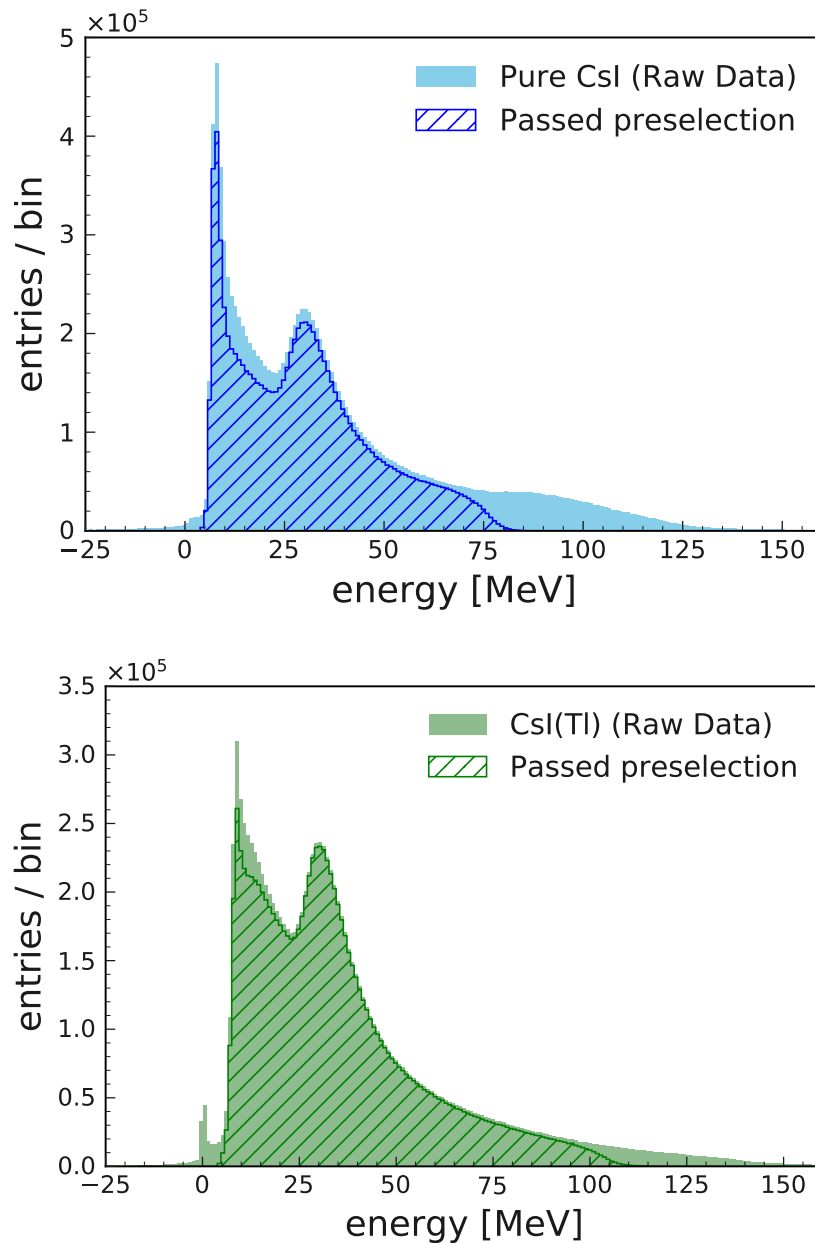


Figure 6.3: Energy spectrum recorded by the pure CsI crystal (top) and CsI(Tl) scintillator crystal (bottom). The filled histogram shows the energy distribution of all events that were recorded in the respective crystal. The striped area shows the distribution of the events that pass the preselection criteria.

criteria they failed, are shown in Table 6.1. If a waveform fails to pass several criteria, it is listed under all of the ones it failed. The energy distribution of the events that do not pass the preselection criteria is shown in Figure 6.4. The images on the left side show the energy spectra recorded in each of the crystals and highlight the events that

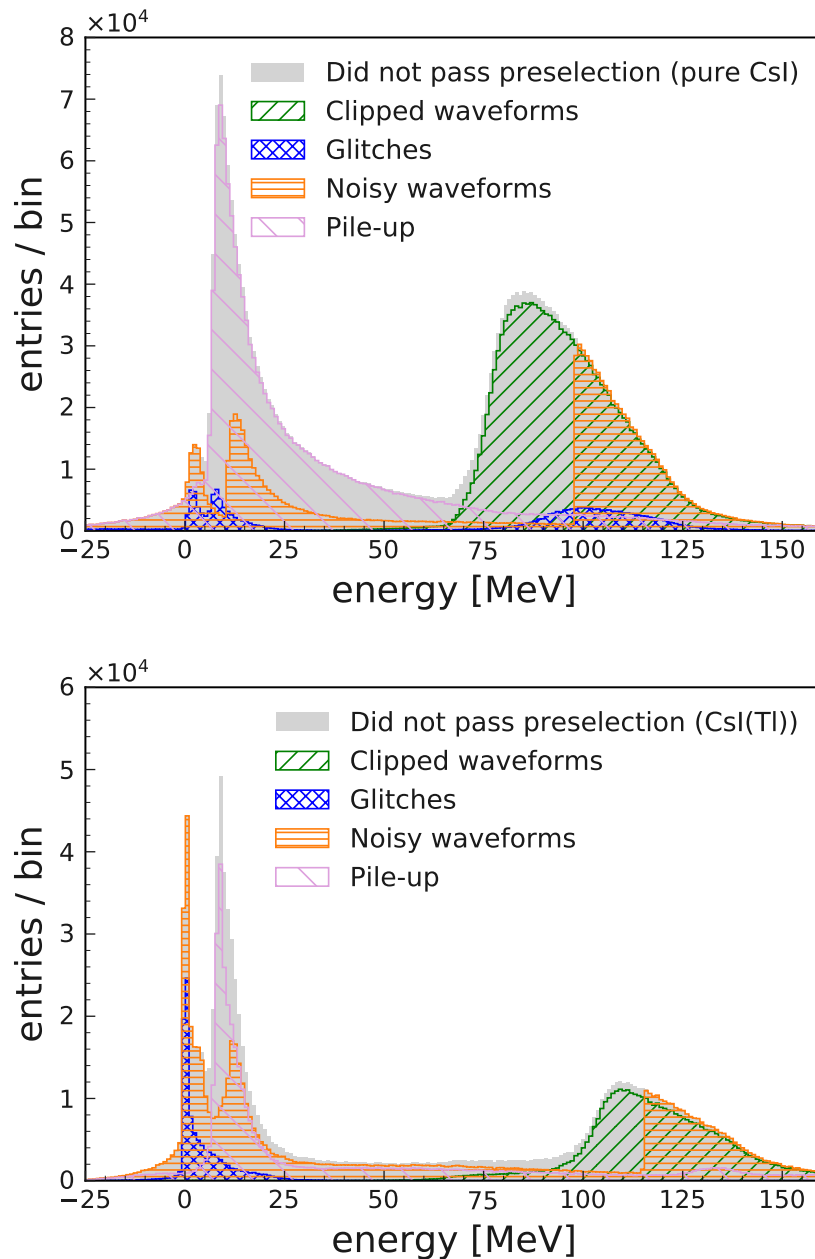


Figure 6.4: Energy spectrum recorded by the pure CsI crystal (top) and CsI(Tl) scintillator crystal (bottom), showing the events that passed the preselection criteria. The right column shows the energy distribution of events that did not pass the preselection in the respective crystal. The striped green histogram shows the clipped waveforms, the dotted blue shows the glitches, orange strips show the noisy waveforms and the pink stripes show pile-up events. Waveforms that fall under multiple criteria are shown under each of them.

pass the preselection. The right side shows the distribution of the events that do not pass the preselection and categorizes them according to which condition they failed.

It can be seen that most events outside a certain energy range do not pass the pres-

Table 6.1: Numbers of events in the data set recorded at XFEL. Events categorized by which criteria they failed in the preselection.

Crystal	Total	Clipped	Pile-up	Glitches	Noisy
Pure CsI	11 981 837 (100 %)	1 481 665 (12.37 %)	1 446 429 (12.07 %)	213 618 (1.78 %)	1 085 912 (9.06 %)
CsI(Tl)	11 194 699 (100 %)	450 648 (4.03 %)	453 964 (4.06 %)	106 258 (0.95 %)	795 247 (7.10)

election. The energy range where most events are kept lies between 5 to 70 MeV for pure CsI and 5 to 100 MeV for CsI(Tl). In the case of CsI(Tl), the energy distribution of all events showed a peak at 0 MeV. All of these events fail the preselection and area attributed to noisy waveforms and/or glitches. The pure CsI crystal does not exhibit a prominent peak at 0 MeV, however a number of events are also found to be glitches or noisy waveforms at energies of 0 MeV. Clipped waveforms start to occur above energies of 75 MeV in the pure CsI and 100 MeV in the CsI(Tl). Pile-up events and noisy events occur through the whole energy range. However these distributions show a peak at around 15 MeV. For the purpose of pulse shape discrimination, it is sufficient to consider the energy range between 12 MeV and 70 MeV, which is in agreement to the expected energy deposits of cosmic muons between 30 to 40 MeV, as seen in Figure 5.2.

6.3 Energy calibration

An energy calibration for each crystal in the detector setup is performed to obtain a calibration factor C , which is needed in Equation 6.1 to convert the value of a waveform integral into units of energy. Measurements with a radioactive source placed close to the scintillation detectors are performed for this purpose. The scintillation crystals are right next to each other and within their shielding during the measurement. The crystals are placed in a metal box in a general laboratory environment with the radioactive source in the middle of the two crystals. For this study, a ^{207}Bi source was used, which has expected emission peaks at 0.569, 1.064, and 1.77 MeV [2]. The emission of the ra-

radioactive source lead to peaks in the recorded energy distribution. Tracing them back to their expected energy values makes it possible to determine the calibration factor C . A fit is applied to describe the shape of the observed spectrum. The total fit consists of

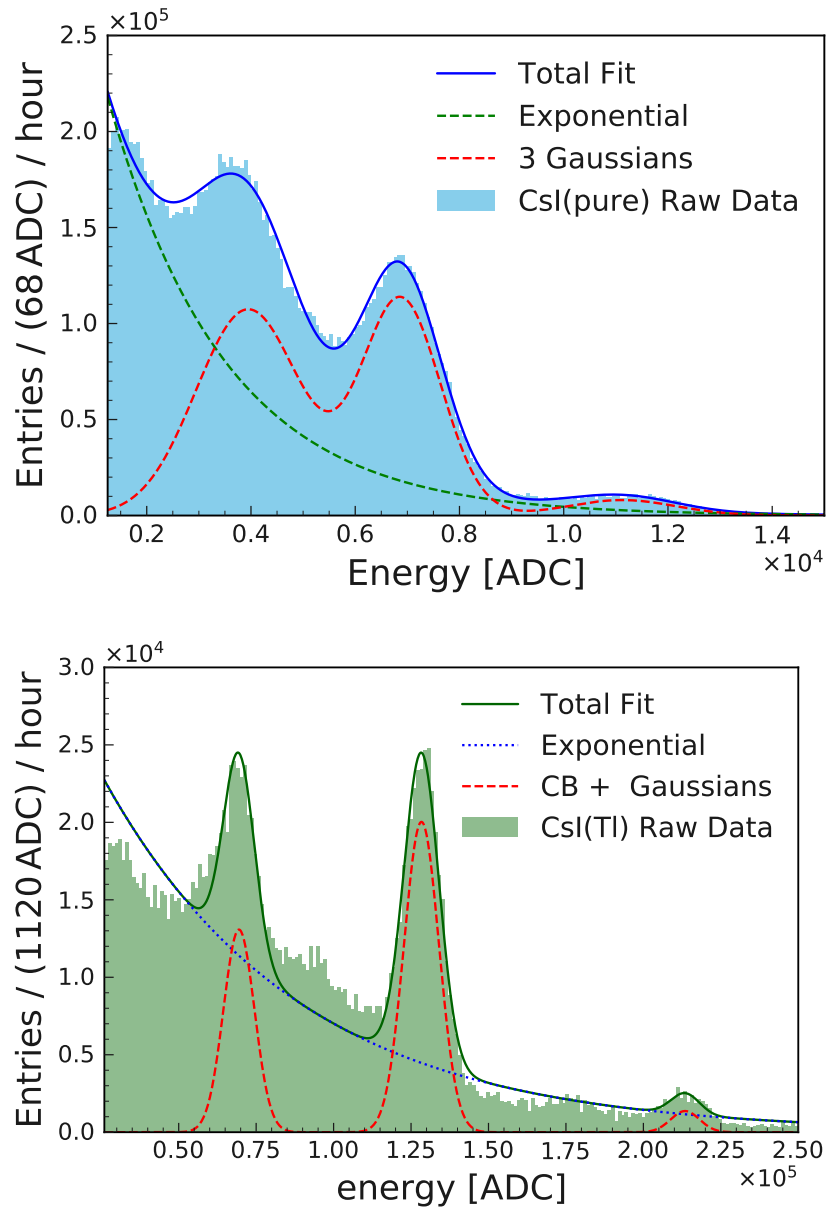


Figure 6.5: Energy spectrum of a radioactive ^{207}Bi source recorded with the pure CsI crystal (top) and CsI(Tl) crystal (bottom). The filled histograms show the data, the total fit is represented with a solid line. Dashed lines show the components of the fitting model, the red dashed line shows the signal component that models the peaks.

a background component and three separate components for each of the peaks.

The background is modeled with an exponential function according to Equation 5.1.

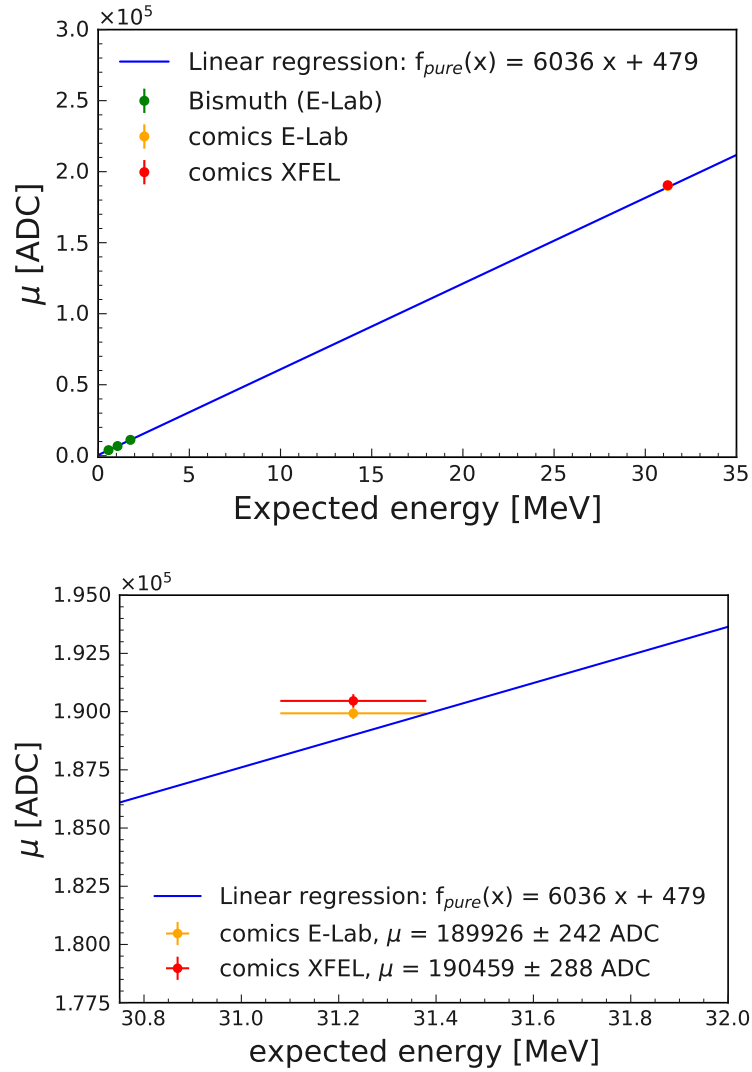


Figure 6.6: Calibration curve for the pure CsI crystal (left). The points through which the linear regression was done are marked in green. The right side shows the extracted values for the location of the cosmic spectrum, marked in red is a spectrum recorded at the XFEL measurement location and in yellow is data recorded in laboratory environment.

Each of the peaks in the pure CsI spectrum is modeled according to a Gaussian function

$$f(x|\mu, \sigma^2) = \frac{1}{\sqrt{2\pi\sigma^2}} e^{-\frac{(x-\mu)^2}{2\sigma^2}} \quad (6.2)$$

where μ is the mean of the Gaussian distribution and σ is the standard deviation of the Gaussian. Two of the three peaks for the CsI(Tl) spectrum are also modeled with Gaussian functions according to Equation 6.2. The lowest energy peak for CsI(Tl) is

modeled with a Crystal Ball function

$$f(x; \mu, \sigma, \alpha, n) = \begin{cases} \exp\left(-\frac{(x-\mu)^2}{2\sigma^2}\right) & \text{for } \frac{x-\mu}{\sigma} \geq -\alpha \\ A \cdot \left(B - \frac{x-\mu}{\sigma}\right)^{-n} & \text{for } \frac{x-\mu}{\sigma} < -\alpha \end{cases} \quad (6.3)$$

with $A = \left(\frac{n}{|\alpha|}\right)^n \cdot e^{-\frac{|\alpha|^2}{2}}$ and $B = \frac{n}{|\alpha|} - |\alpha|$ where μ is the mean of the Gaussian, σ is the width of the Gaussian, α is the parameter where to switch from the Gaussian to the power tail and n is the exponent of the tail.

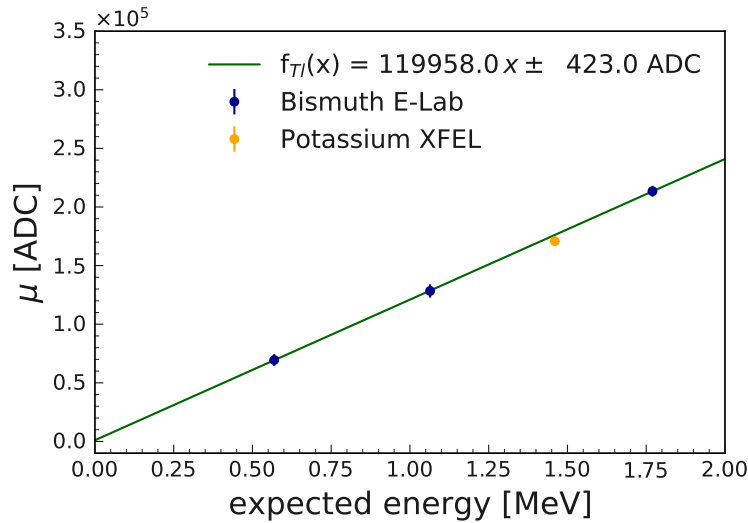


Figure 6.7: Calibration curve for the CsI(Tl) crystal. The points through which the linear regression was done are marked in blue. The extracted mean value for the Potassium peak, which originates in the ambient radioactive background, is shown for reference in yellow.

The energy spectra and the fit results in each of the scintillation crystals are shown in Figure 6.5. It shows the resulting total fit function in comparison to the data and shows the signal and background components of the fit. It can be seen that the exponential background is not sufficient to describe the shape of the background, but the modelling of peaks is sufficient enough to extract the means and widths of the peaks, which will be needed for the energy calibration. The pure CsI shows a lower resolution than the CsI(Tl). This is expected due to the low light yield of pure CsI.

To obtain the calibration constant, the three fitted means μ and the widths σ of the peaks are used to perform a linear regression. The slope of the resulting linear function

will be the calibration constant C . The calibration curves is shown for CsI(Tl) in Figure 6.7 and for pure CsI in Figure 6.6. The Figures show the linear regression through the three points from the calibration measurement. Inserted as reference are the results of fits from other reference measurements at the laboratory location and at the XFEL measurement spot. The reference points from other measurements serve as validation check of the calibration and were obtained from another set of fits to data. For the CsI(Tl) crystal, the signal of natural Potassium radiation is fitted, where the peak is expected to be at 1.460 MeV [44]. This is shown in Figure 6.8. The pure CsI does not offer the resolution to show the Potassium peak, therefore the location of the peaks for cosmic muons is shown. This is shown in Figure 6.9. The location of the mean for the cosmic muon peak is based on the fits performed in Figure 5.2.

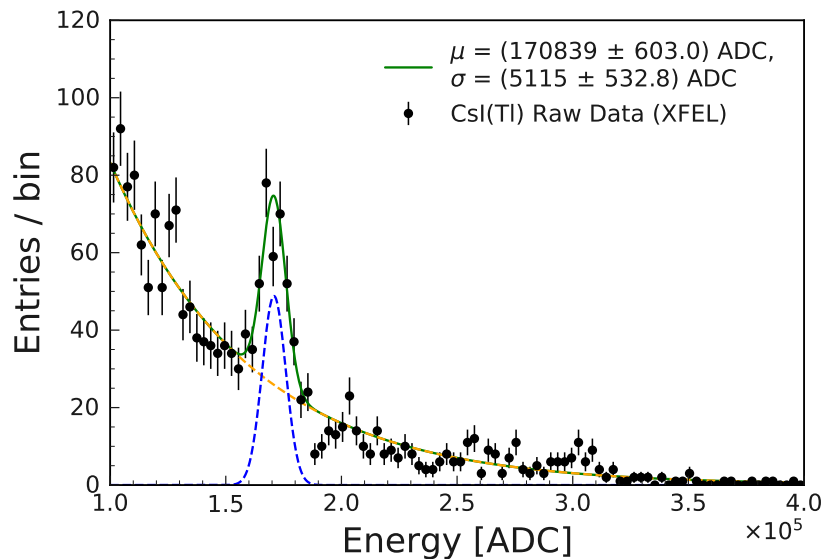


Figure 6.8: Fits to peaks in the energy spectrum recorded with the CsI(Tl) crystal. Data points are shown in black. The total fit is shown with the green line. The signal component of the fit is shown with a blue dashed line, the background component with a yellow dashed line.

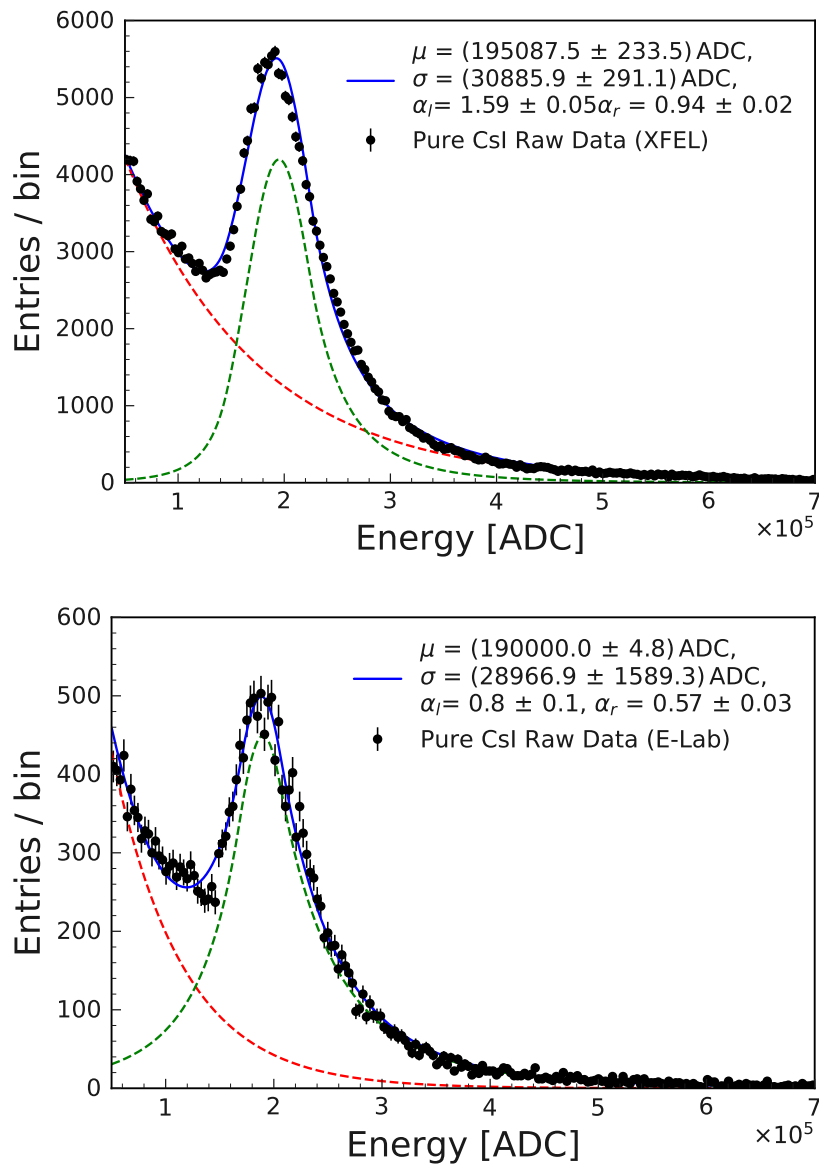


Figure 6.9: Fits to peaks in the energy spectrum recorded with the CsI(Tl) crystal. Data points are shown in black. The total fit is shown with the blue line. The signal component of the fit is shown with a dashed green line, the background component with a dashed red line. The upper image shows the beam off case in the XFEL measurement location while the lower image shows the spectrum recorded in a generic laboratory environment.

Chapter 7

Pulse shape discrimination

Pulse shape discrimination (PSD) methods are applied to differentiate between the scintillation response to electromagnetic and hadronic energy deposits. This chapter discusses the results on the studies of PSD properties of pure CsI and CsI(Tl) crystals for the distinction of cosmic muons and high energetic neutrons. The first section shows the energy spectra recorded with each of the scintillation crystals. The second section shows the results of the PSD studies with the CsI(Tl) crystal using the charge ratio method and compares them to studies for the Belle II electromagnetic calorimeter. The third section investigates the optimal charge ratio time window for pure CsI and the achievable separation power. The last section of the chapter shows the charge ratio results for pure CsI.

7.1 Energy spectra recorded at XFEL

This analysis is based on data recorded at a beam dump pit of a beam-line of the XFEL where flux of high energetic neutrons is expected from below and a continuous flux of cosmic muons is expected from above [32]. The preselection for events in this analysis and the energy calibration are applied according to the criteria listed in Section 6.2. The energy deposits by incoming particles in the scintillation crystals are computed using Equation 6.1.

Figure 7.1 shows the energy deposits of incoming particles in each crystal per hour for

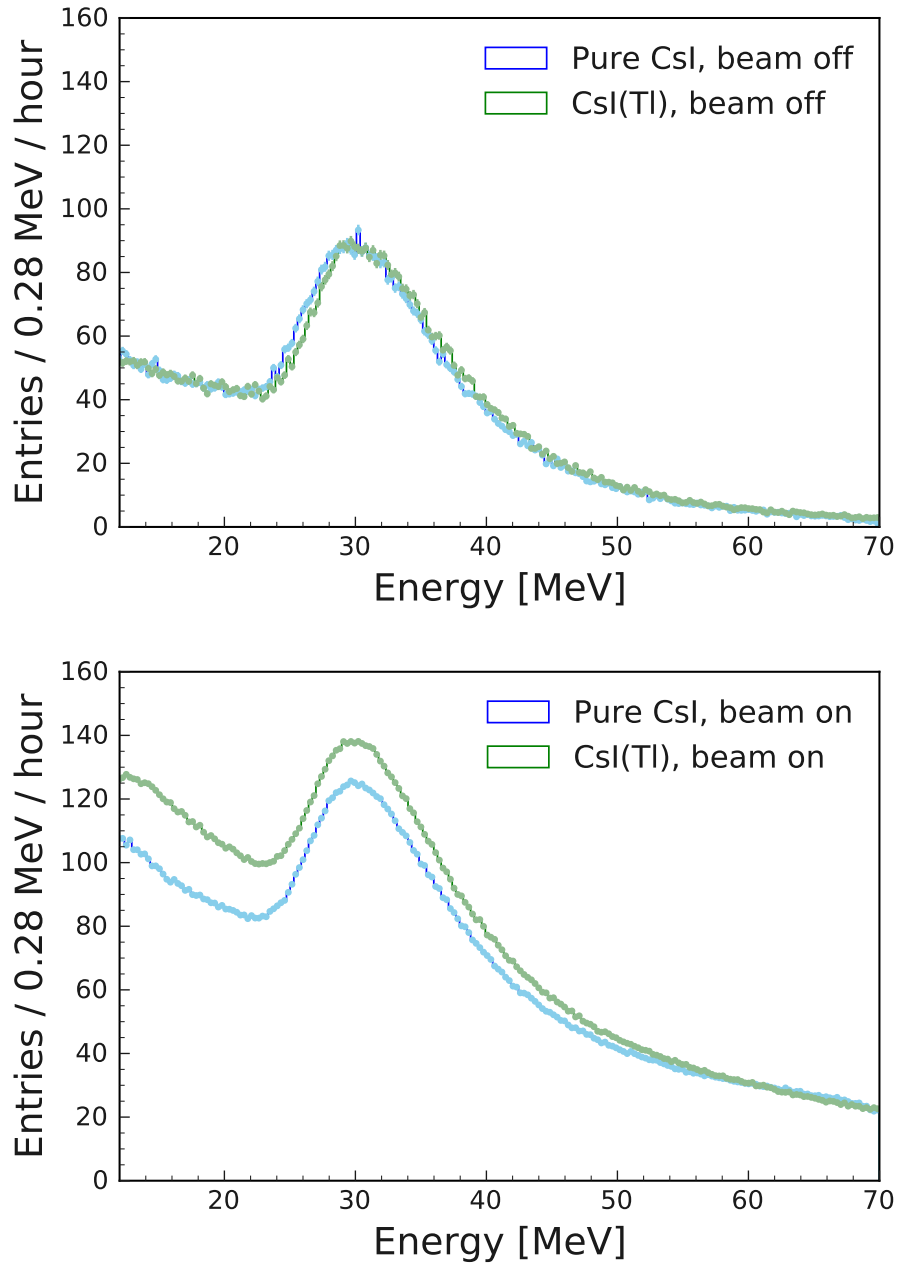


Figure 7.1: Histograms of the energy deposits recorded with the pure CsI crystal (blue) and CsI(Tl) crystal (green). The left image shows the energy distribution for the case when the XFEL beam was turned off, while the right image shows the case when the XFEL accelerator was in operation.

the case when XFEL beam was turned off and turned on. In the case where the beam was turned off, the energy deposits are mainly due to cosmic muons ionizing in the scintillator. It can be seen that the general shape of the spectrum is similar in both crystals. This leads to the conclusion that the shape of the distribution is not dominated by

the respective energy resolution of the crystal. It is dominated by the track length that the muons travel through the crystal, which is given by the crystal geometry. As the geometrical dimensions are identical for each of the crystals, the expected track length is also the same. The position of peak corresponds to the incoming particles travelling through the full 5 cm diameter of the crystal. This also confirms the previously applied energy calibration as sufficient, as the values for energy deposits are consistent with the expectations from the simulations in Figure 5.2.

Most of the energy deposits are associated to cosmic muons ionizing in the crystal when the beam was turned off, so in the case of no beam at XFEL, there are mainly electromagnetically interaction particles. When the XFEL beam is turned on, the expected number of particles leaving energy deposits in the crystal increases for every bin of energy. These additional events due to the neutron flux. Therefore the data set recorded during XFEL beam operation entails samples of electromagnetic and hadronic waveforms. The additional events, which occur only when the beam was turned on, correspond to the spectrum of energy deposits due to neutrons. This difference follows a close to linear distribution and does not show no peak, unlike what is observed for muons. This is due to the properties of neutrons when they interact with the scintillator. Neutrons do not have a electrical charge and have a lower probability to interact with the material they travel trough as discussed in Section 3.1.2. Their main interaction is through inelastic collisions. The energy deposits in the scintillator is attributed to the secondary particle produced in the inelastic collision. Since various particles can be produced in these processes, a continuous increase in events is observed.

7.2 Charge ratio method in CsI(Tl)

A common approach to perform PSD is through integrating the scintillation emission over two different time intervals and computing the ratio. This is called the charge ratio method, or integration method. It has been applied in previous studies for the

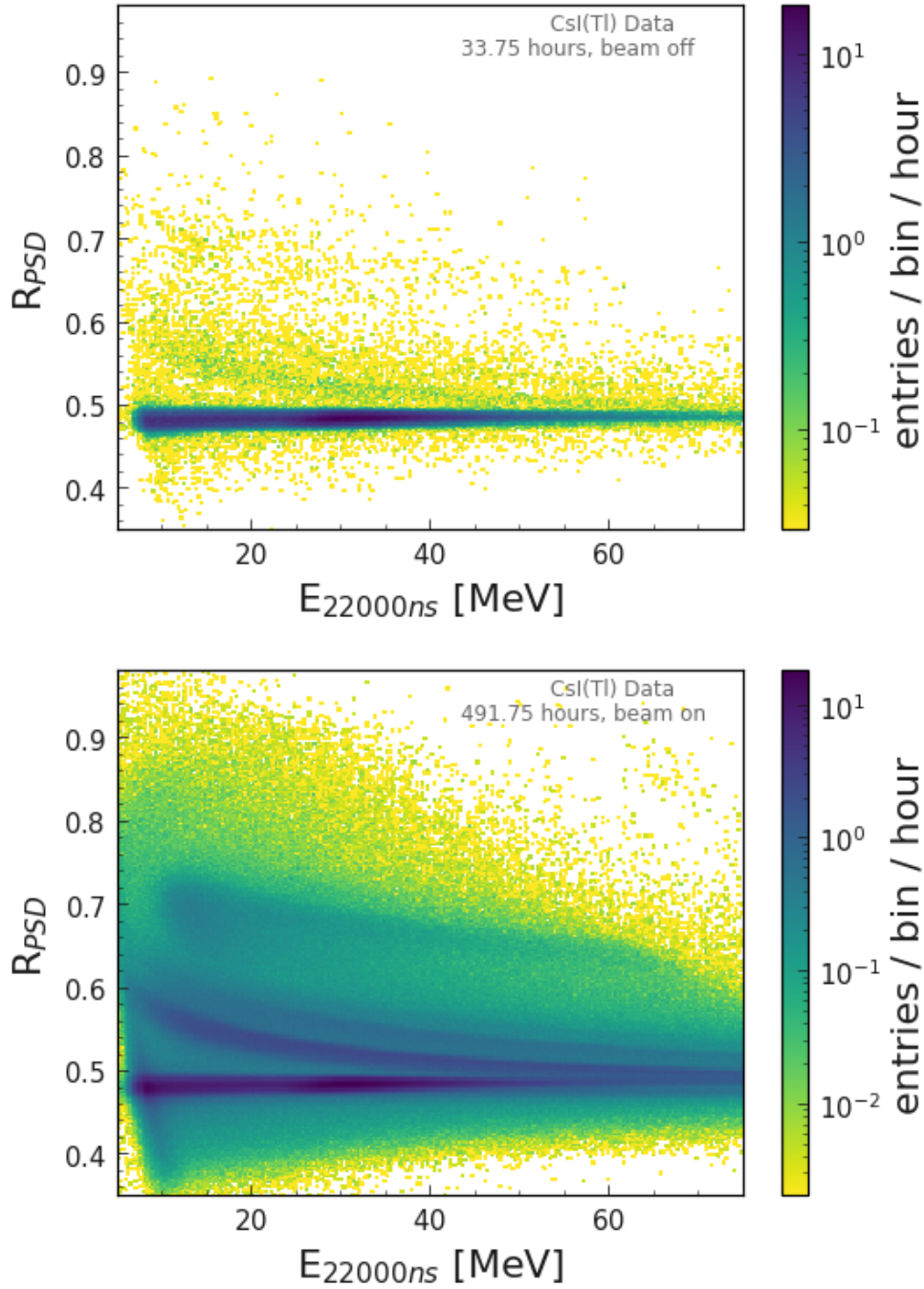


Figure 7.2: Distribution of the charge ratio R_{PSD} in CsI(Tl) with respect to the energy $E_{22000\text{ns}}$ that was deposited in the crystal. The upper image shows the case when the XFEL beam was turned off. The lower image shows the case when the beam was turned on.

Belle II calorimeter [1] and at other experiments [26, 45]. The charge ratio is defined as

$$R_{\text{PSD}} = \frac{E(t_{\text{short}})}{E(t_{\text{long}})} = \frac{\sum_{t=t_0}^{t_{\text{short}}} x(t)}{\sum_{t=t_0}^{t_{\text{long}}} x(t)}, \quad (7.1)$$

where t_{short} and t_{long} are the short and long time intervals. They are also referred to as short and long time gate.

The variable R_{PSD} offers information on the shape of the waveform, as different incoming particles can emit scintillation emissions which are slower or faster. An incoming particle that generates a faster scintillation emission will have a larger charge ratio than a particles that generates scintillation emissions at a slower time. The value for short time gate is determined by the material of the scintillator. For CsI(Tl), a value of $t_{short} = 1.2 \mu s$ is chosen as short gate to make it comparable to other studies, where this has also been reported as the optimal value for CsI(Tl) [26]. This value has also been applied for studies in CsI(Tl) for the Belle II electromagnetic calorimeter in [20], which serve as main comparison reference to the studies here. For the long time gate, a value of $t_{long} = 22 \mu s$ has been chosen to consider as much of the full waveform as possible.

Figure 7.2 shows the distribution of the charge ratio with respect to the total energy deposited in the CsI(Tl) crystal. The upper image shows the case when the XFEL beam was not in operation. Cosmic muons are the primary source of energy deposits in the crystal in this case, as previously seen in Section 7.1. The ionizing muons result in a single band at constant value for the charge ratio. No energy dependence in the shapes of waveform produced by electromagnetic particles is observed.

The lower image in Figure 7.2 shows the case when the XFEL beam was turned on. During operation of the XFEL beam, a high energetic neutron flux is present [32] which leads to neutron interactions within the crystal. Several bands of neutron interactions in the CsI(Tl) crystal can be observed that were not present in the case of beam off. As past studies for the Belle II calorimeter [25] show, the scintillation emission due to hadronic particles is dependant on the dE/dx energy deposited at high ionization. Each of the bands are due to inelastic scattering processes of the neutrons in the CsI(Tl) crystal with different particles in the final state. The band closest to the band for cosmic muons belongs to the case where a single proton is emitted from the scattering, while the band close above to it corresponds to elastic neutron scattering process where two protons are produced. The band further above these two is due to scattering process

where the neutron produces an alpha particle.

7.3 Optimization of short time window in pure CsI

The studies in this thesis are the first studies on the PSD abilities of pure CsI with the charge ratio method. Therefore, the optimal discrimination variable R_{PSD} is investigated with the goal to determine the optimal value for a short gate in Equation 7.1 which provides the highest separation between the neutron and muon waveforms.

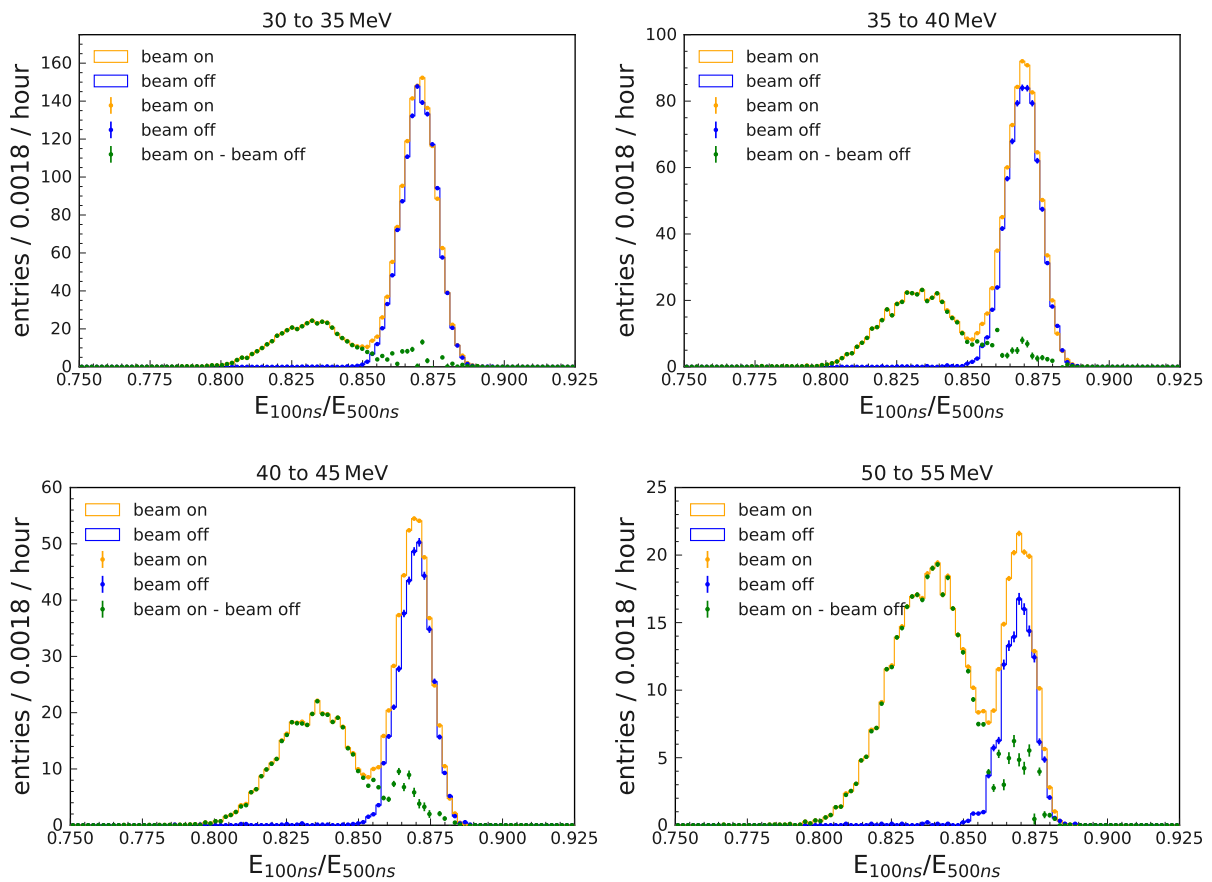


Figure 7.3: Histograms of charge ratios in a different energy ranges. In every image, the data in the case of XFEL beam off (blue) is subtracted from the data when the beam was turned on (orange). This results in the points marked in green.

Distributions of the charge ratio with a short time gate of 100 ns are shown in Figure 7.3 for different regions of constant energy. Data for the cases when XFEL beam was turned on and off is shown in comparison. The distributions for the case of no beam

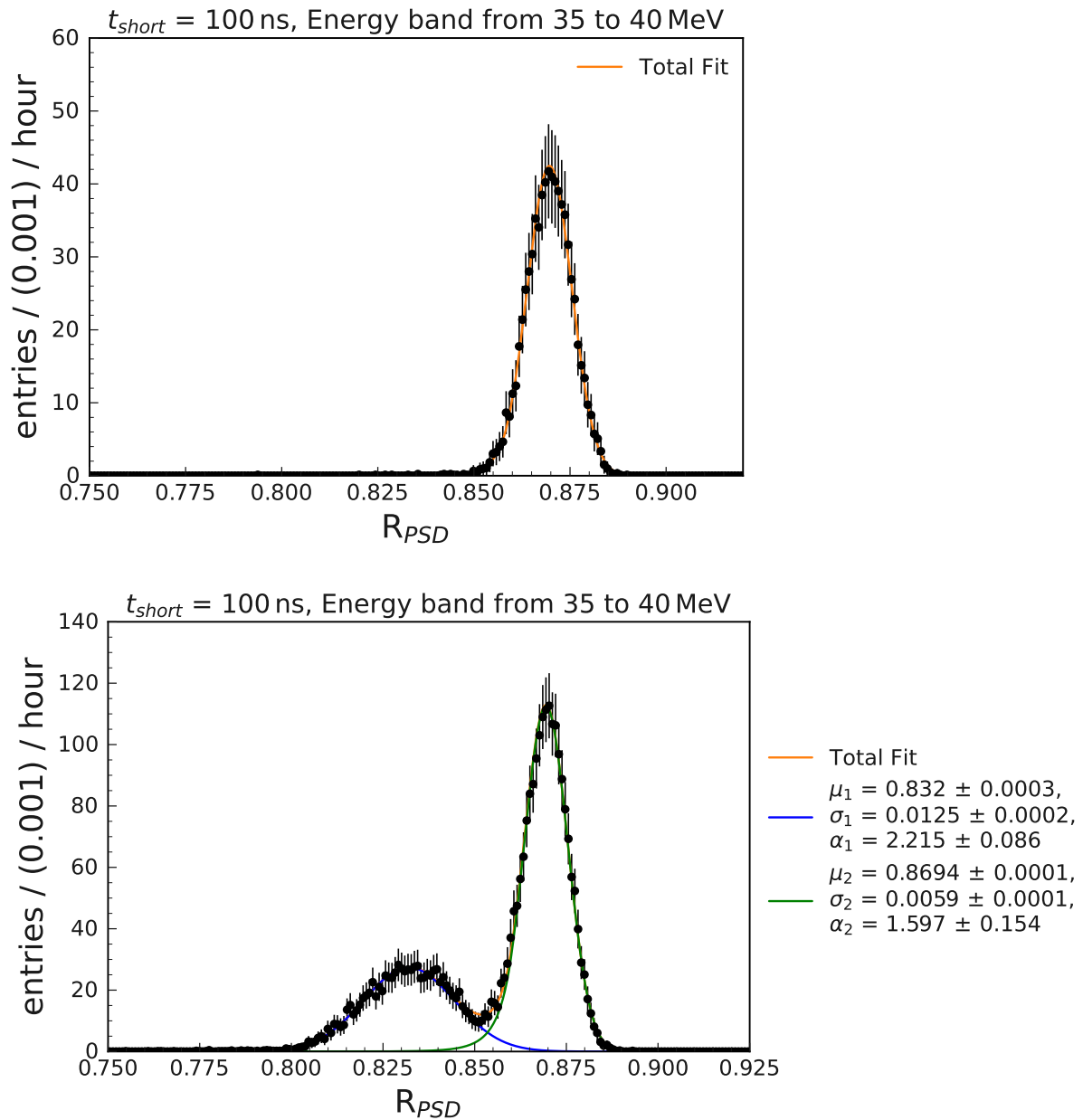


Figure 7.4: Charge ratio distributions in pure CsI for the energy range between 35 and 40 MeV, using a short time gate of 100 ns. The top plot shows the case where the XFEL was not in operation, while the bottom one shows the case when XFEL operation was turned on. Data points are shown in black. The orange curve shows the total fit, while the blue line shows the fit to the cosmic muon peak and the green line shows the fit to the neutron peak.

operation show one peak, whereas a second distinct peak is present in the case when the beam was in operation. The peak which is present regardless of the XFEL operation is due to the cosmic muon flux, while the peak that is only seen in the beam on data

is a consequence of the neutron flux. The peak from cosmic muon has a higher charge ratio value, while the other peak that entails the waveforms from neutrons is at value of lower charge ratios. This shows that energy deposits of neutrons entail a scintillation component that is slower than the scintillation constants for muons.

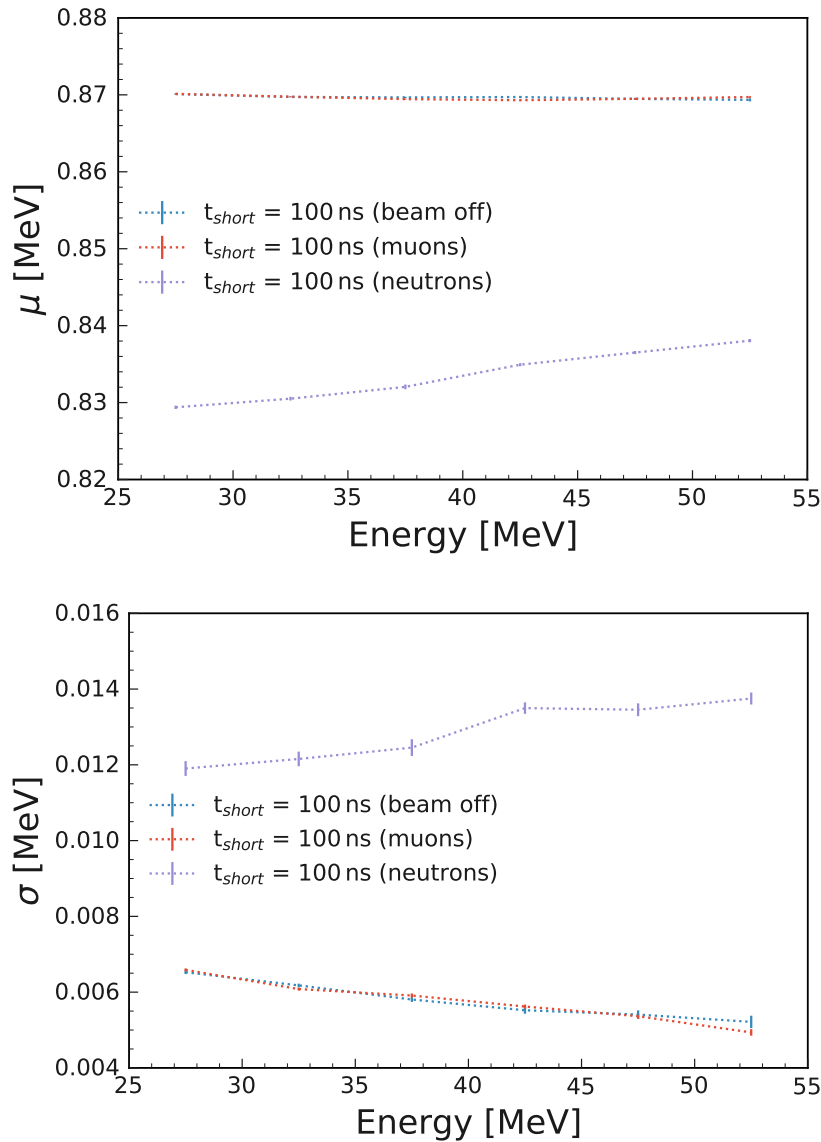


Figure 7.5: Extracted mean values μ (top) and widths (bottom) of the Crystal Ball fit functions for the case of no XFEL operation (blue). The red points correspond to the peak due to muons in case of beam operation at XFEL, while the purple points belong to the peak due to neutrons. Points are connected to guide the eye. Errorbars are included.

To obtain the optimal value for a short time gate, a scan over various short time

gates is performed. Values of the short time gate between 40 ns and 200 ns are considered in steps of 10 ns. The long time gate is kept constant at 500 ns. The charge ratio distributions are studied in regions of constant energy that range from 25 to 55 MeV, scanned in steps of 5 MeV. These energy windows were chosen because the most events of both muons and neutrons are expected here, as already seen in the simulation in Figure 5.2 and in the results from data in Figure 7.1.

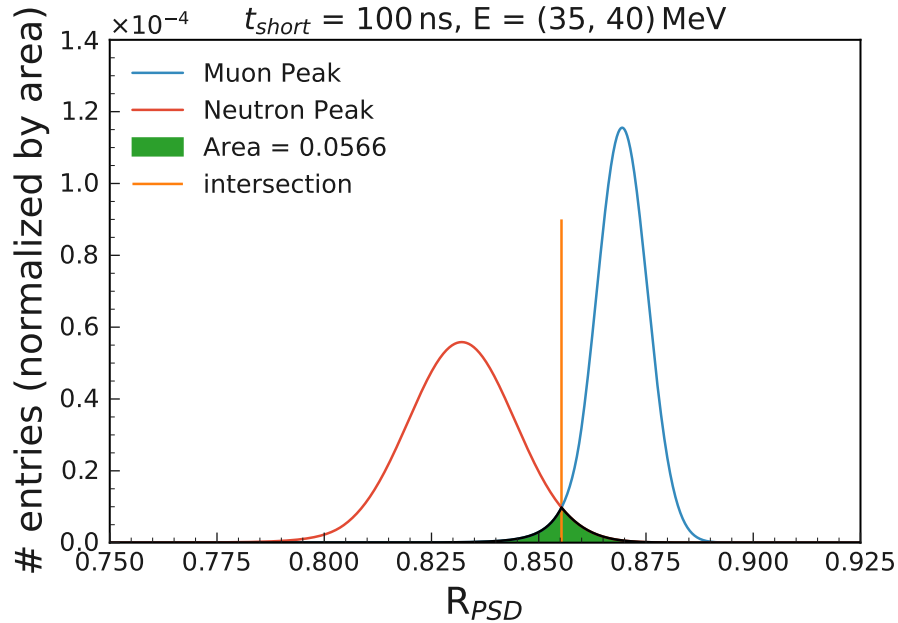


Figure 7.6: Charge ratio distributions in pure CsI for short time gate of 100 ns in the energy range from 25 to 30 MeV. Data points are shown in black. The orange curve shows the total fit, while the blue line shows the fit to the cosmic muon peak and the green line shows the fit to the neutron peak.

Fits are performed on the distribution of the data recorded when the XFEL beam was turned on. The distribution of each of the chosen t_{short} is fit separately for energy range. An example fit for the case of $t_{short} = 100$ ns in the energy range of 35 to 40 MeV is shown in Figure 7.4. Fits for all scanned energy ranges and tested short gate values are shown in the Appendix B. The case for no XFEL operation is shown, where the shape of the distribution can be described with a single Crystal Ball function, according to Equation 6.3. All parameters except n are left floating in the fit. The case when the beam was turned on is shown in direct comparison. The total fit model in this case consists of the sum of two Crystal Ball functions where each of the Crystal

Ball function describes one of the peaks. Again all parameters except n are left floating in the fit. Each of the peaks in the beam on data belong to either the muon or neutron waveforms. The fit for the muon peaks also resembles the distribution of the beam off data, confirming that the additional peak is present due to the incoming neutron flux. It confirms that each of the peaks corresponds to their muon or neutron waveforms.

The fit parameters of the Crystal Ball are extracted from the fits. The means and widths of the Crystal Balls from the fits to the beam off data and the beam on data are shown in Figure 7.5. The results for a charge ratio with a 100 ns short gate are shown for different energy ranges. The values of the peaks and the widths for the beam off case are in agreement with the fits to one of the peaks in the beam on case, confirming again that this peak component is due to the constant present of the cosmic muon flux.

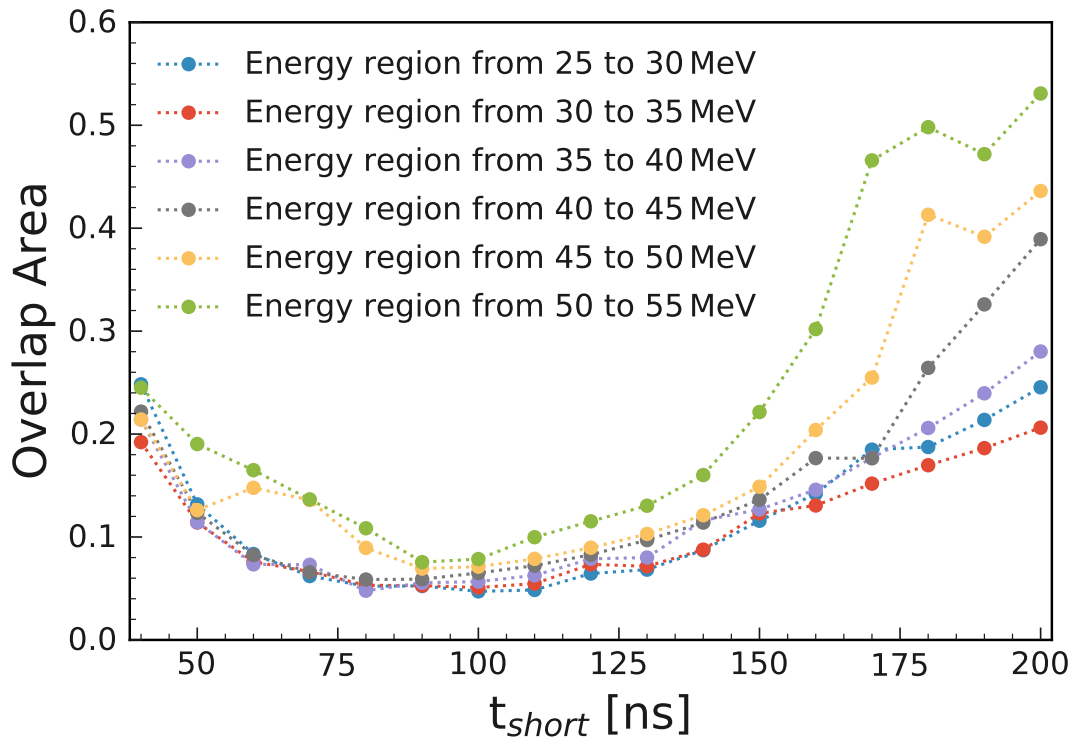


Figure 7.7: The overlap area of the distributions of muon-like and neutron-like waveforms with respect to the applied short gate, shown for various energy bands. Each series of points correspond to a 5 MeV wide energy region and is connected with the thin dotted line.

To quantify the separation power, the functions of the two components of the total fit on the beam on data are normalized to an area of one. This is shown in Figure 7.6

for a short gate of 100 ns in the energy range between 25 to 30 MeV. The images for all scanned energy ranges and every tested short gate value are shown in the Appendix B. It can be seen that the distribution of the muon waveform has an overlap with the distribution for neutrons. The overlap area of the two distribution quantifies the separation of the two types of particles. In case of an ideal separation, there would be no overlap between the two distributions. Therefore, the ideal short time gate values corresponds to the case with the minimal overlap.

The separation power in each of the energy regions is shown in Figure 7.7. The energy regions between 25 and 40 MeV have the least areas of overlap, regardless of the short time gate. The overlap is largest for short gates below 50 ns and values above 150 ns. It can be seen that in every of the energy regions, the distributions show a local minimum in the region between 60 and 130 ns. This is furthermore visible in Figure 7.7 which shows the overlap area with respect to the energy deposit in the crystal. The minimal overlap areas are accomplished in for the short time values of between 80 to 100 ns. Through all regions of energy, the value at 100 ns has the strongest separation power. The global minimum value is accomplished at a short time of $t_{short} = 80$ ns in the energy region from 35 to 40 MeV. Overall this allows the conclusion that good separation can be accomplished with short time gates between 60 and 130 ns, which highlights the robustness of this method.

A complete overview of the separation power in all scanned energy regions and for all short time gates can be seen in Figure 7.9. It shows the overlap area for each of the tested short gates in dependence to the energy region. It shows that a good separation can be accomplished in the energy regions between 25 to 40 MeV. This energy region also corresponds to the region with the most energy deposits from cosmic radiation and in general is the region with the highest number of events in this study. The overlap area increases at higher energies, which means the separation power decreases. It is lowest in the energy region from 50 to 55 MeV and with the short time gate values of 180 ns and higher. In general, the minimal overlap area can be found for short time gates of between 80 to 110 ns. The ideal value is found to be at 100 ns. For this val-

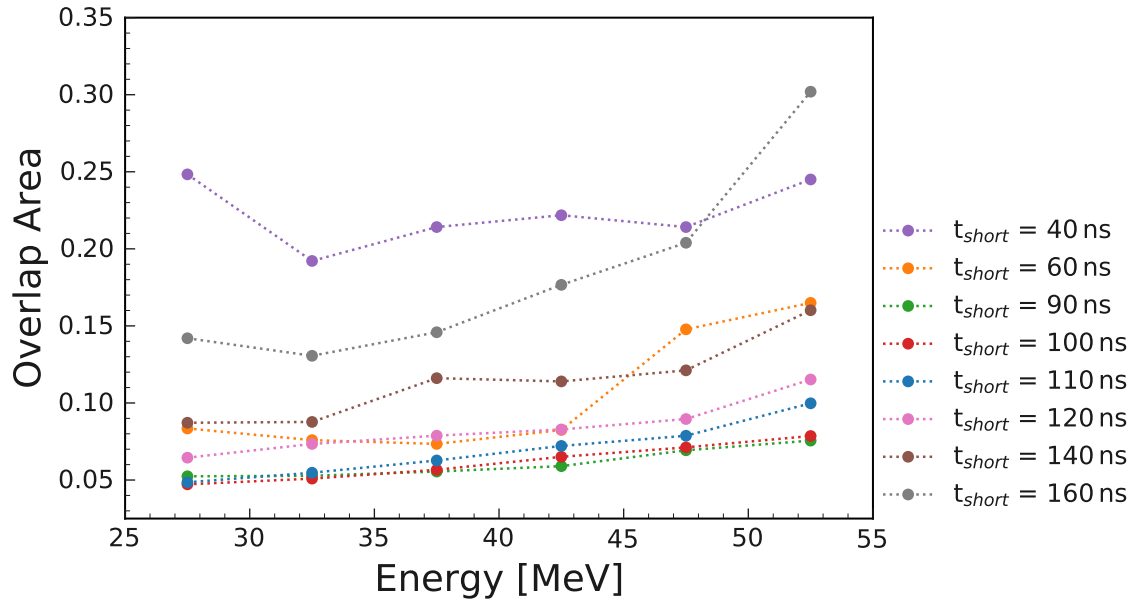


Figure 7.8: The overlap area of the distributions of muon-like and neutron-like waveforms with respect to the energy deposited, shown for various short gates. Each series of points correspond to a chosen short gate. The points are placed in the center of the energy regions and connected with the thin dotted line.

ues, the overlap area is below 10% over the whole energy range is accomplished. This allows the highest separation of the muons from neutrons. The smallest overlap area was found with a short gate of 100 ns in the energy region between 25 and 30 MeV, with an overlap of 0.047. This corresponds to samples of 95.3% purity in each of the samples. The results of this study shows that the difference in the pulse shapes are due to differences in the tail of the waveform, since the main scintillation decay time of pure CsI is 16 ns [27].

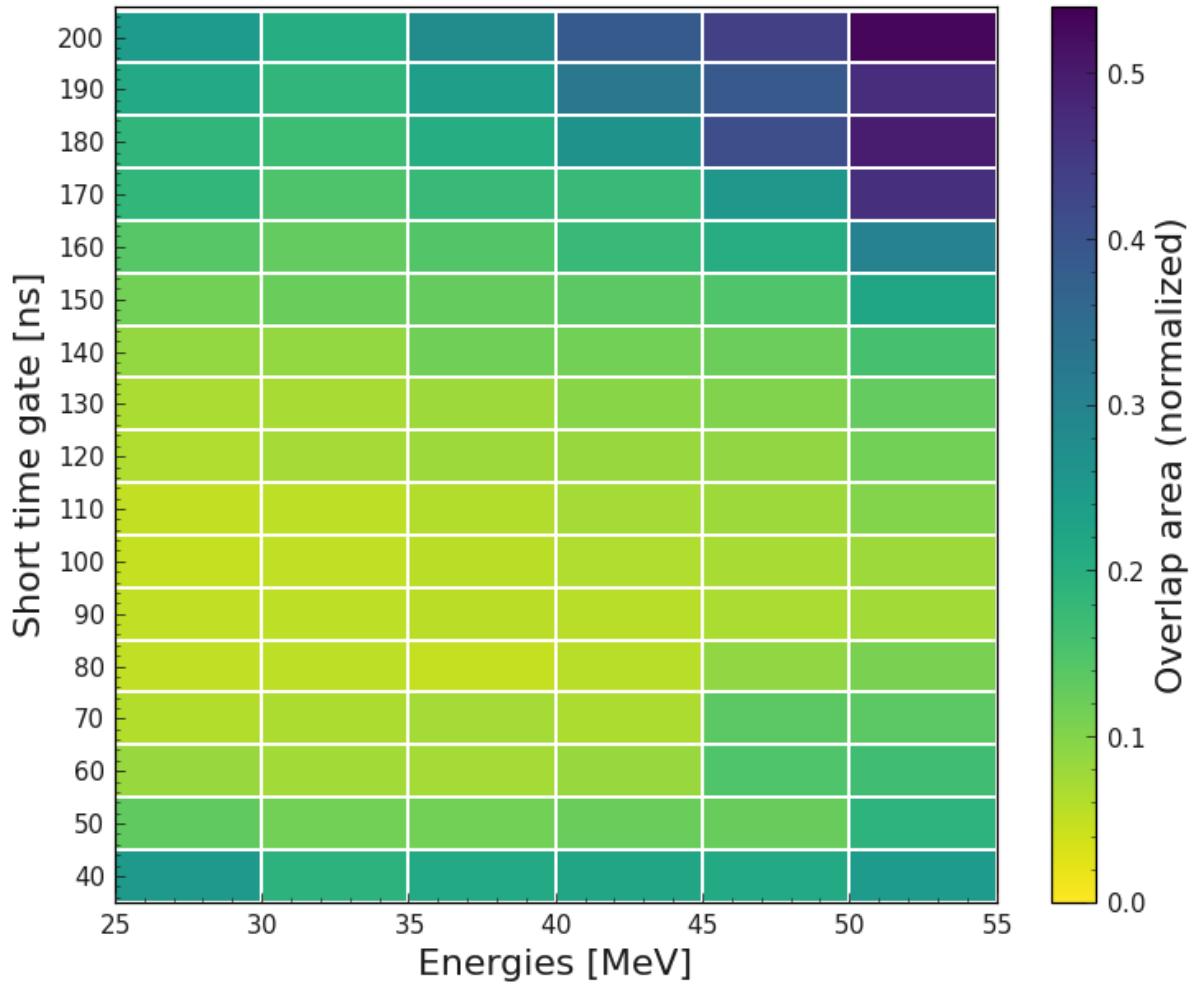


Figure 7.9: The overlap area between the distributions of muon-like and neutron-like waveforms, shown with respect to the applied short time gates and the energy range. The energy range cover the energies in the interval indicated by the edges of the bins. The short time gates are according to the center of the bin. Overlap areas with small values are colored in yellow, while values with higher overlap are shaded in blue.

7.4 Charge ratio method in pure CsI

The charge ratio method is applied for pure CsI based on Equation 7.1 with a short time gate at 100 ns and a long time gate of 500 ns. The charge ratio for pure CsI with respect to the energy deposits is shown in Figure 7.10.

The data shown is recorded under the same conditions and simultaneously to the data that was shown for CsI(Tl) in Section 7.2. Therefore the incoming particle flux is expected to be similar. The top image shows the case when XFEL was not in operation, while the bottom shows the case when the beam was turned on. The case for beam off shows the events where cosmic muons ionize in the pure CsI crystal as there is only cosmic radiation present. These events are at a constant charge ratio value, independently of the total energy deposit. The shape is comparable to what is also observed in CsI(Tl). However, the distribution is wider in the pure CsI crystal, showing the poorer resolution in pure CsI. This is observed due to the lower light yield of pure CsI. When the XFEL beam is turned on, events due to neutron interactions with the scintillator become visible. They form a band below the band for cosmic muons. Similar interactions of the neutron are expected to happen in both crystals, as the pure CsI and CsI(Tl) crystals have the same dimensions and have similar chemical material properties. Therefore, inelastic scattering processes are expected to happen in the scintillator material. There is only one distinct band is observed for the neutron interactions. It displays no further structure, unlike in the case of CsI(Tl), where several bands were observed in dependence to the secondary particle produced in the inelastic scattering process of the neutron with the scintillator material. This distinction is not possible in the pure CsI. The band furthermore shows no energy dependence and is located below the band for the muons. This indicates that neutrons with energy deposits have a generally slower scintillation emission than the muons regardless of the energy deposited in the crystal. Since it is not possible to distinguish between the particles created in the inelastic scattering, a scintillation mechanism different to CsI(Tl) can be responsible for the different pulse shapes. In the CsI(Tl), the hadronic interactions lead to an additional scintillation component that was dependant on the dE/dx of the incoming

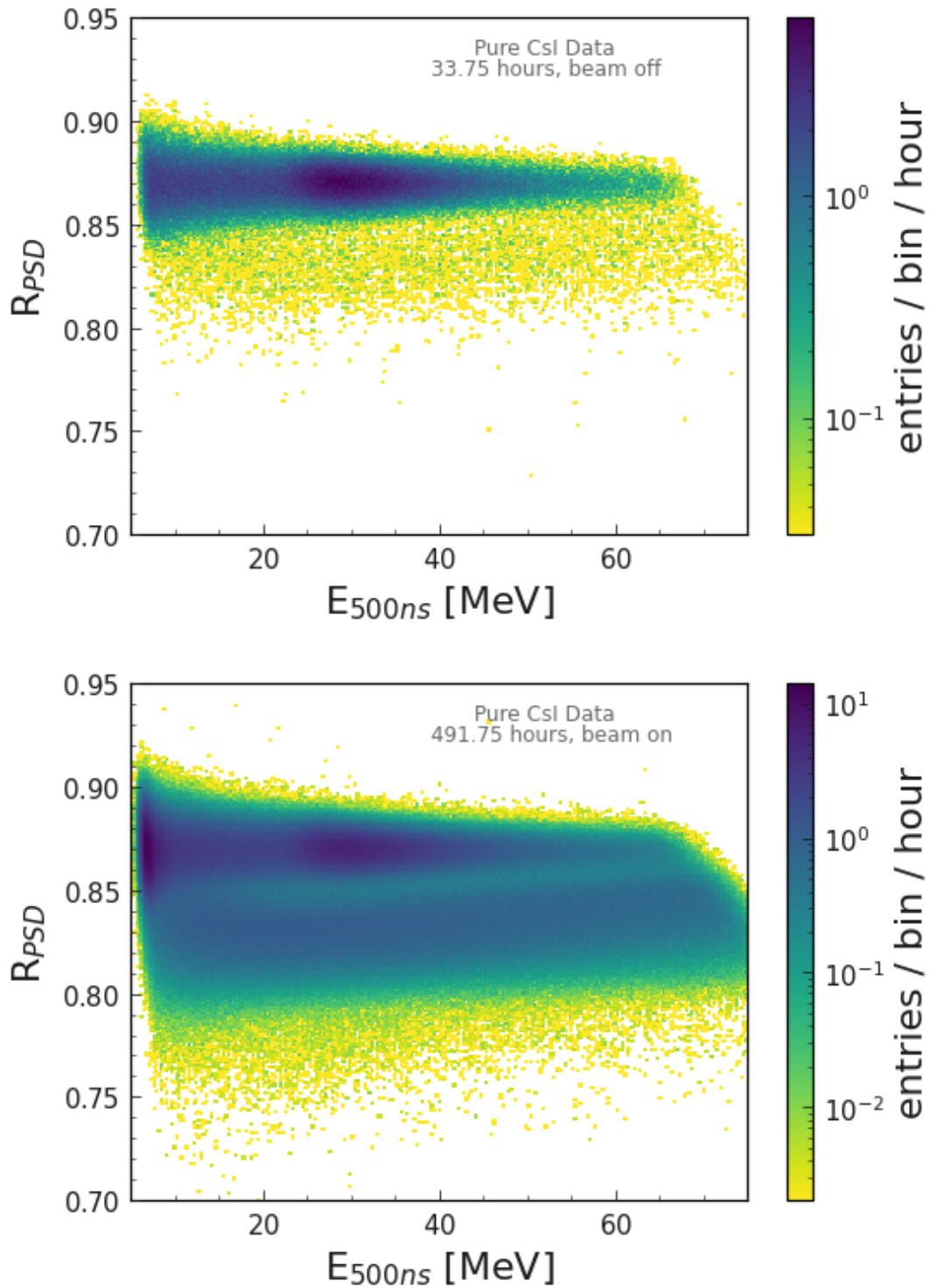


Figure 7.10: Distribution of the charge ratio R_{PSD} in pure CsI with respect to the energy E_{500ns} that was deposited in the crystal. The upper image shows the case when the XFEL beam was turned off. The lower image shows the case when the beam was turned on.

particles. In pure CsI, it is not clear why the neutrons are at a generally lower charge ratio. The energy independence of the charge ratio could indicate that the pulse shape difference is not due to the dE/dx . A different mechanism than the mechanism for CsI(Tl) appears to be responsible for the different waveform shapes and the additional scintillation component for energy deposits from hadronically interacting particles in pure CsI.

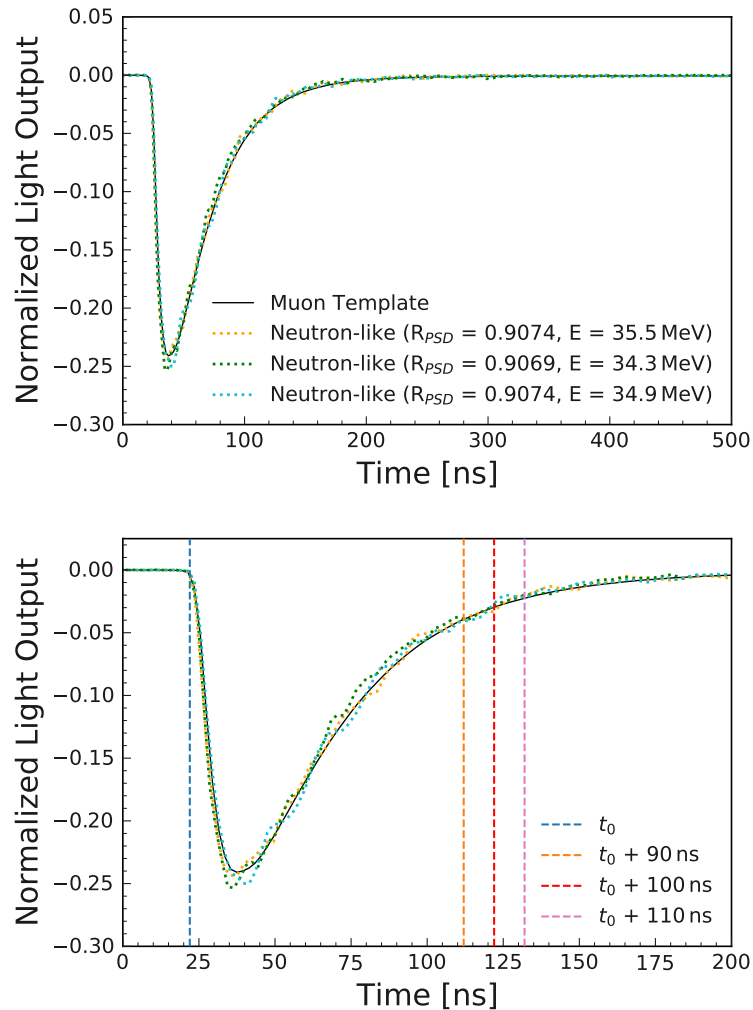


Figure 7.11: Normalized waveforms recorded with the pure CsI crystal. The solid line shows a (OF) template of the average over muon waveforms. The dotted lines show examples of three individual neutron waveforms. The left side shows the waveform over the whole long integration window. The right side shows the same waveforms, zoomed into a shorter time window. Marked with dashed lines are the short time gates t_{short} of 90, 100 and 110 ns.

The difference of muon-like and neutron-like waveforms is shown in Figure 7.11. A

template of a normalized typical muon waveform is shown in comparison to three individual neutron-like waveforms is shown. The muon template was created using the QETpy analysis tools from [41]. It is created from data that was recorded in general laboratory environment with no neutron flux present and therefore offers a sufficiently pure sample of muon-like waveforms. The neutron-like waveforms are selected based on their charge ratio and with similar energies, to emphasise the differences in shape.

Most differences in the waveforms are observed in the tail of the waveforms, in the region after 50 ns. The scintillation light output of the muon-like waveform is higher, which indicates that it has a faster scintillation time. Meanwhile the neutrons-like waveforms have a lower light output in this time window, which indicated a longer decay time of the scintillation. The short time gates t_{short} are marked as well. In the computation of the charge ratio, the region between t_0 and the chosen short time gate is compared to the full waveform integral. Comparably good separation is found to possible with short time gates between 90 to 100 ns. The optimal separation has been found to be accomplished with a short time gate of 100 ns. This leads to the conclusion that the main difference between neutron-like and muon-like waveforms is observed in the region from 90 to 100 ns. Since this is the case in various energy regions that were scanned in the study, one can conclude there is a general difference in the scintillation mechanism of electromagnetic particles and hadronic particles in pure Csl.

Chapter 8

Conclusions and Outlook

This thesis presents one of the first quantitative studies of pulse shape discrimination in a single pure CsI scintillator crystal. The goal was to determine whether it is possible to perform a separation of electromagnetically and hadronically interacting particles based on the scintillation light output of the crystals. An experimental setup was designed for this task, featuring a single pure CsI crystal, and a CsI(Tl) crystal as reference. Scintillation waveforms from energy deposits of the cosmic muon flux and a high energetic neutron flux were evaluated for this study. A location above a beam dump pit of the XFEL was chosen to obtain the neutron data sample. Simulation studies in GEANT4 were done to test the expected energy deposits in pure CsI from the cosmic spectrum.

This analysis is performed on the level of individual waveforms, therefore a preselection is applied to ensure the quality of the waveforms. It is found that pure CsI has pulse shape discrimination abilities over the full probed energy range between 12 and 70 MeV. It is found that the difference in pulse shapes is due to differences in the tails of the waveforms.

Pulse shape discrimination is performed in this thesis based on the charge ratio method, which characterizes the pulse shape based on the ratio of the integrated scintillation light output over a short and a long time gate. The timing windows for CsI(Tl) are

chosen based on past studies. For pure CsI, this is the first study of pulse shape discrimination properties using the charge ratio method. Therefore an optimal short gate time is determined. The separation power between neutrons and muons is investigated with respect to the short gate time and the energy deposited in the crystal. The highest separation can be found at a short time gate of 100 ns. Short gate times between 80 to 110 ns provide an overall suitable separation power.

The data for the PSD studies was stored and analysed offline. Future studies using this experimental detector setup could test a real-time approach to perform pulse shape discrimination. Using a machine-learning approach, a classifier could be trained to apply PSD.

Since this study only tested variations of the short gate in the charge ratio, further studies could investigate the optimal long gate. It is furthermore found that the pulse shape differences in pure CsI are not dependent on the dE/dx as observed in CsI(Tl). Furthermore, only the charge ratio method is applied for PSD in this study. Following studies could test the PSD performance of pure CsI based on other pulse shape analysis methods, such a template fit method. Template fit are applied for the CsI(Tl) scintillators at Belle II. Therefore it will be of interest to study the implementation of this method with pure CsI.

It has been found that the results from the charge ratio in pure CsI allow PSD, however the observed results differ from CsI(Tl). This could be due to different scintillation mechanisms in pure CsI. Further simulation-based studies could be performed to obtain an insight to this phenomena and allow a better understanding of the origin of the different scintillation mechanisms in pure CsI compared to CsI(Tl).

Appendix A

Shielding of the crystal setup

The following Figures show detailed drawings of the housing used for the experimental setup described in Chapter 4.

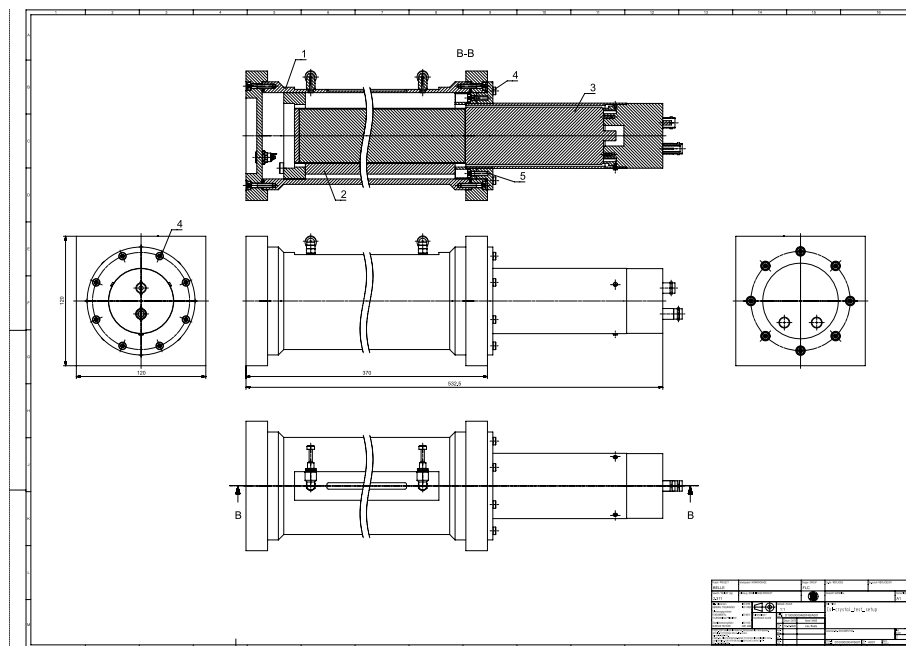


Figure A.1: Technical drawings of the shielding for the setup. Dimensions for the front and rear side are stated.

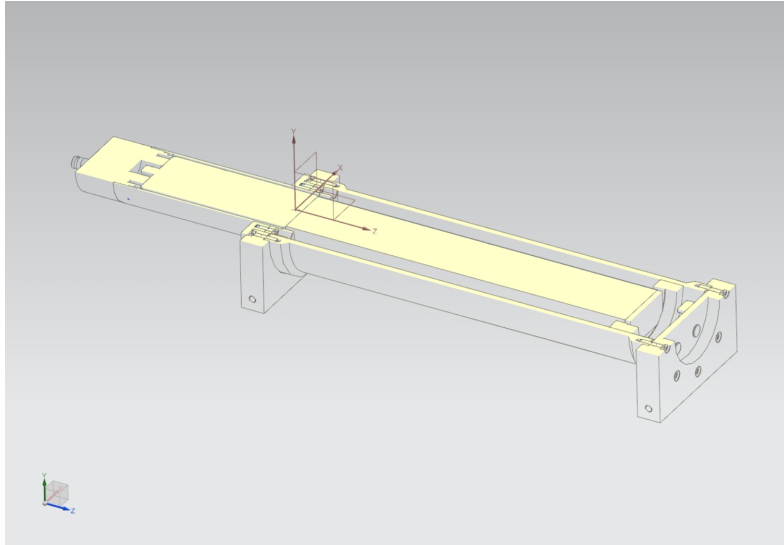


Figure A.2: 3D model of the shielding for the setup with open view into the xz -plane.

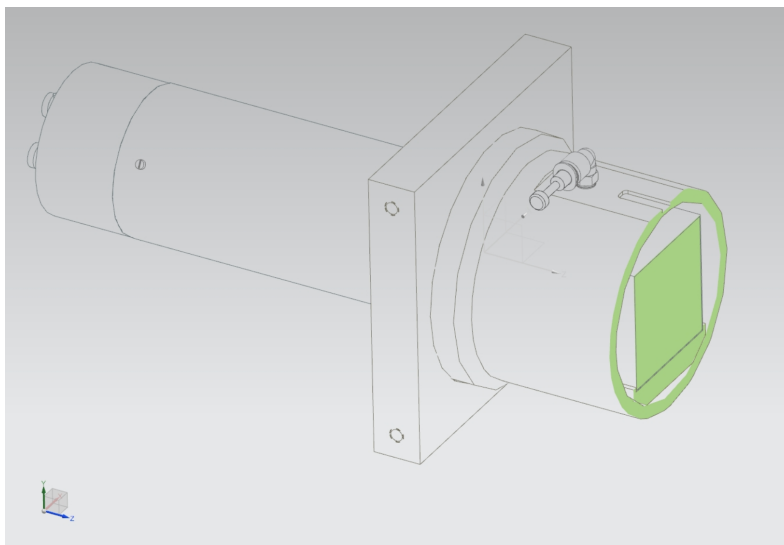


Figure A.3: 3D model of the shielding for the setup with open view into the xy -plane.

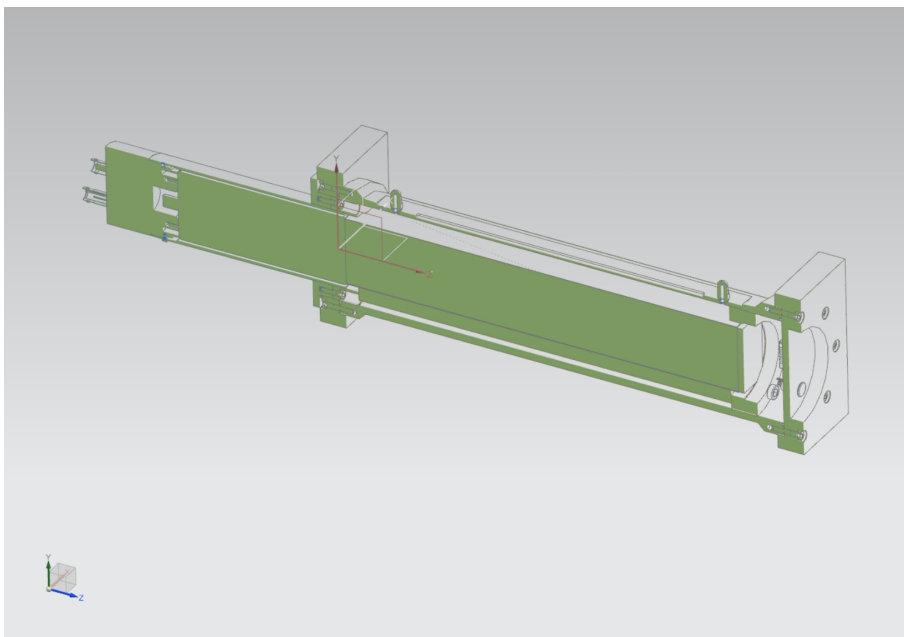


Figure A.4: 3D model of the shielding for the setup with open view into the yz -plane.

Appendix B

Short time gate for pure CsI

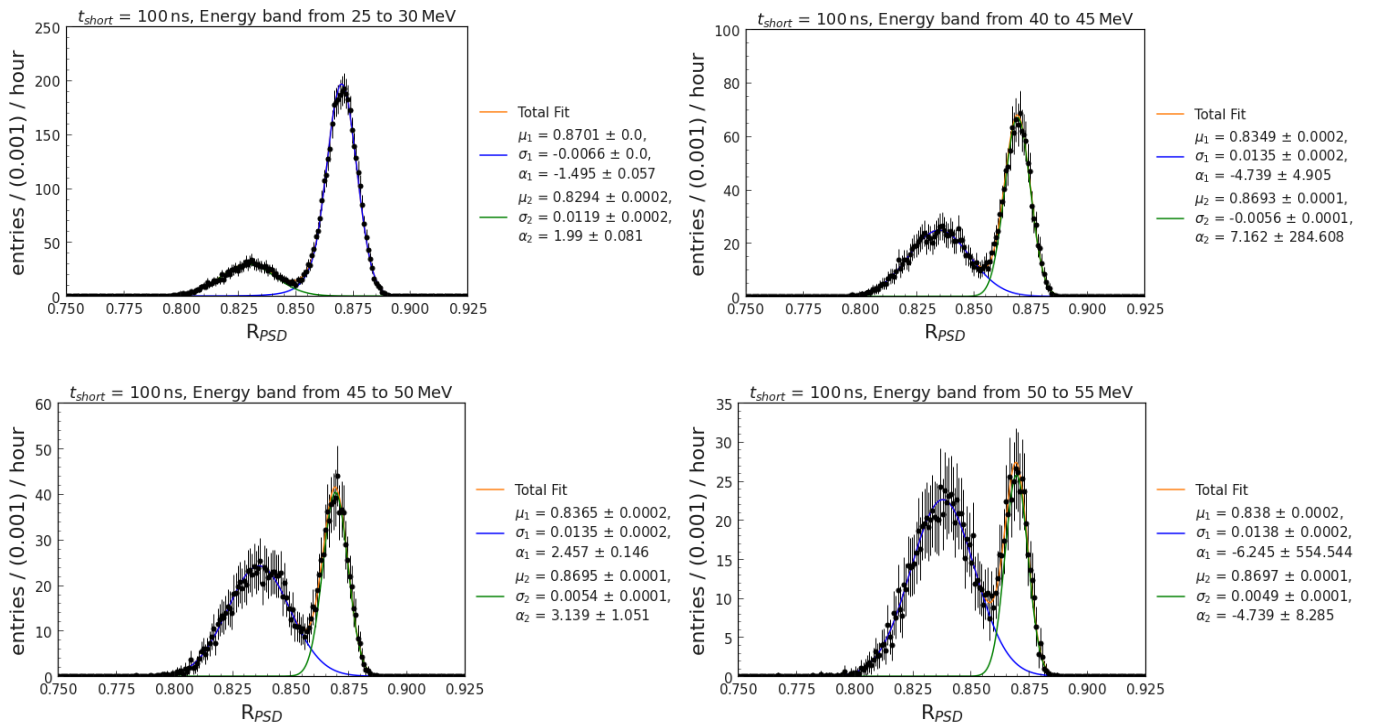


Figure B.1: Charge ratio distributions in pure CsI for different energy ranges, all using a short time gate of 100 ns. Data points are shown in black. The orange curve shows the total fit, while the blue line shows the fit to the cosmic muon peak and the green line shows the fit to the neutron peak.

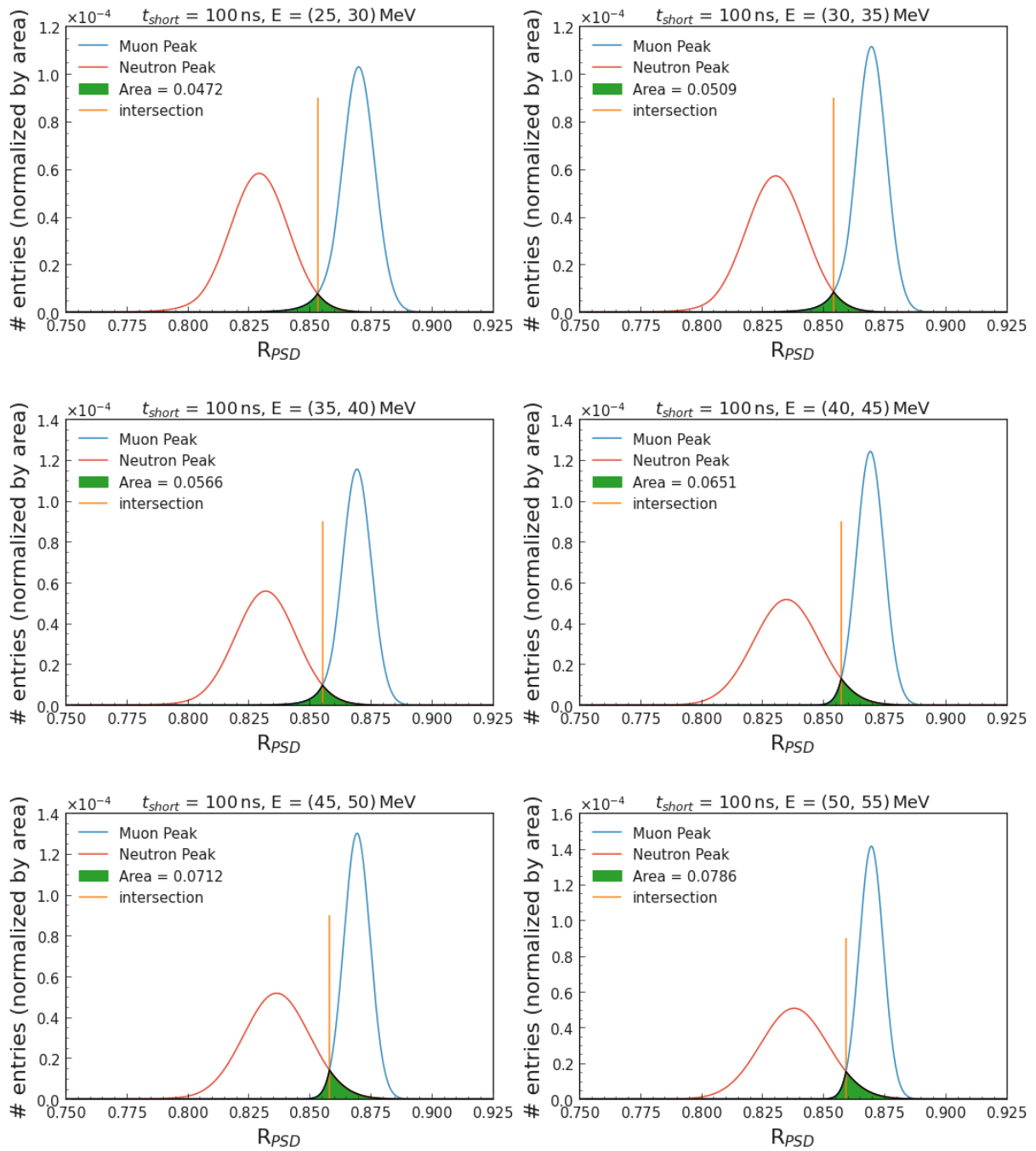


Figure B.2: The components of the fits to the charge ratio distributions in pure CsI in different energy ranges, all using a short time gate of 100 ns. The blue line shows the fit to the cosmic muon peak and the green line shows the fit to the neutron peak, both functions are normalized to an area of 1. The orange line shows the intersection point of both function and the green area marks the area of overlap.

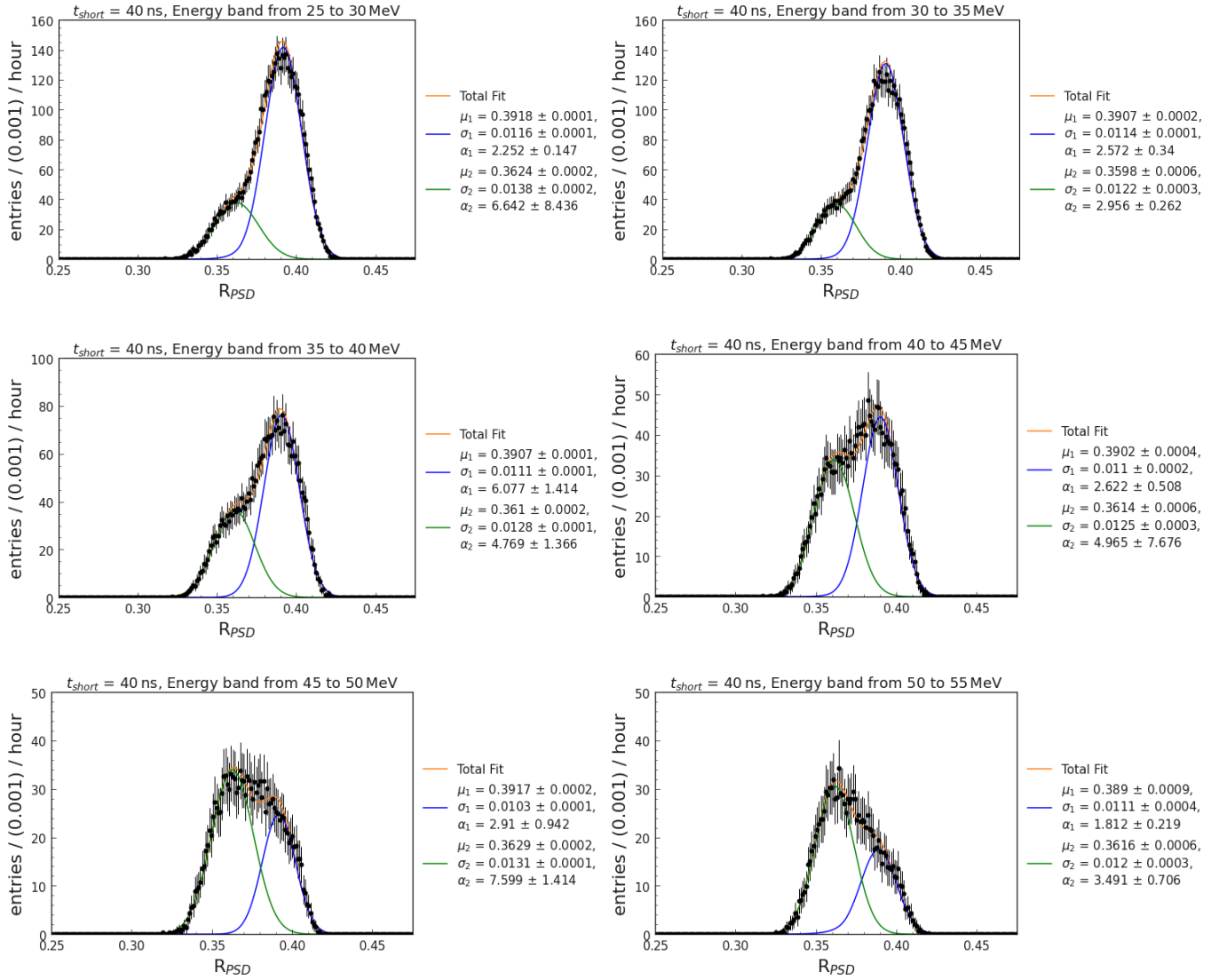


Figure B.3: Charge ratio distributions in pure CsI for different energy ranges, all using a short time gate of 40 ns. Data points are shown in black. The orange curve shows the total fit, while the blue line shows the fit to the cosmic muon peak and the green line shows the fit to the neutron peak.

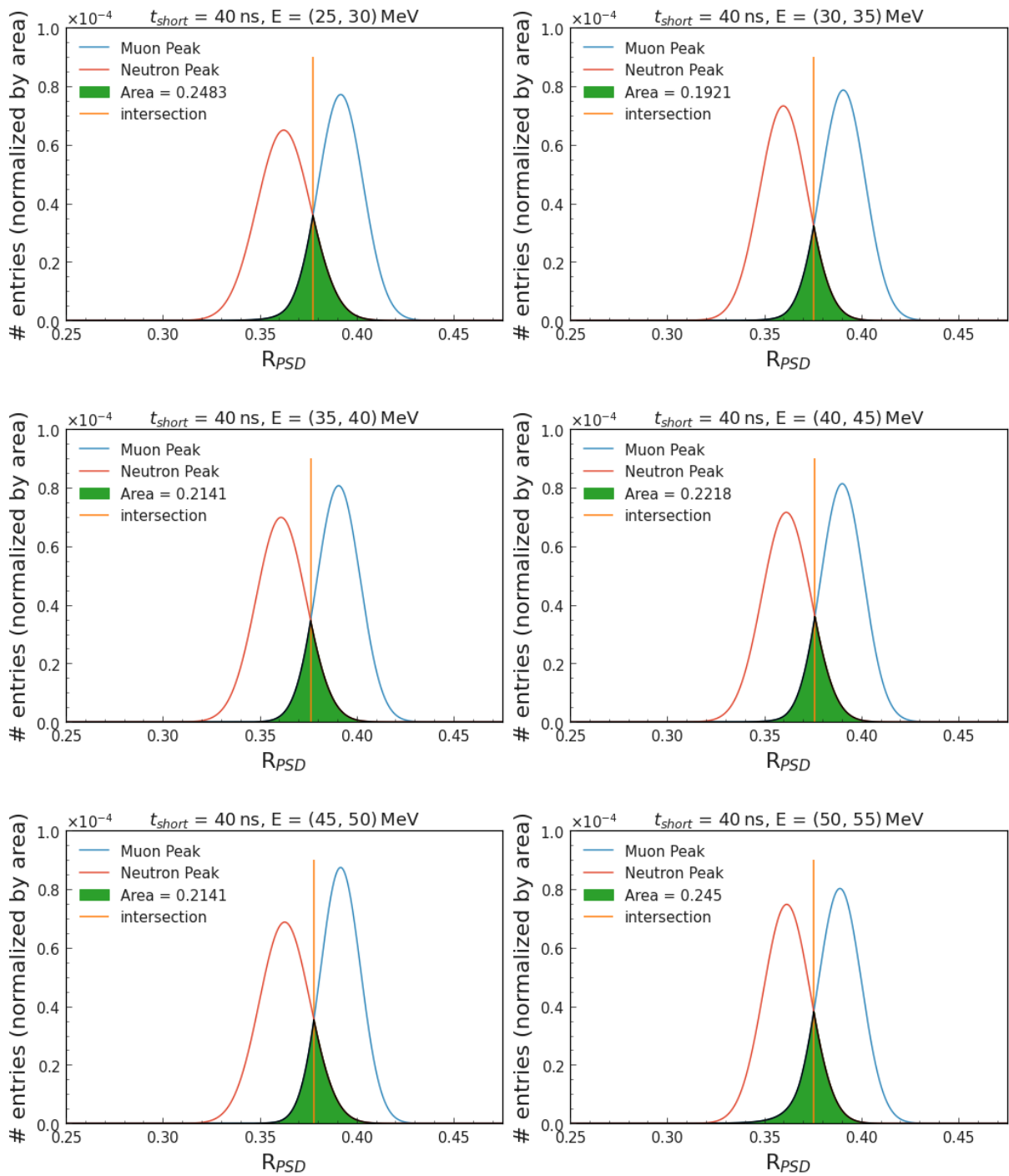


Figure B.4: The components of the fits to the charge ratio distributions in pure CsI in different energy ranges, all using a short time gate of 40 ns. The blue line shows the fit to the cosmic muon peak and the green line shows the fit to the neutron peak, both functions are normalized to an area of 1. The orange line shows the intersection point of both function and the green area marks the area of overlap.

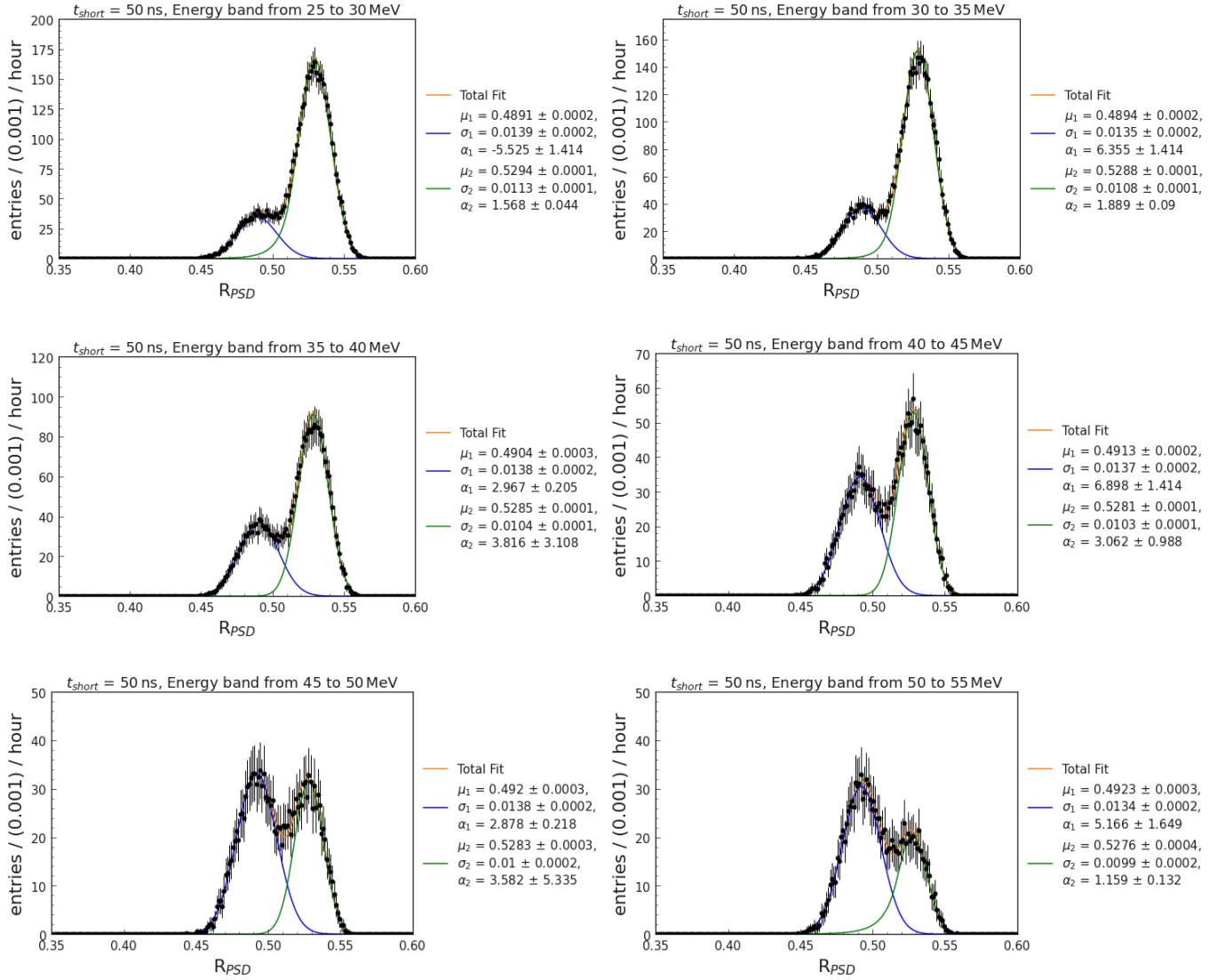


Figure B.5: Same as Figure B.3 but here with a short gate of $t_{short} = 50$ ns.

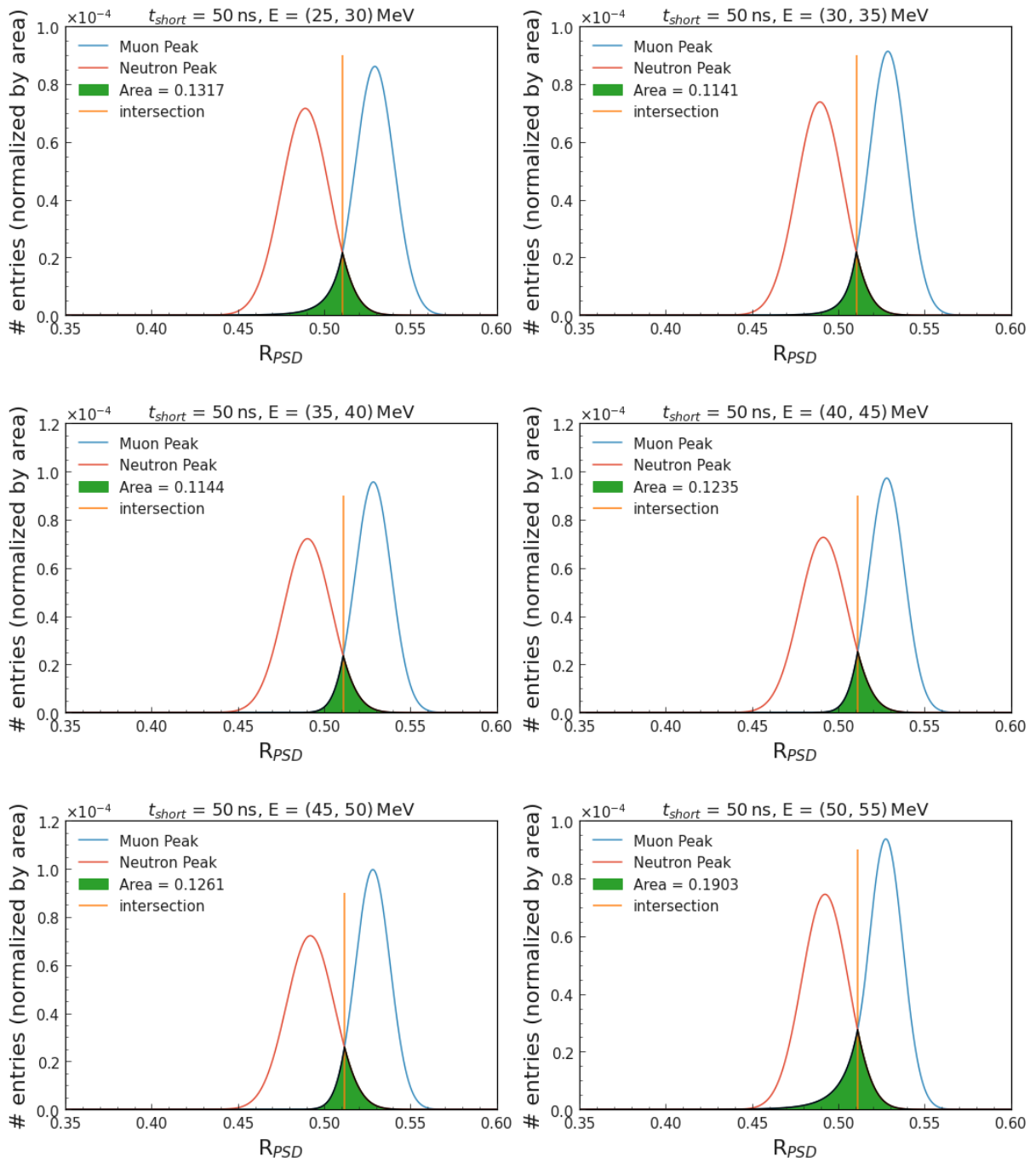


Figure B.6: Same as Figure B.4 but here with a short gate of $t_{short} = 50$ ns.

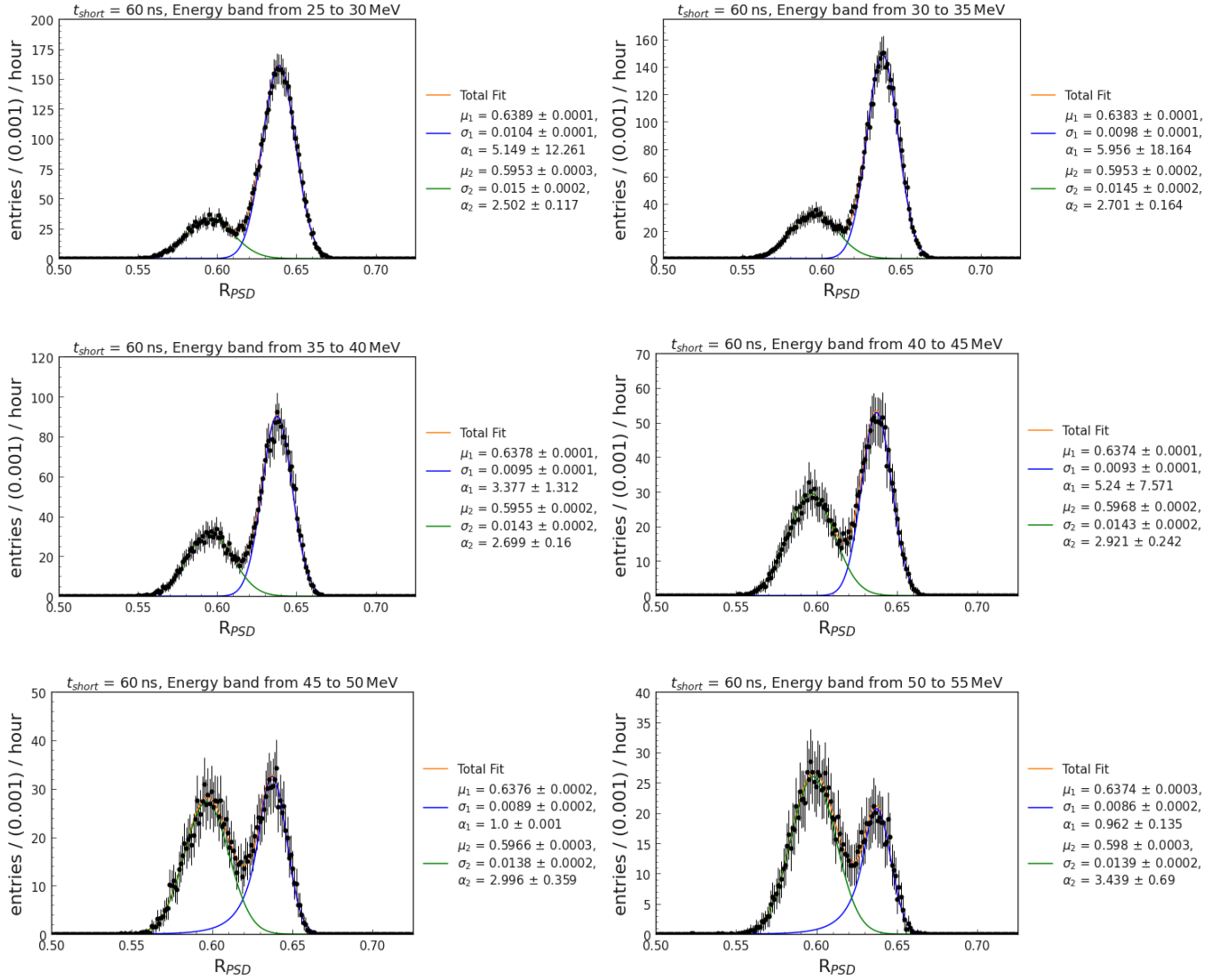


Figure B.7: Same as Figure B.3 but here with a short gate of $t_{short} = 60$ ns.

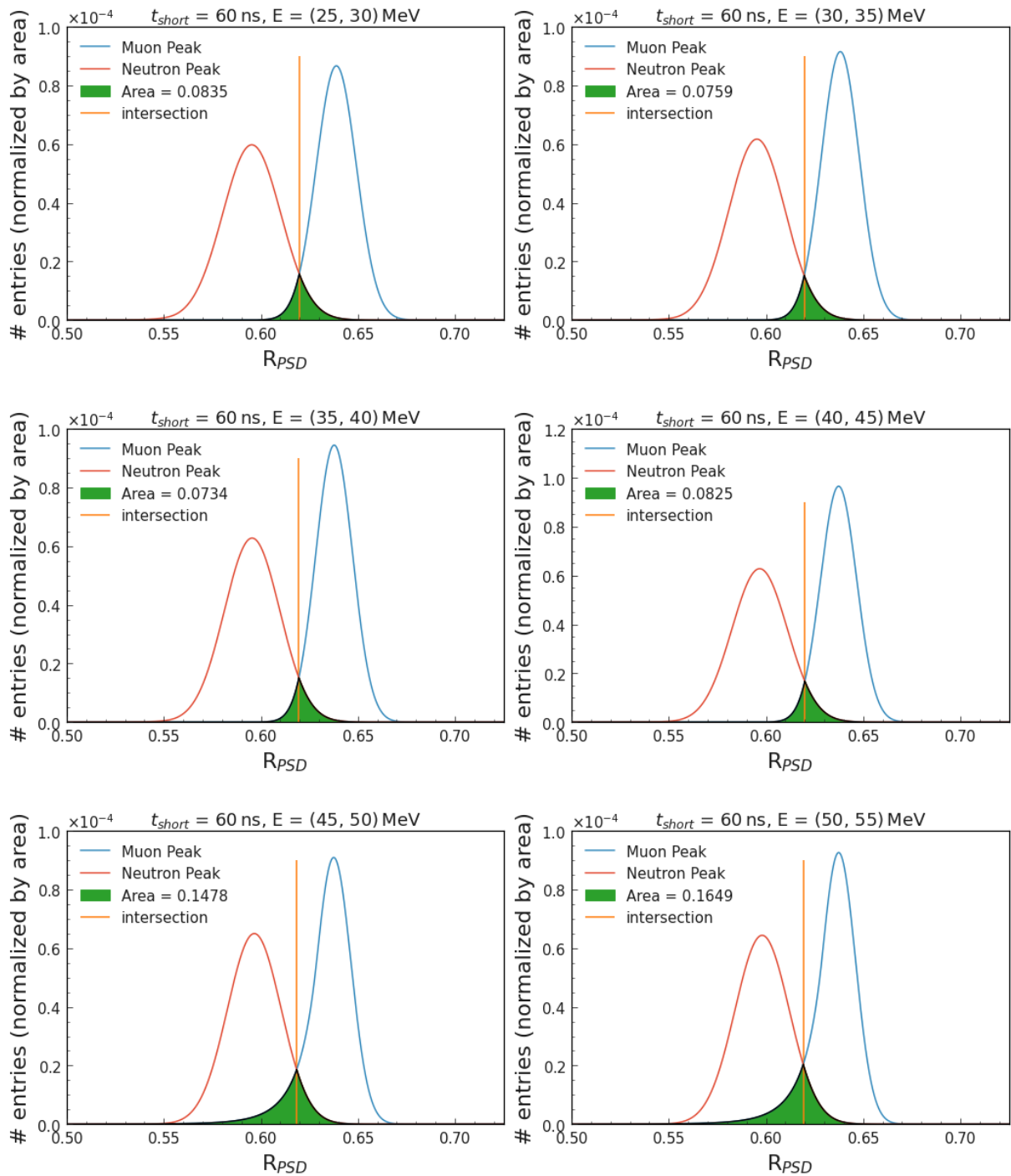


Figure B.8: Same as Figure B.4 but here with a short gate of $t_{short} = 60$ ns.

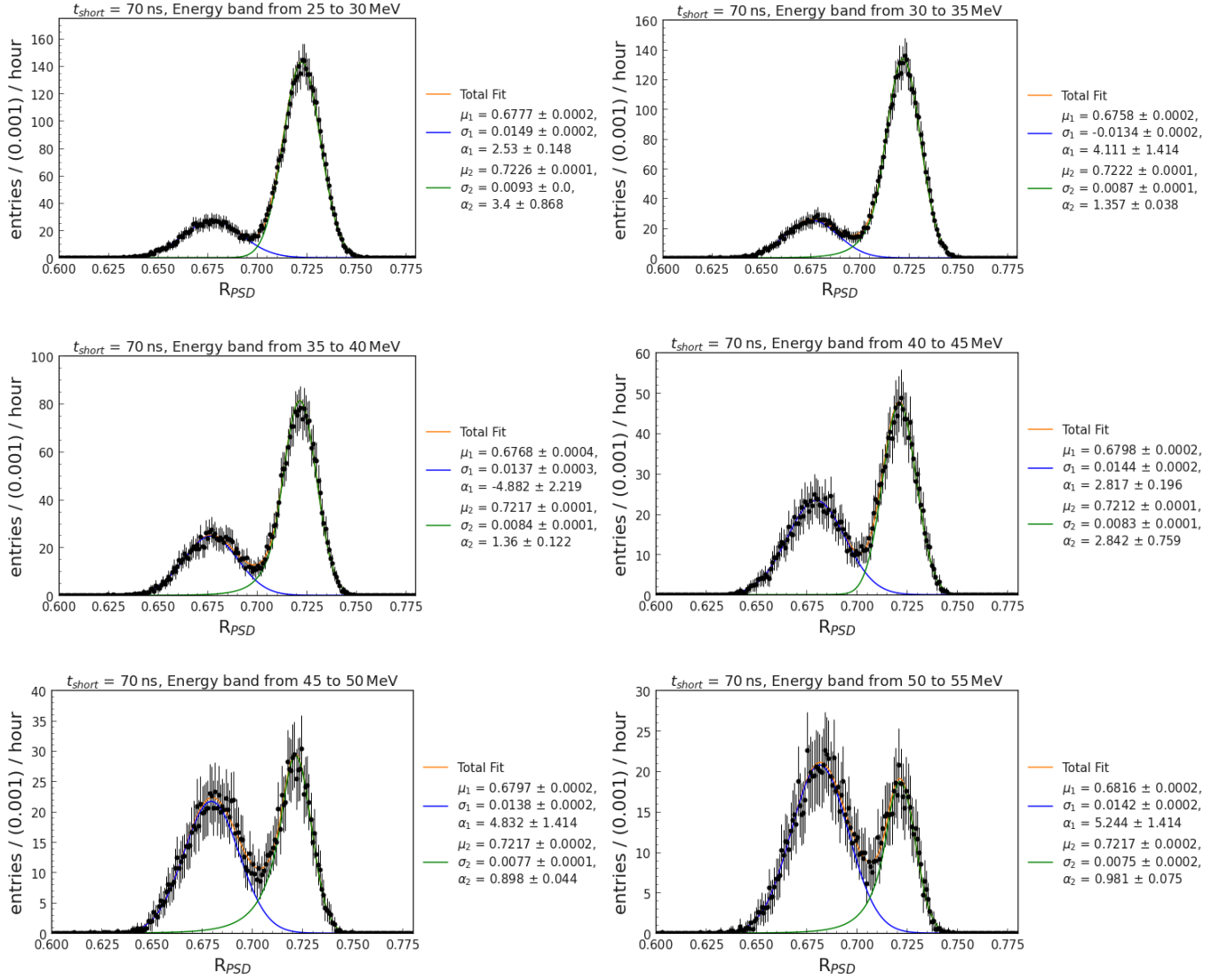


Figure B.9: Same as Figure B.3 but here with a short gate of $t_{short} = 70$ ns.

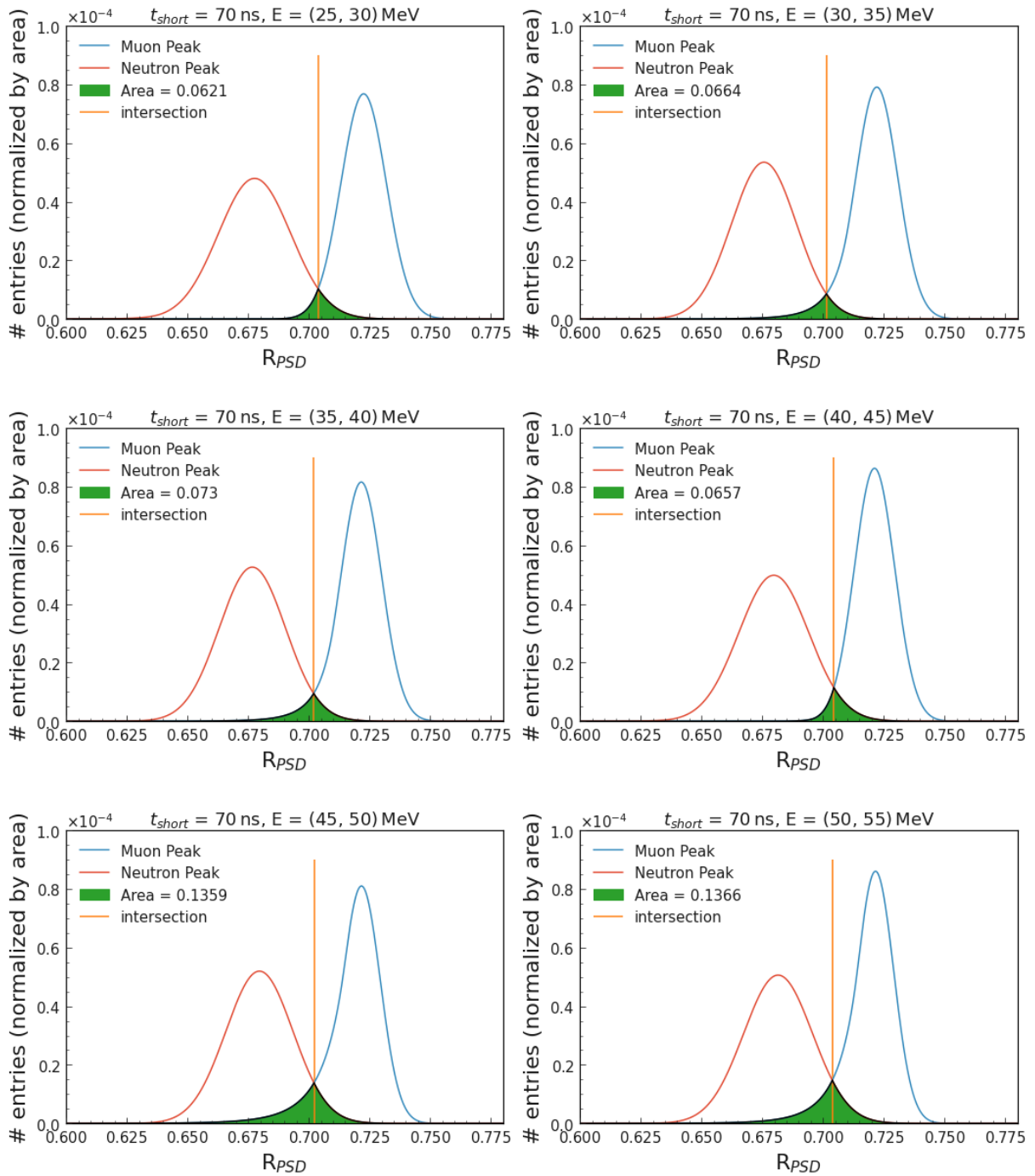


Figure B.10: Same as Figure B.4 but here with a short gate of $t_{short} = 70$ ns.

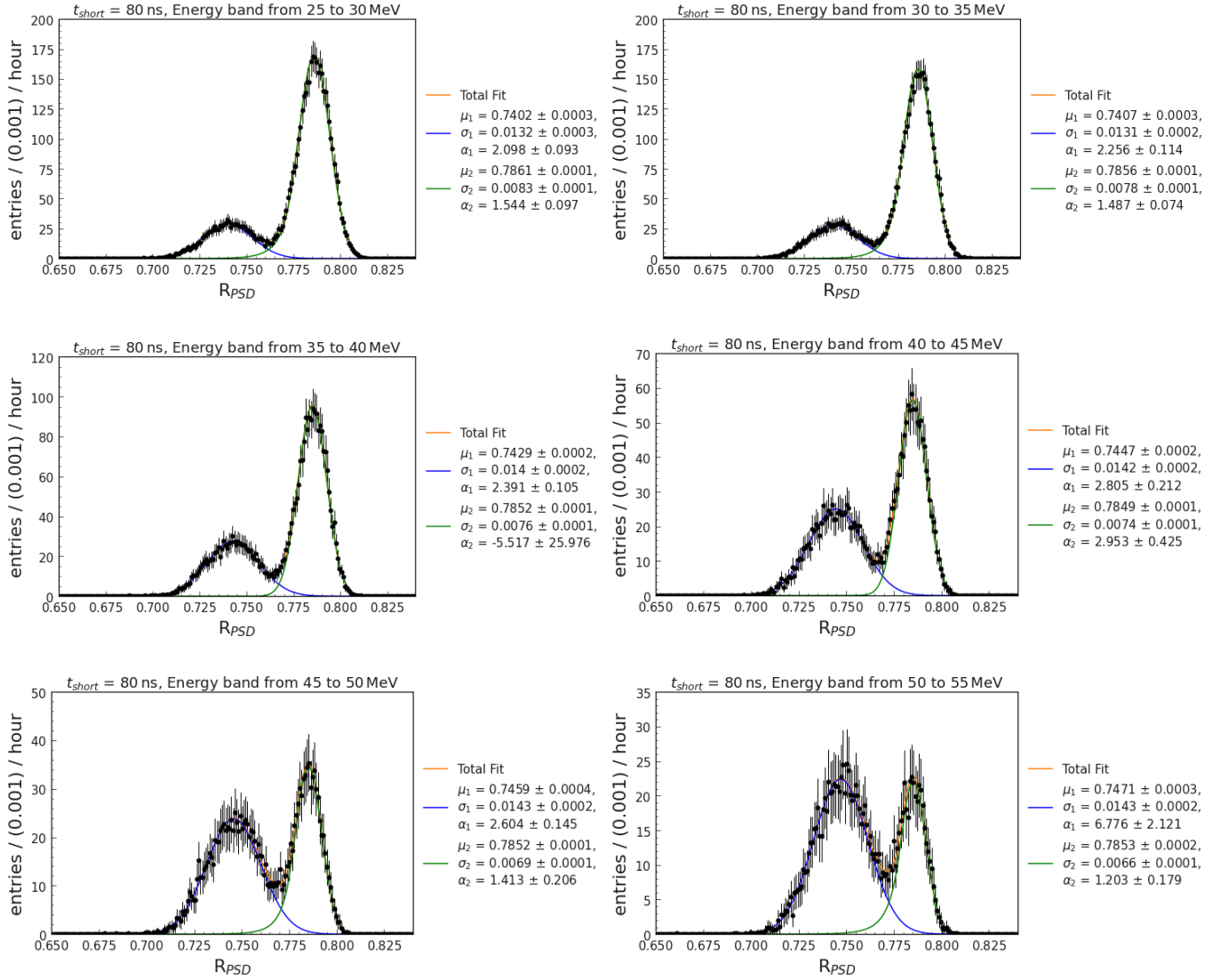


Figure B.11: Same as Figure B.3 but here with a short gate of $t_{short} = 80$ ns.

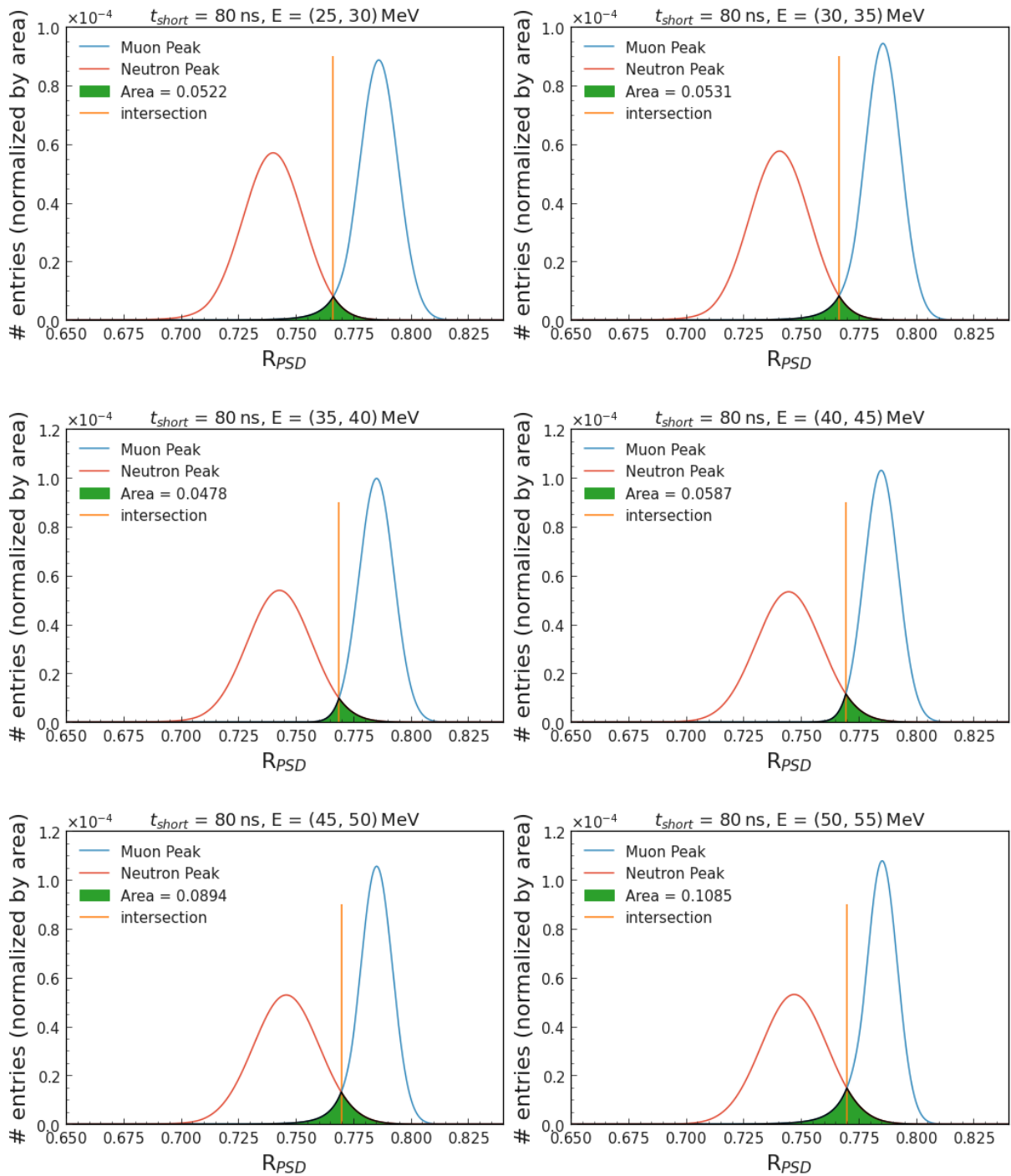


Figure B.12: Same as Figure B.4 but here with a short gate of $t_{short} = 80$ ns.

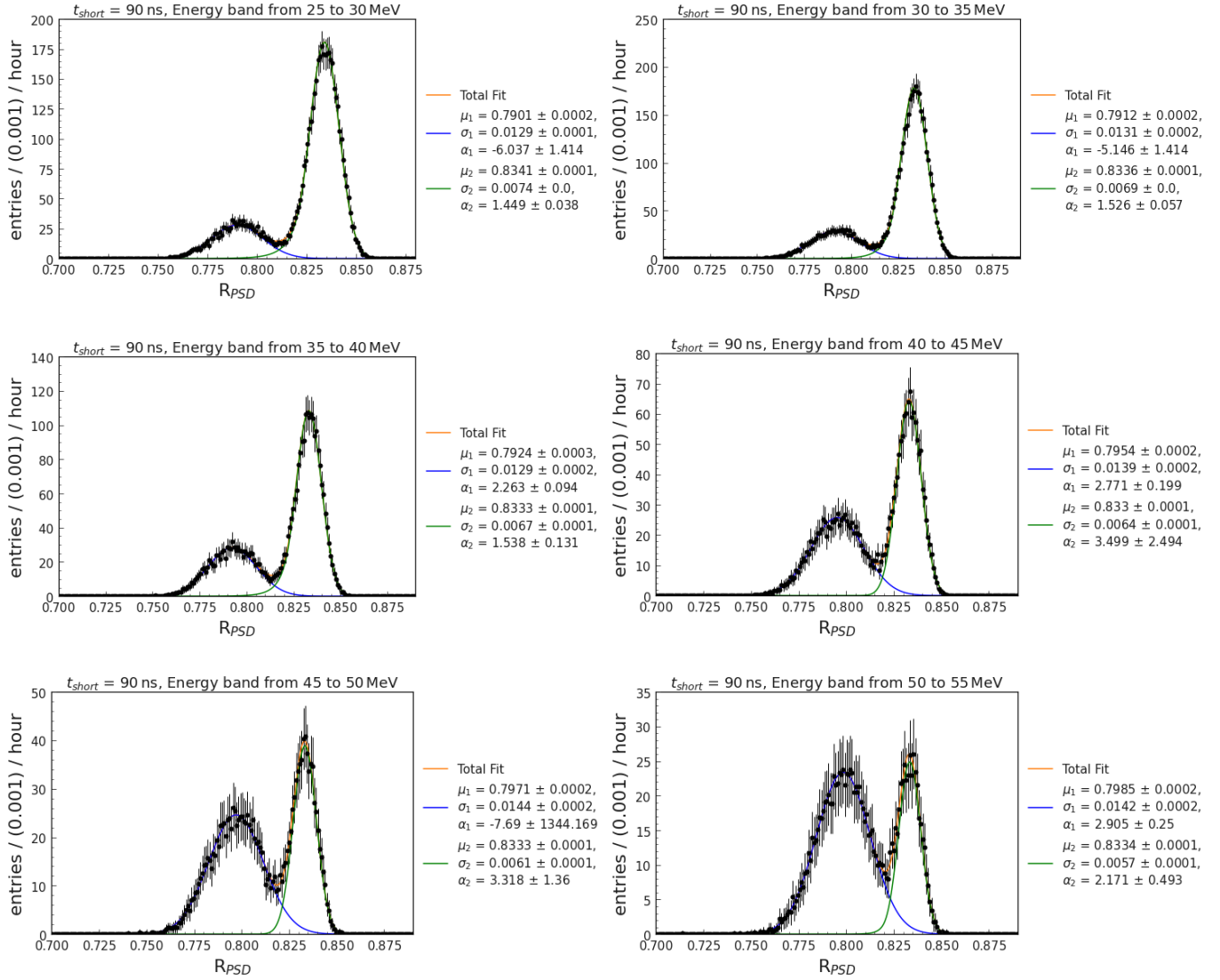


Figure B.13: Same as Figure B.3 but here with a short gate of $t_{short} = 90$ ns.

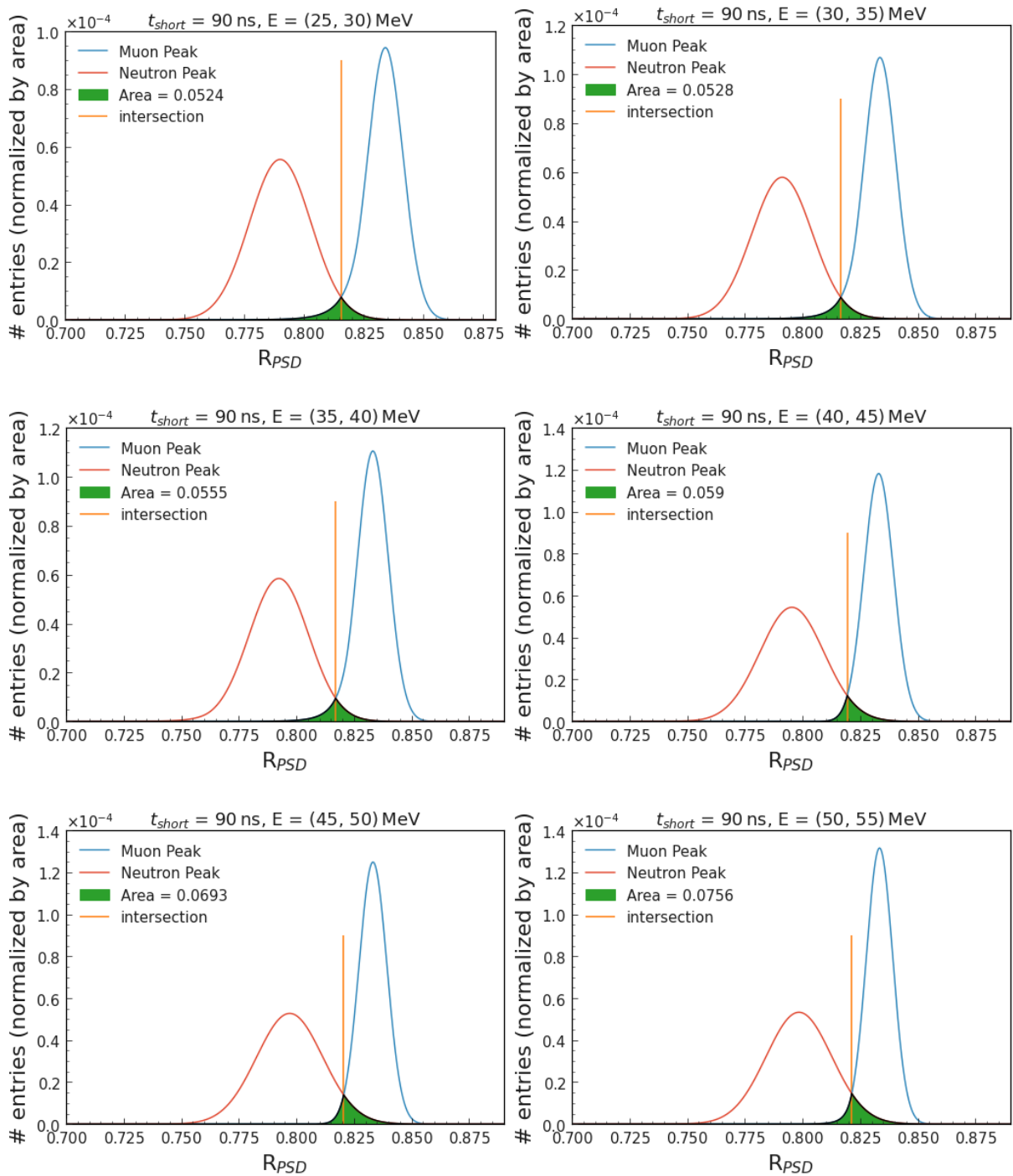


Figure B.14: Same as Figure B.4 but here with a short gate of $t_{short} = 90$ ns.

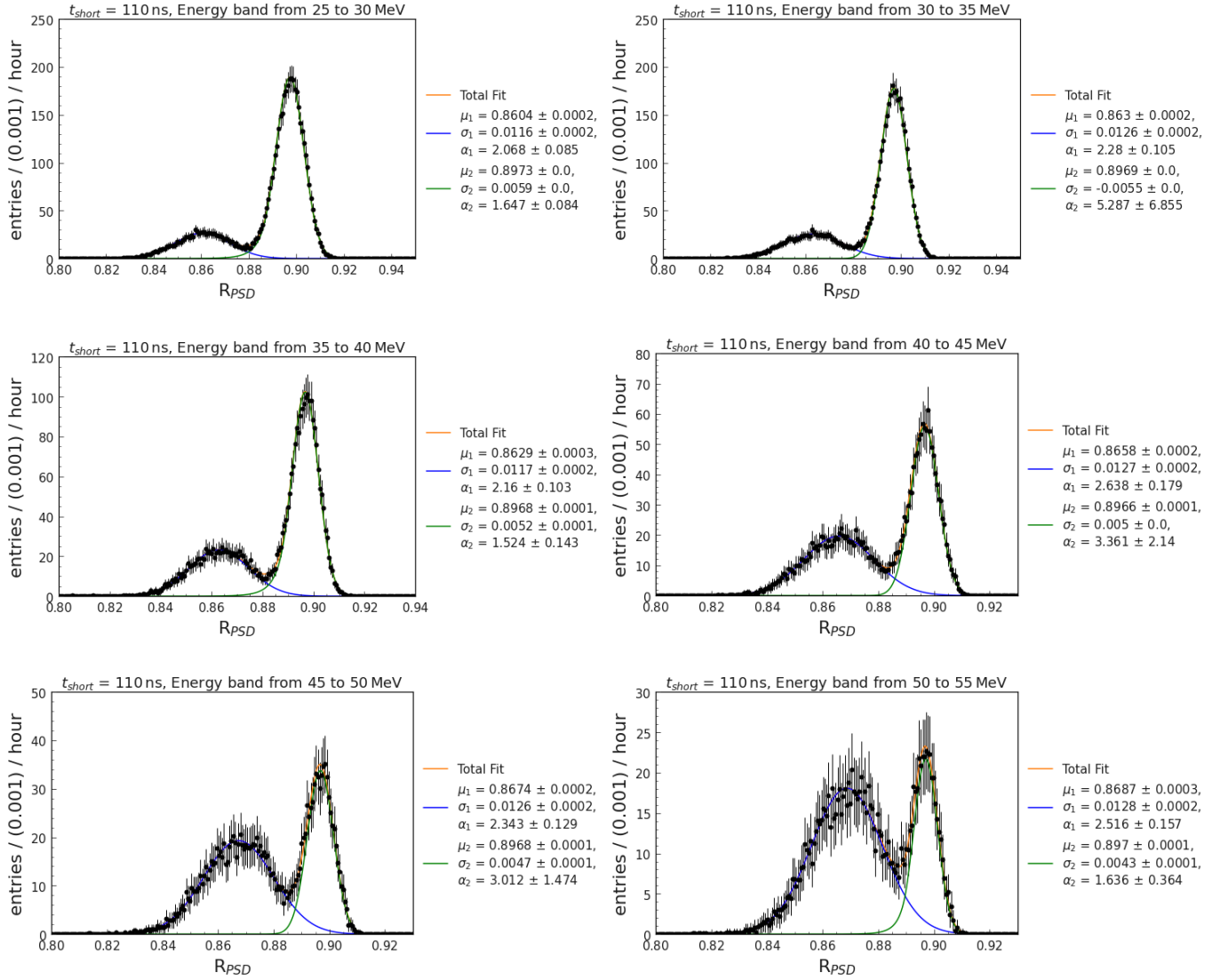


Figure B.15: Same as Figure B.3 but here with a short gate of $t_{short} = 110$ ns.

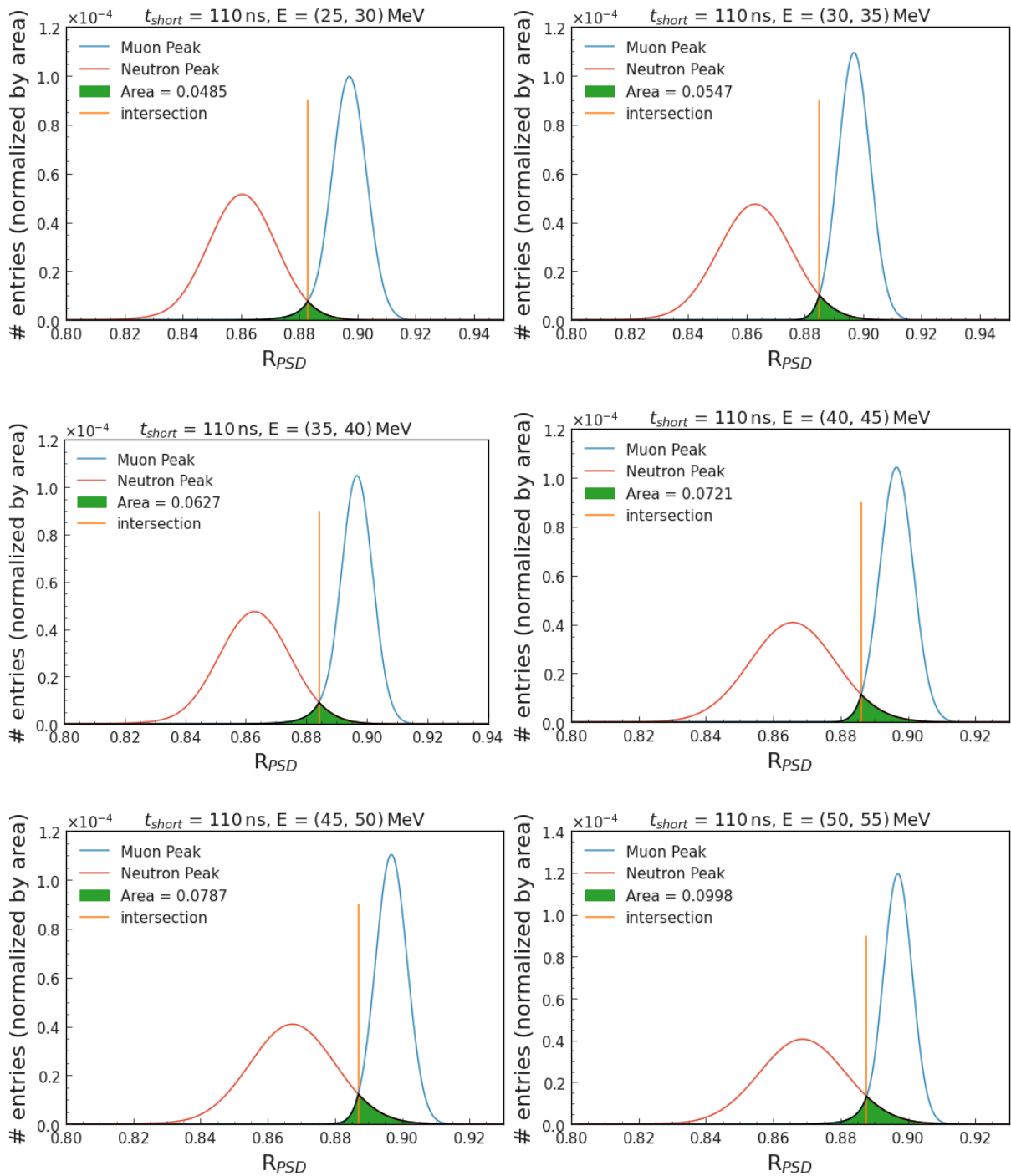


Figure B.16: Same as Figure B.4 but here with a short gate of $t_{short} = 110$ ns.

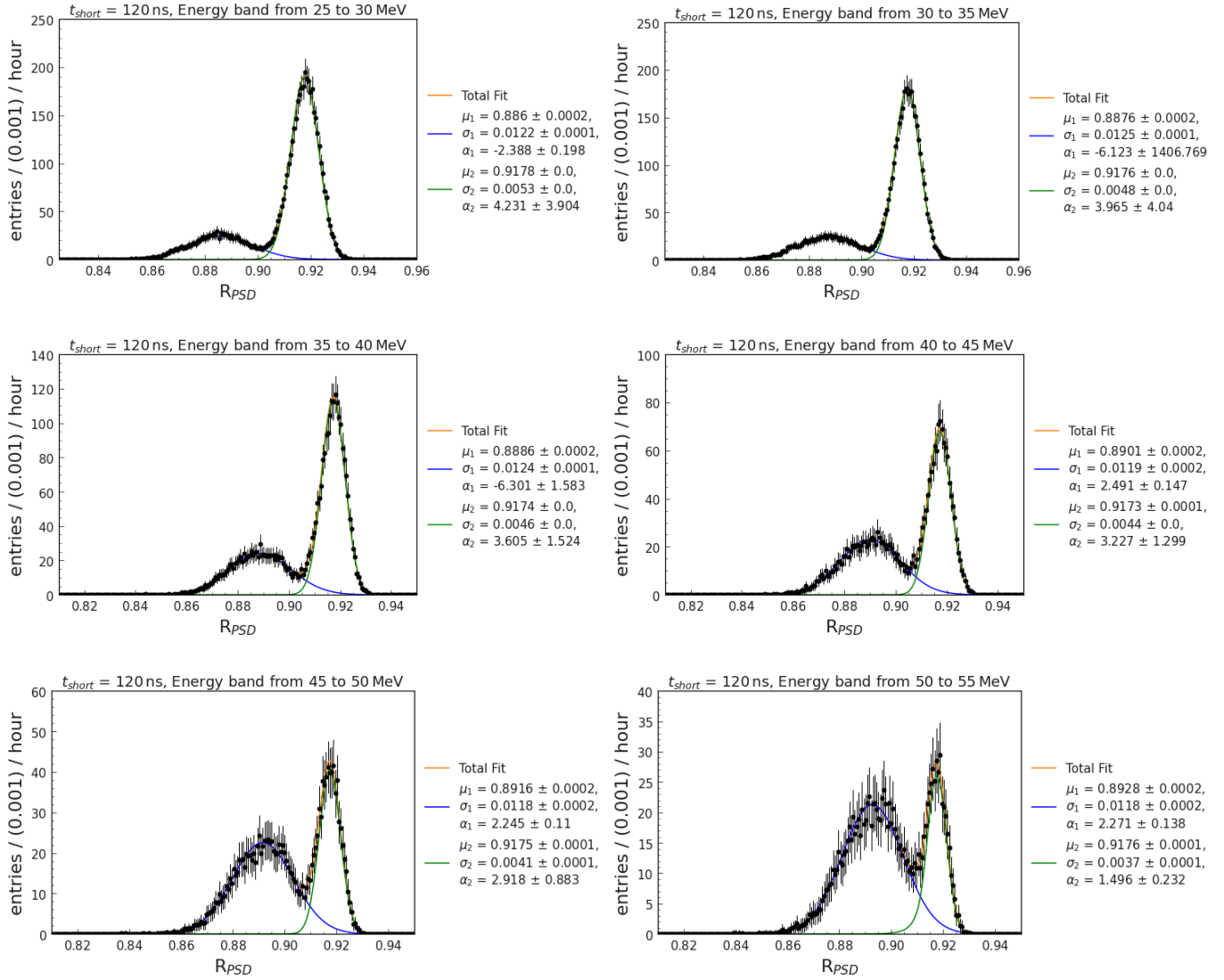


Figure B.17: Same as Figure B.3 but here with a short gate of $t_{short} = 120$ ns.

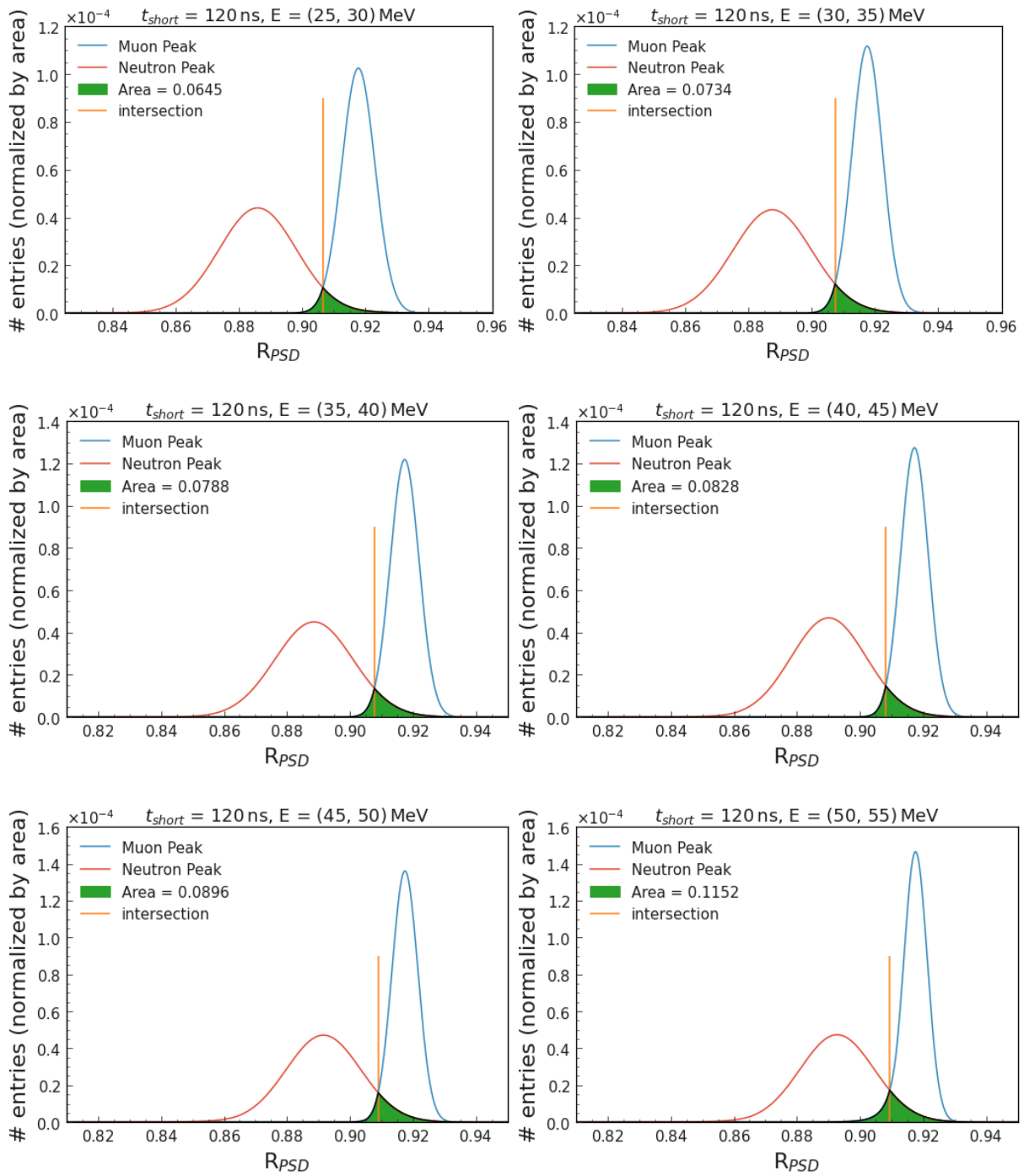


Figure B.18: Same as Figure B.4 but here with a short gate of $t_{short} = 120$ ns.

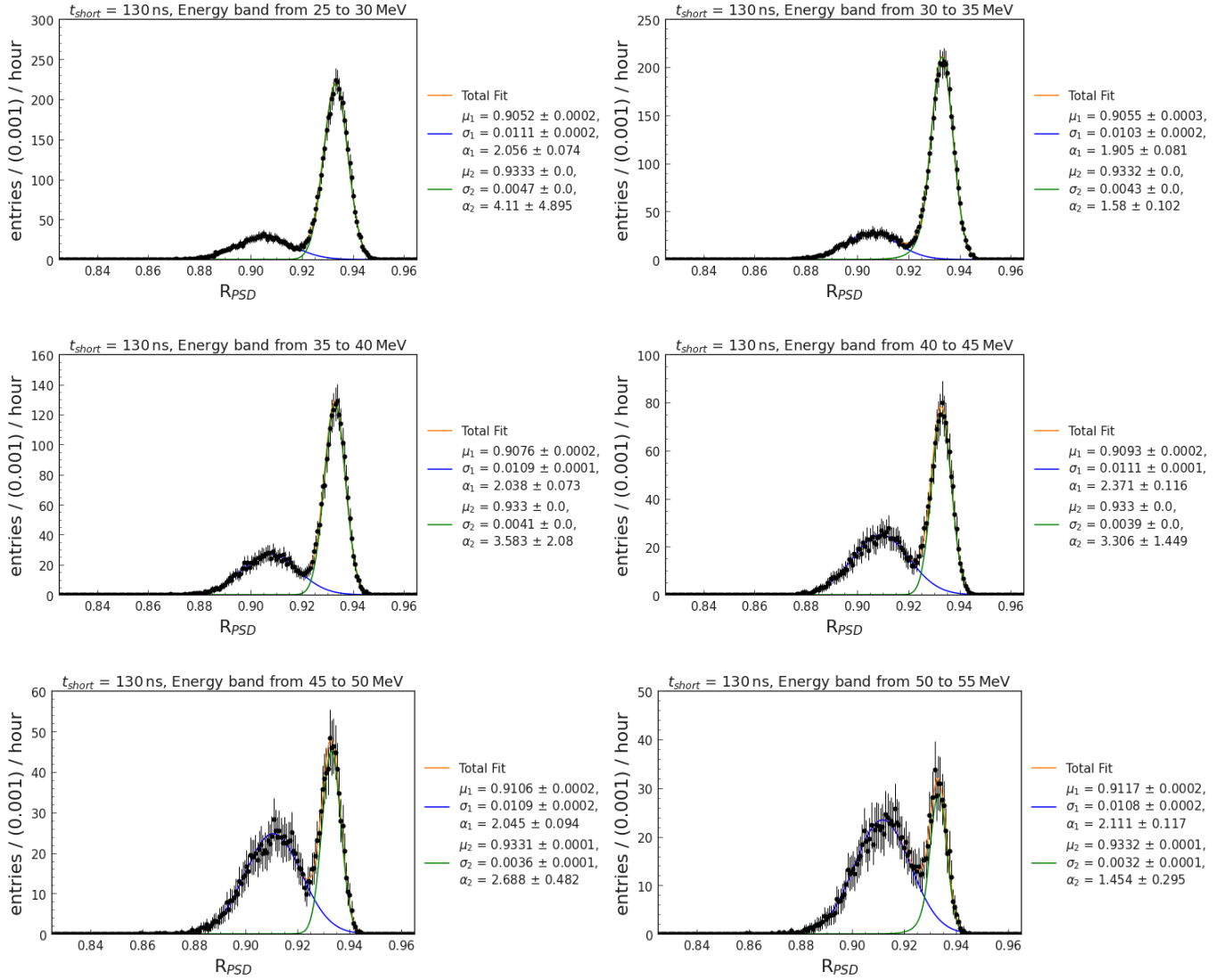


Figure B.19: Same as Figure B.3 but here with a short gate of $t_{short} = 130$ ns.

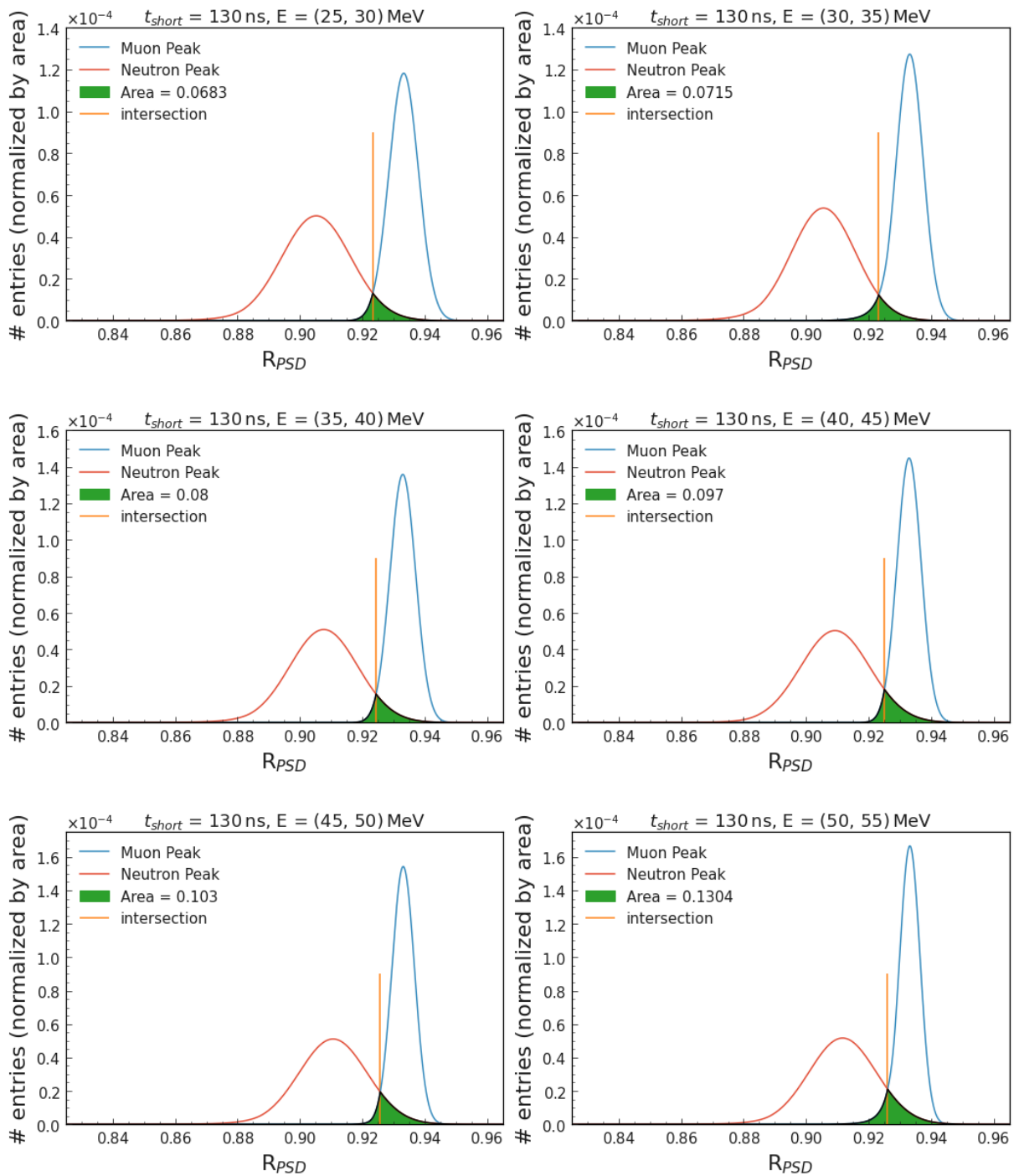


Figure B.20: Same as Figure B.4 but here with a short gate of $t_{short} = 130$ ns.

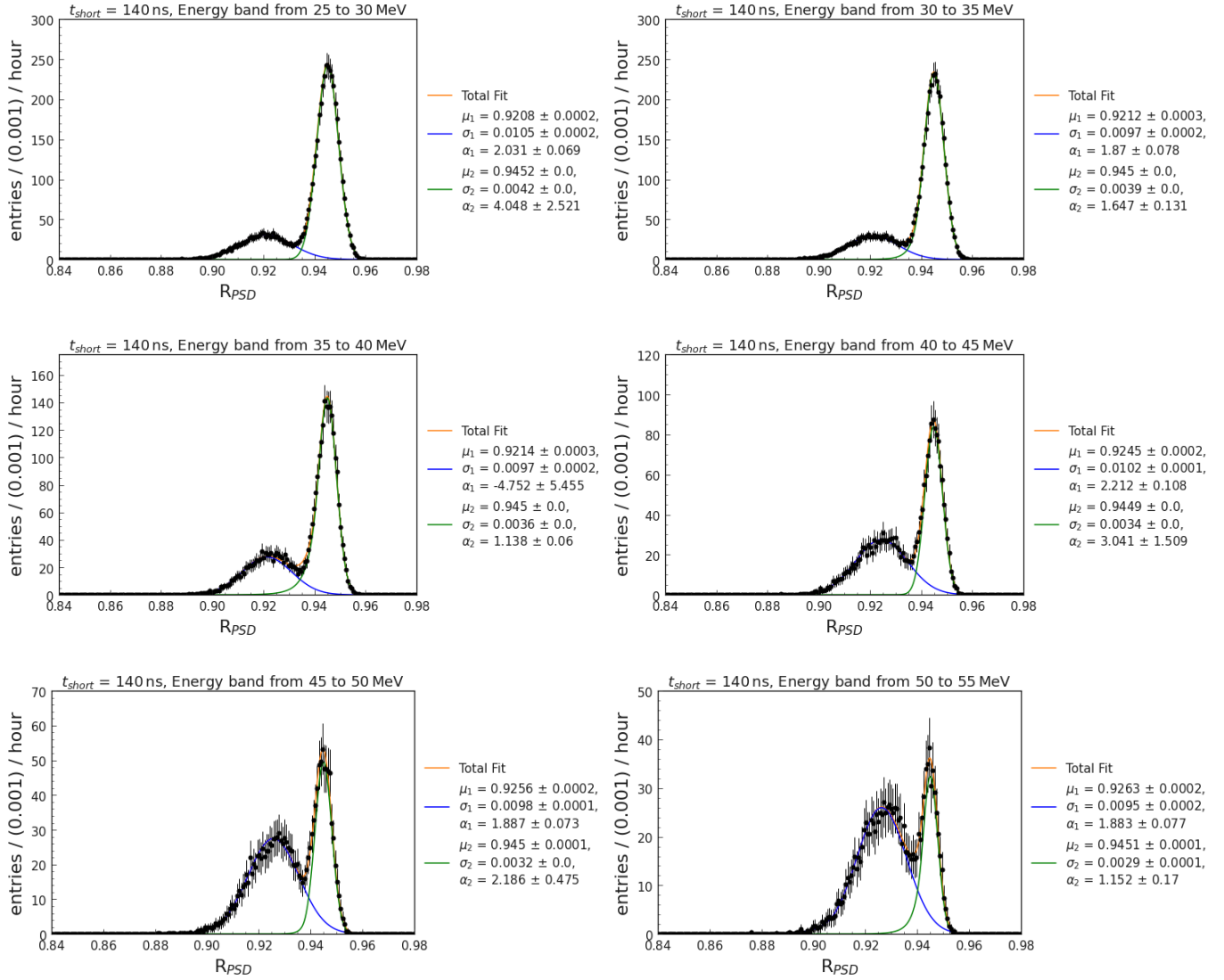


Figure B.21: Same as Figure B.3 but here with a short gate of $t_{short} = 140$ ns.

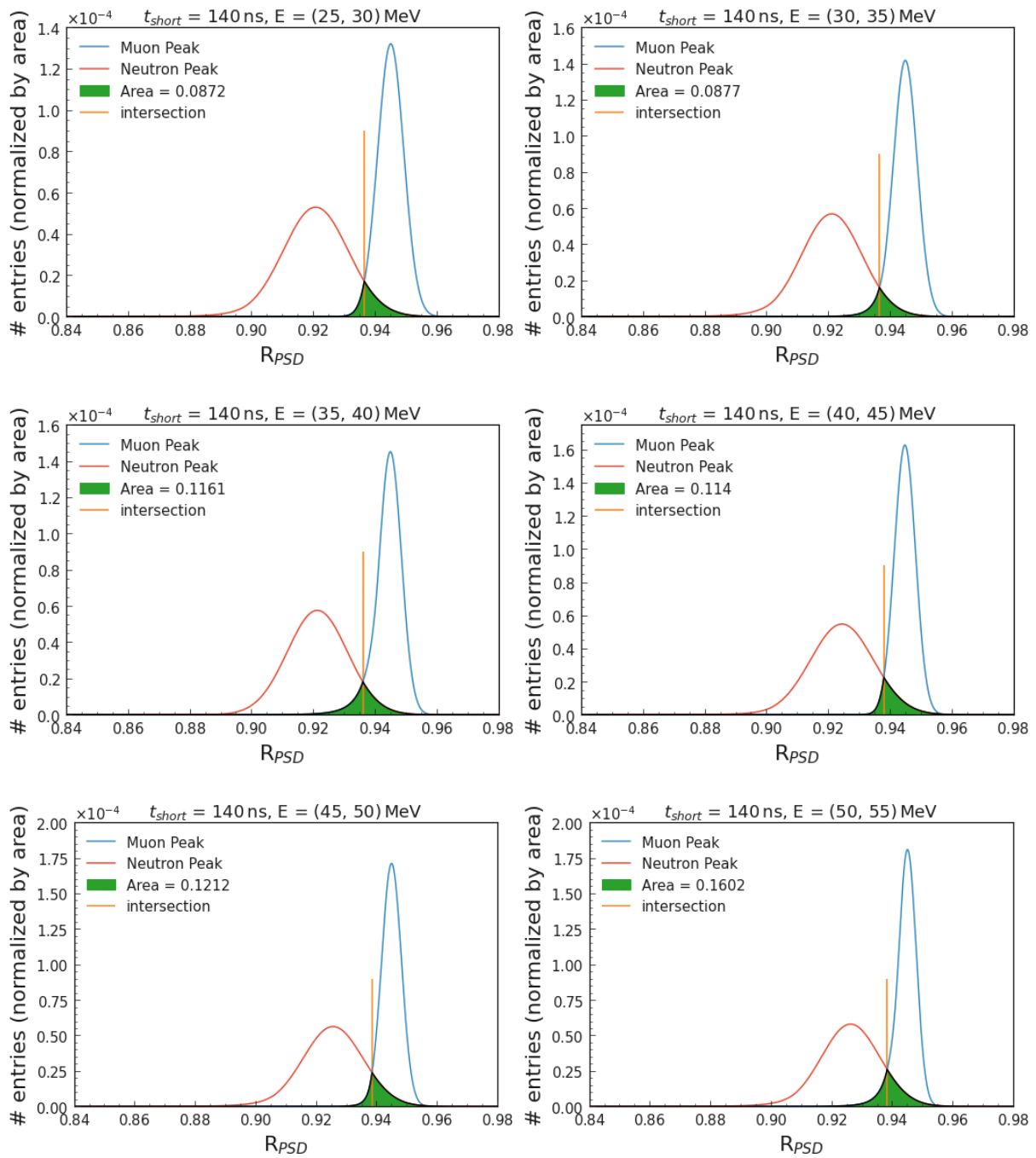


Figure B.22: Same as Figure B.4 but here with a short gate of $t_{short} = 140$ ns.

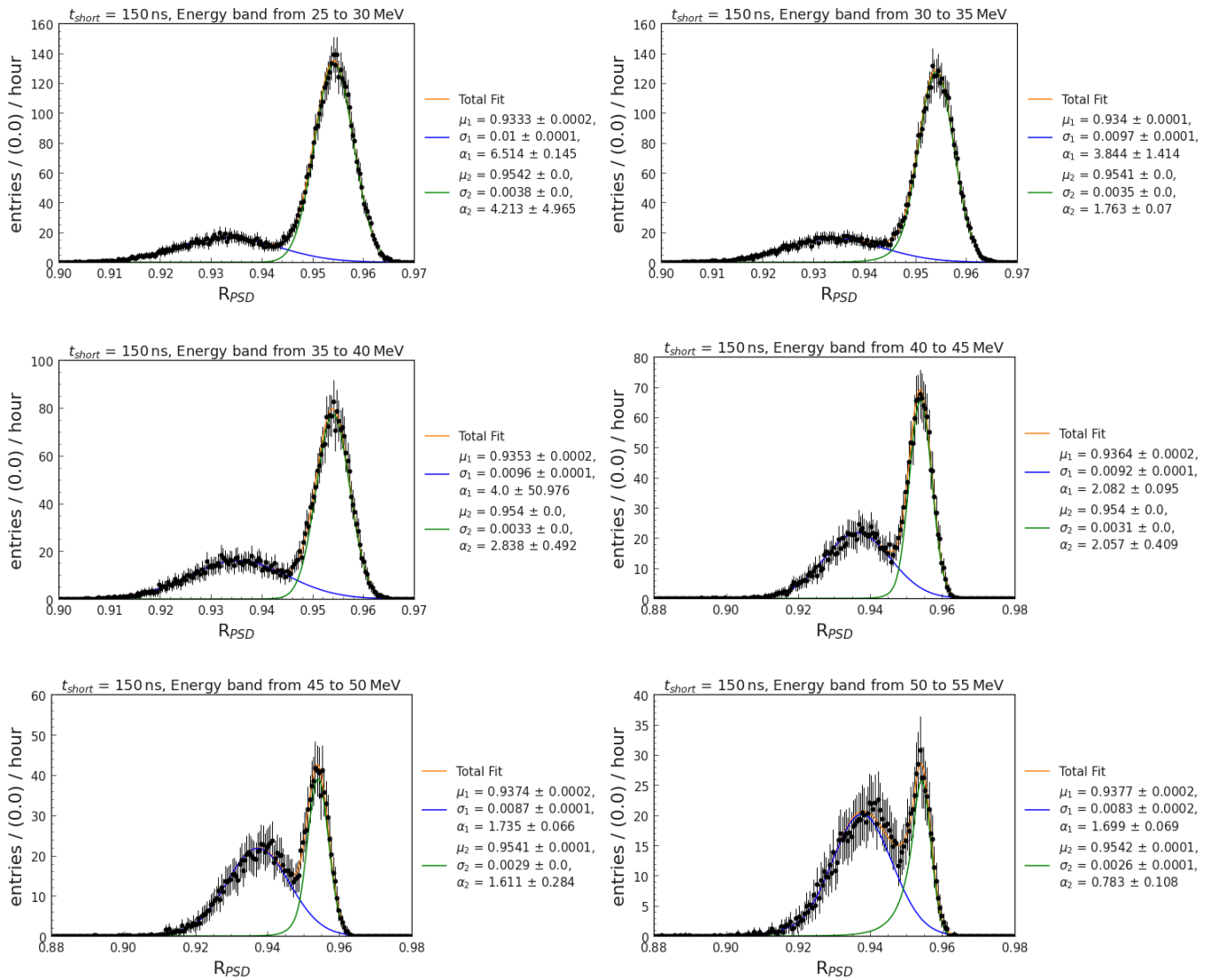


Figure B.23: Same as Figure B.3 but here with a short gate of $t_{short} = 150$ ns.

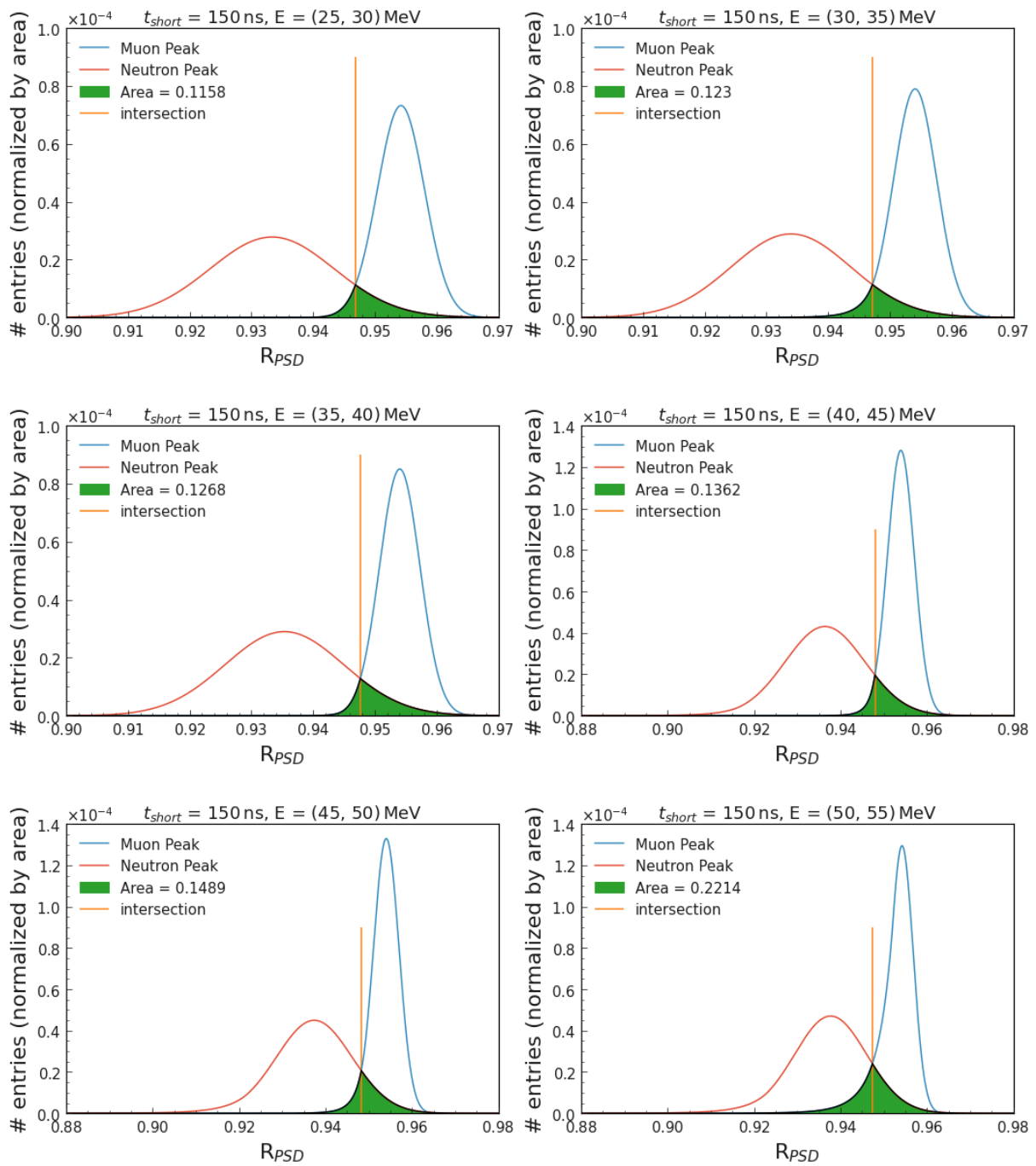


Figure B.24: Same as Figure B.4 but here with a short gate of $t_{short} = 150$ ns.

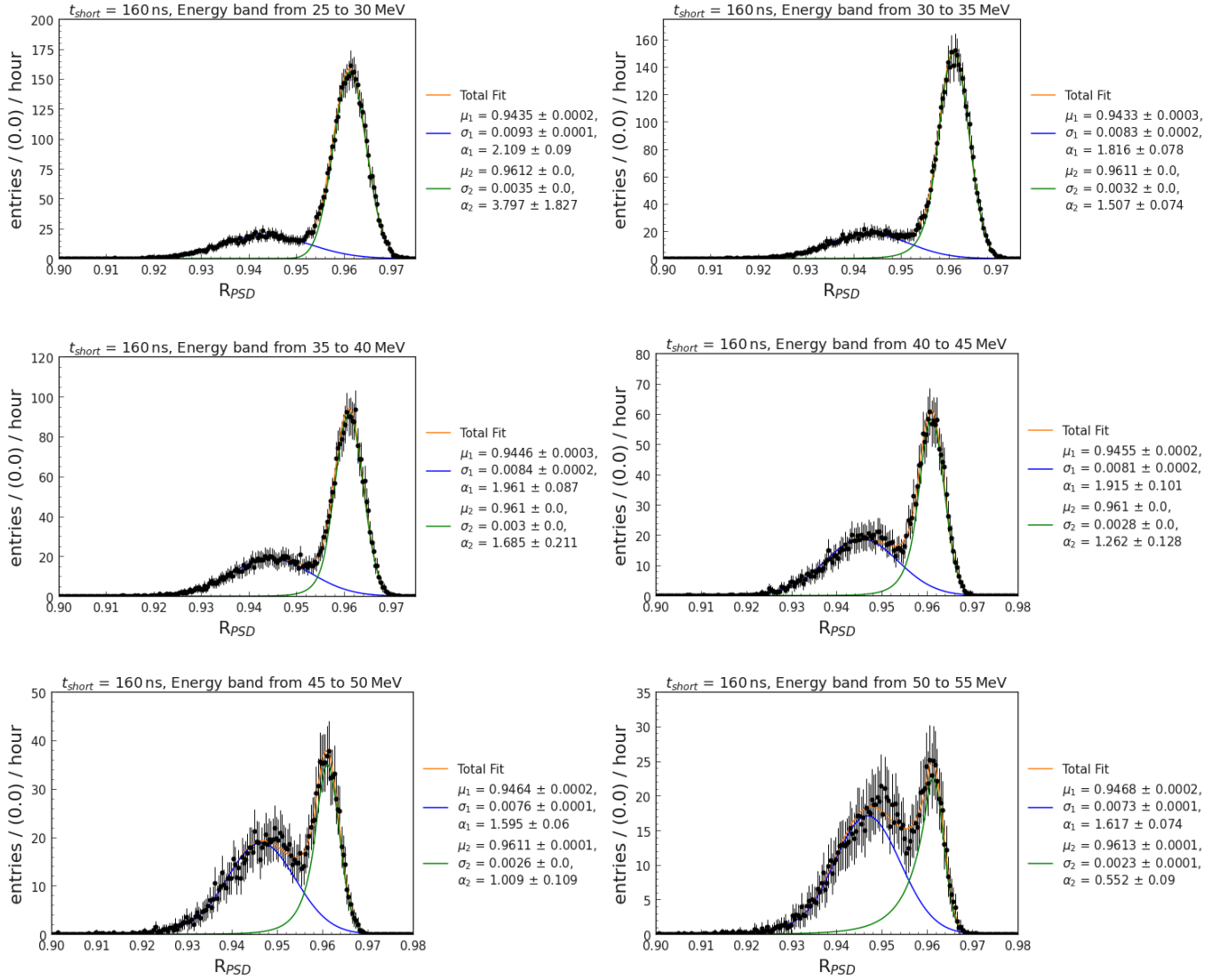


Figure B.25: Same as Figure B.3 but here with a short gate of $t_{short} = 160$ ns.

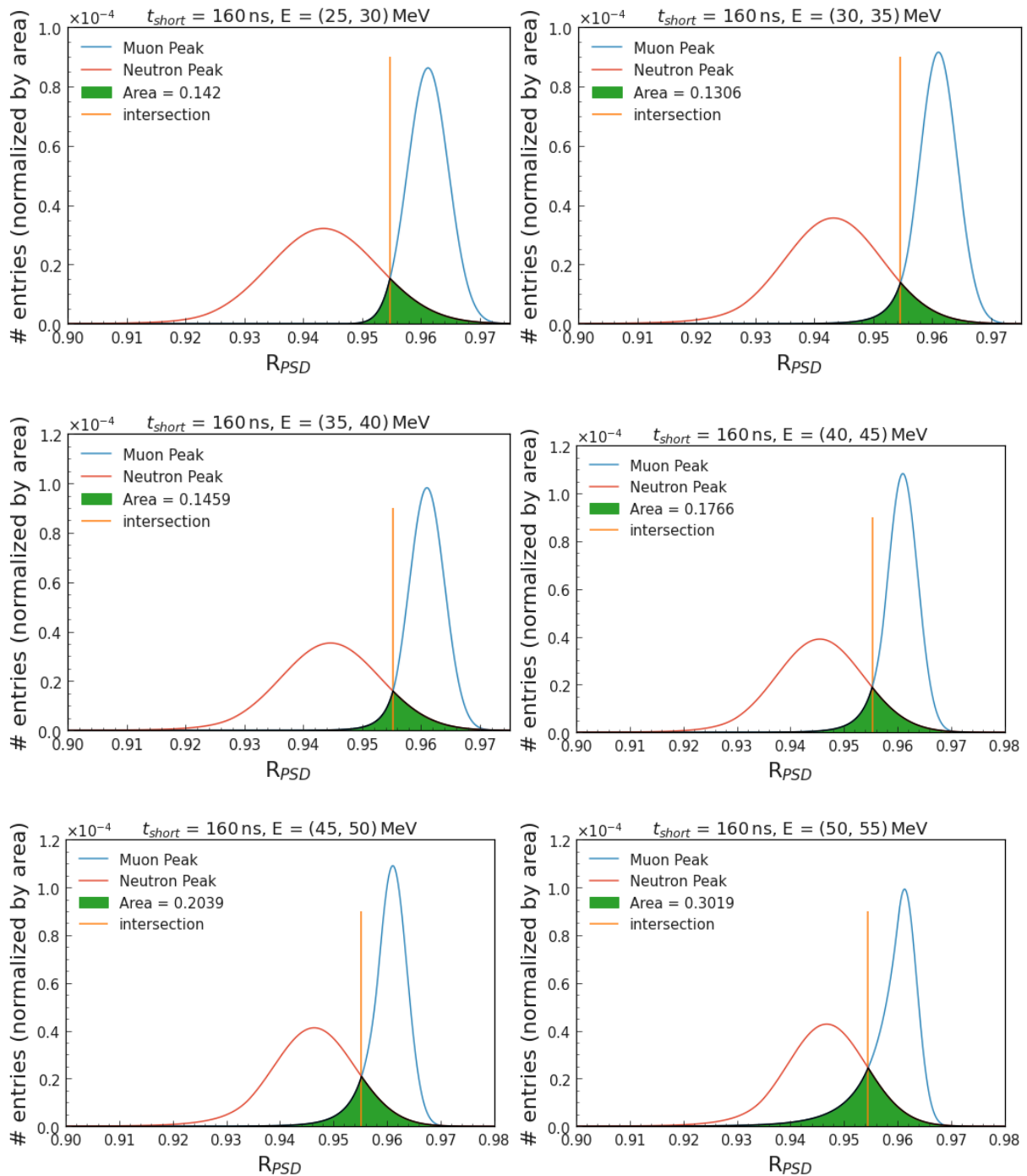


Figure B.26: Same as Figure B.4 but here with a short gate of $t_{short} = 160$ ns.

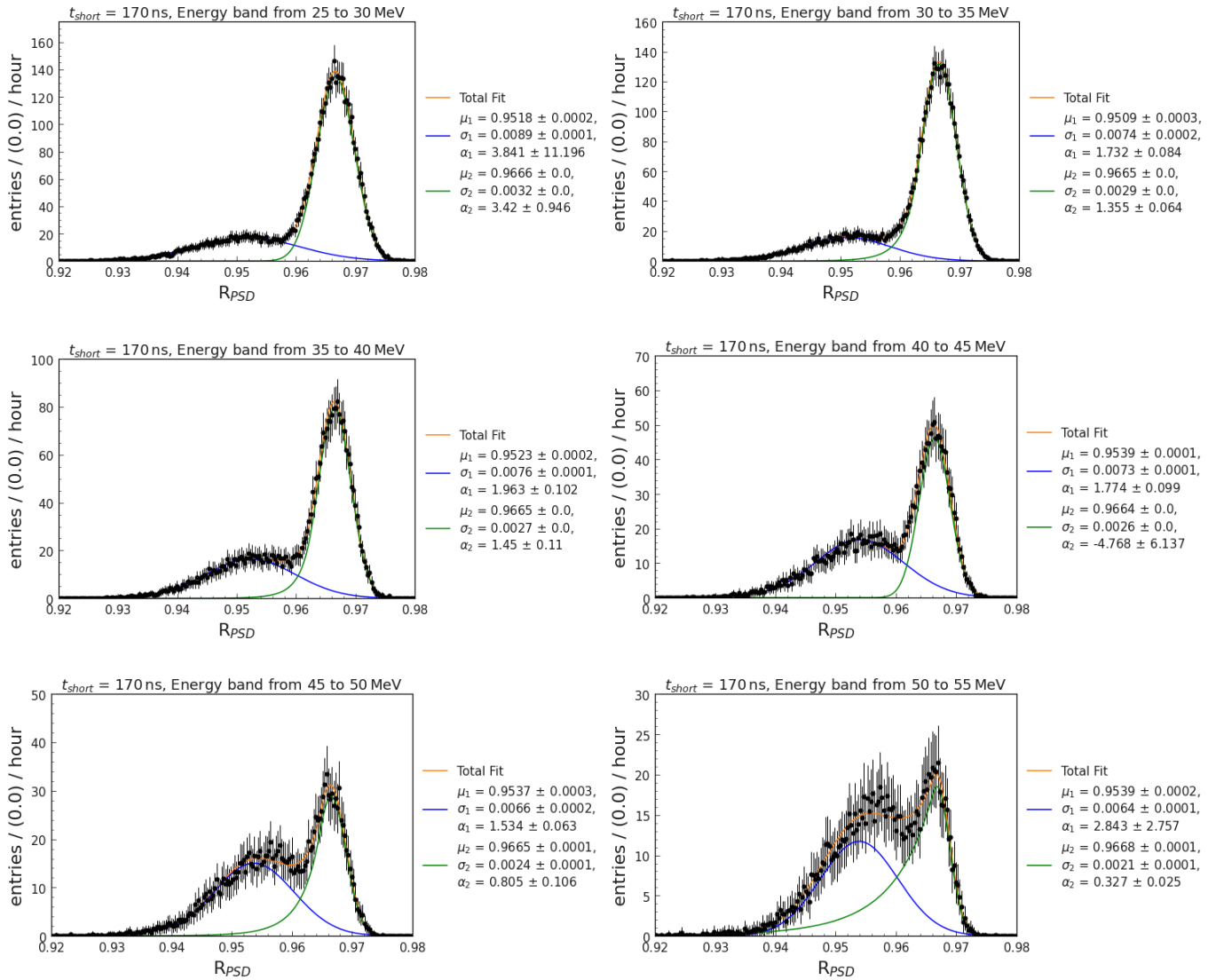


Figure B.27: Same as Figure B.3 but here with a short gate of $t_{short} = 170$ ns.

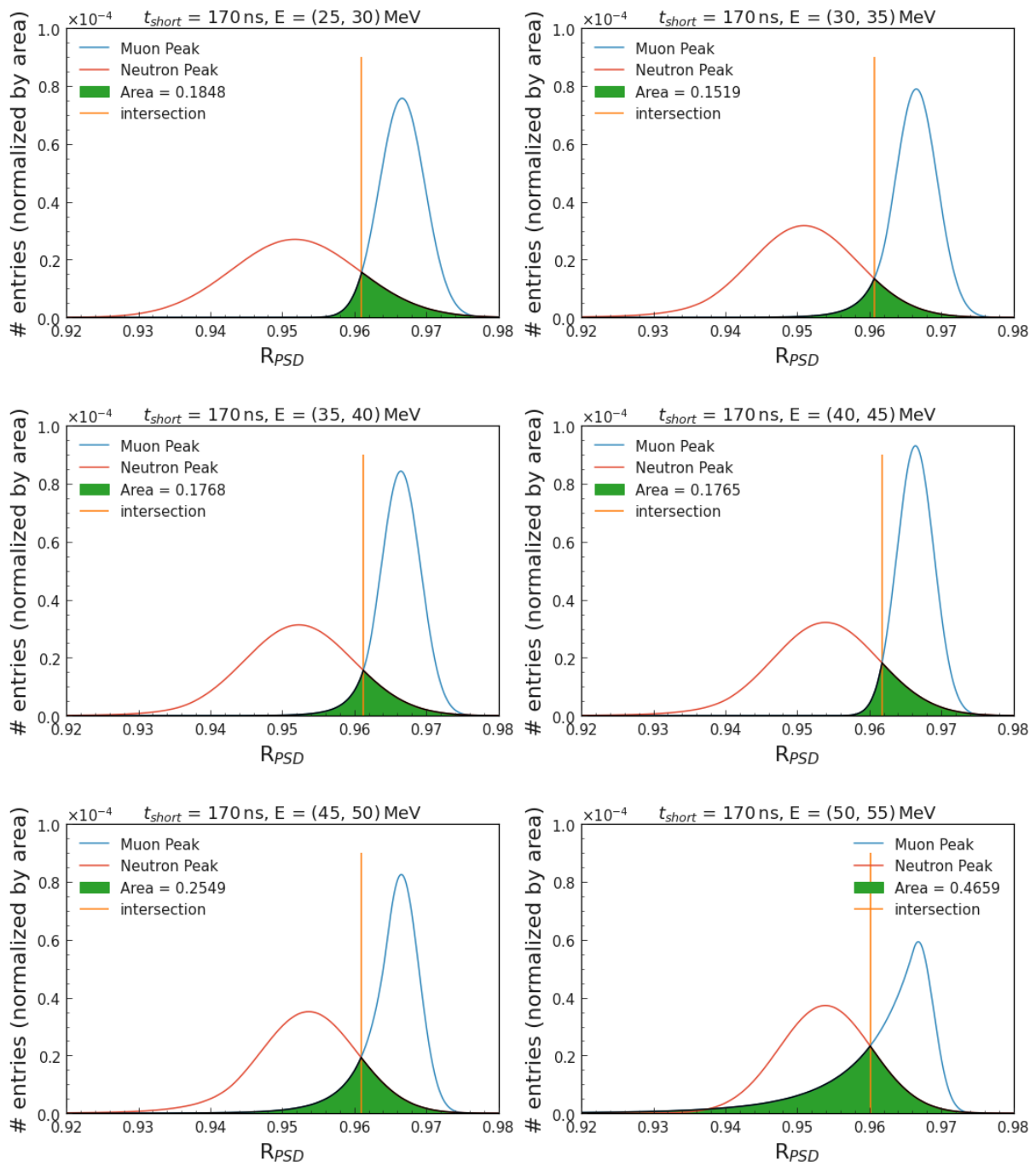


Figure B.28: Same as Figure B.4 but here with a short gate of $t_{short} = 170$ ns.

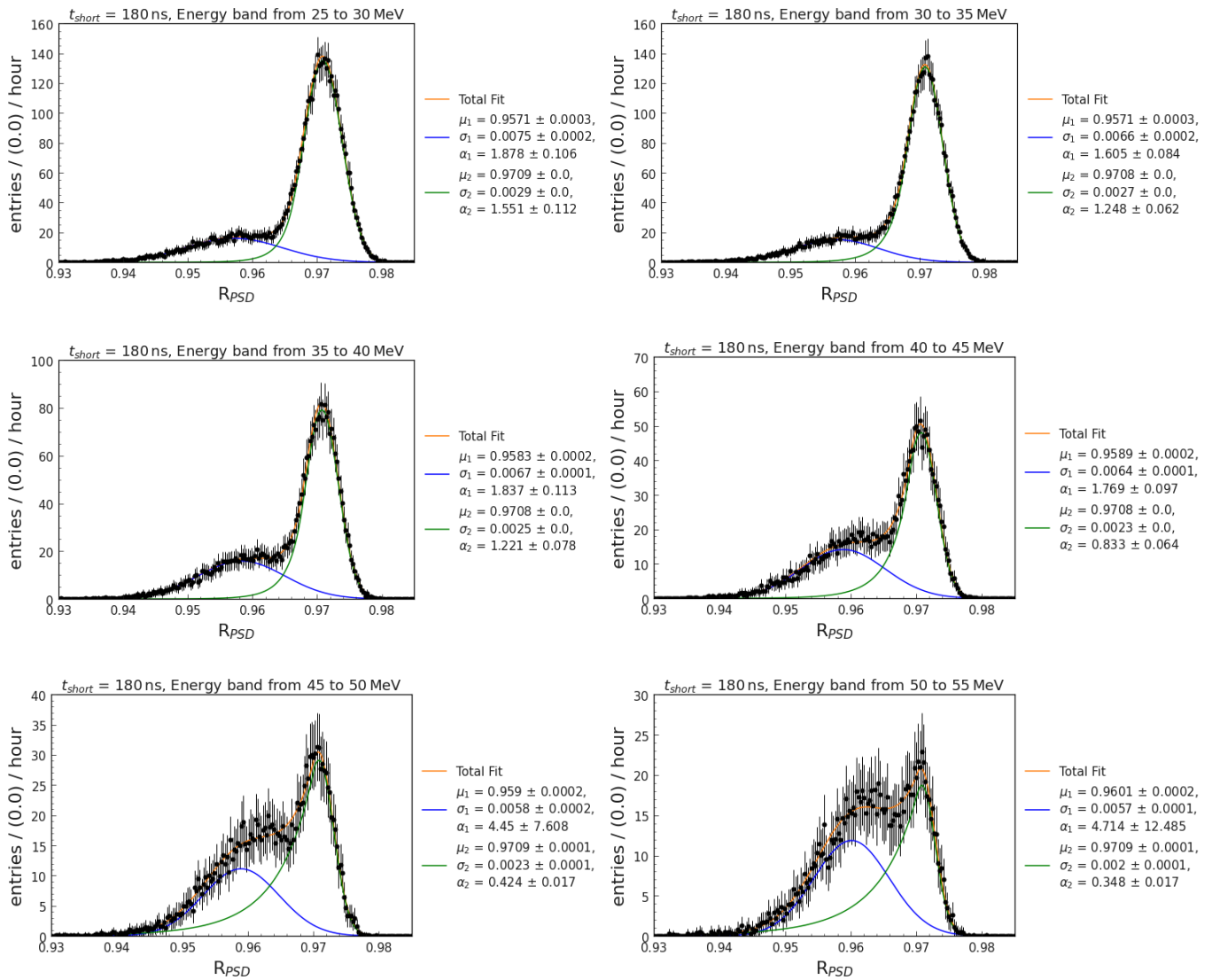


Figure B.29: Same as Figure B.3 but here with a short gate of $t_{short} = 180$ ns.

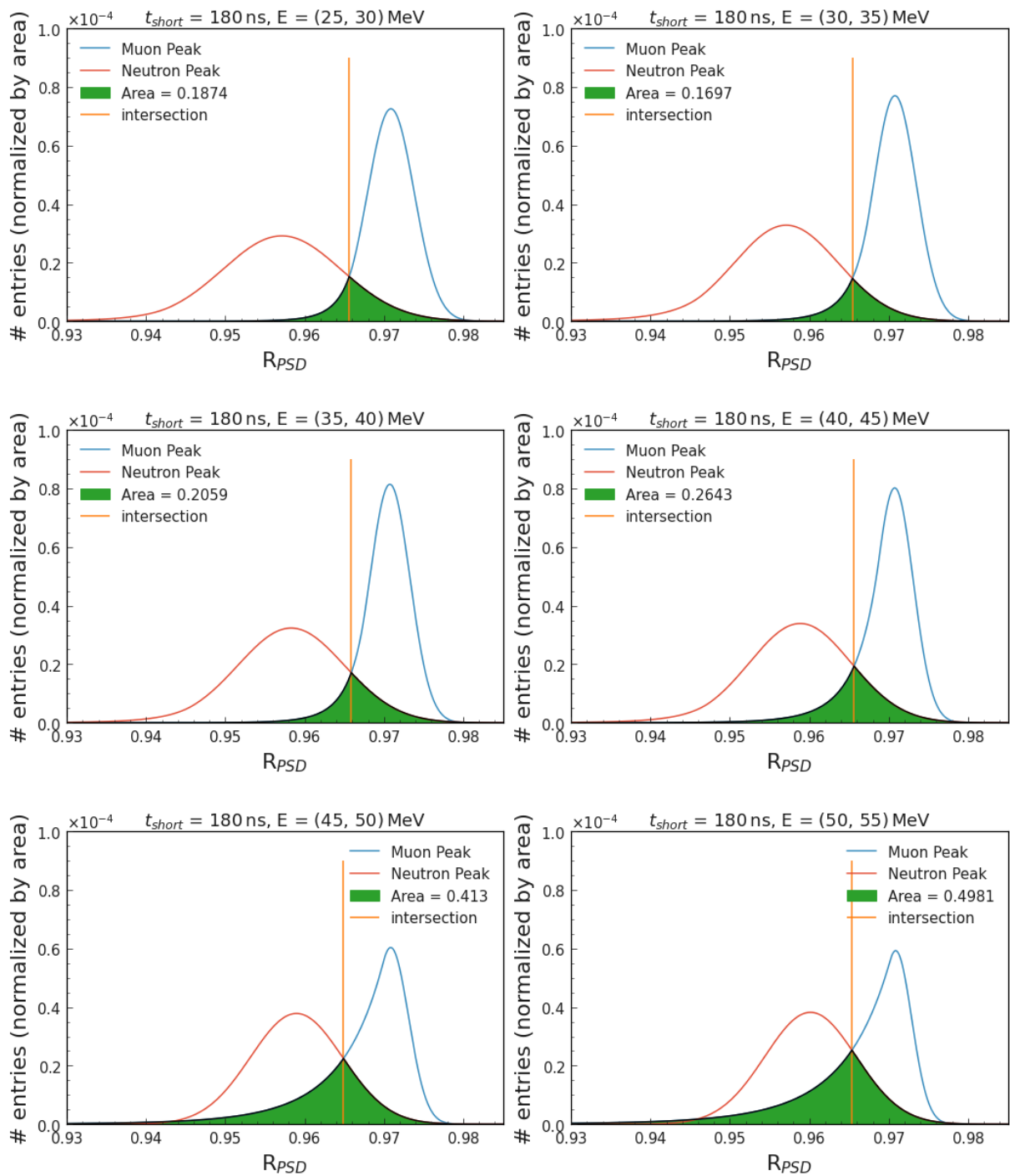


Figure B.30: Same as Figure B.4 but here with a short gate of $t_{short} = 180$ ns.

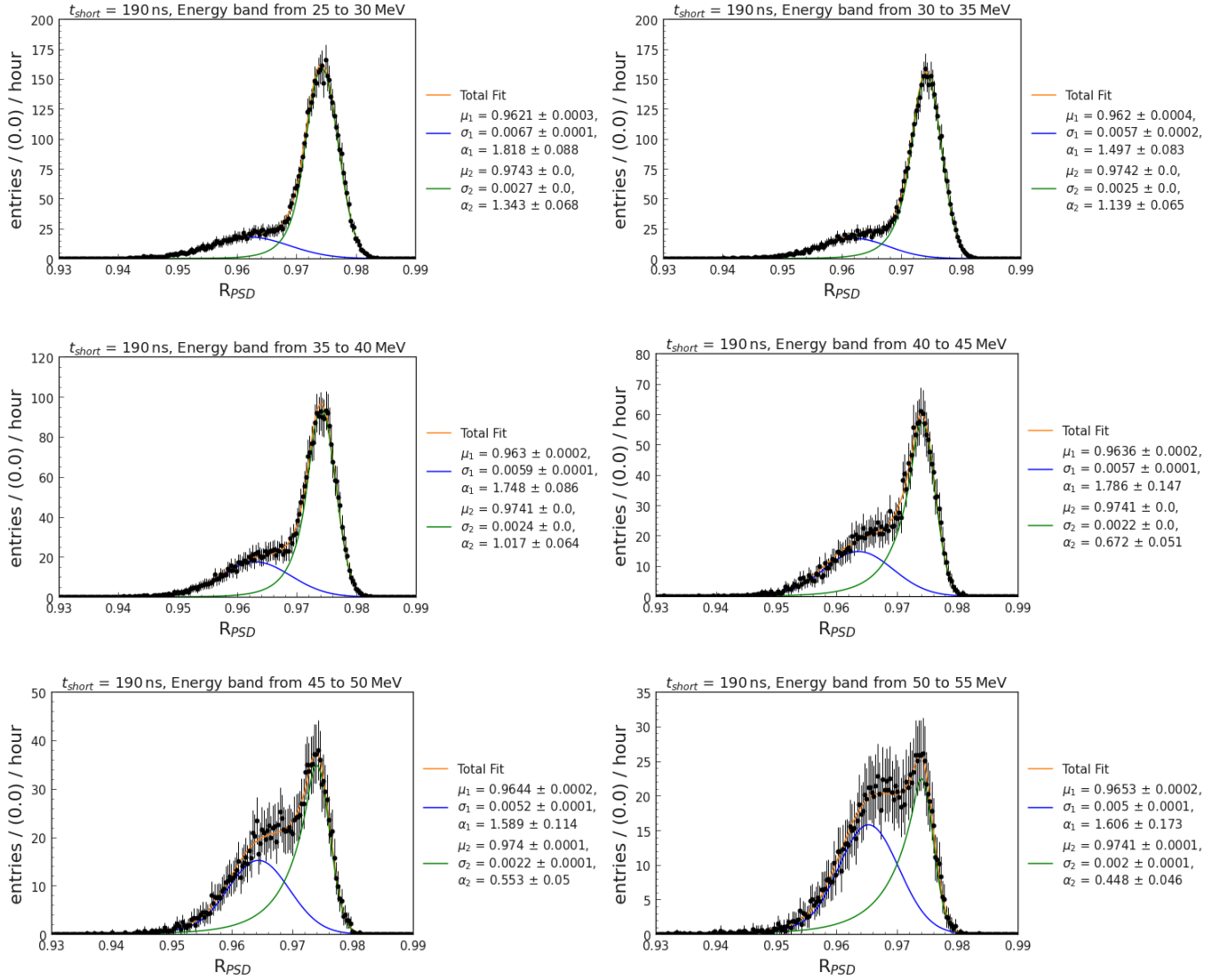


Figure B.31: Same as Figure B.3 but here with a short gate of $t_{short} = 190$ ns.

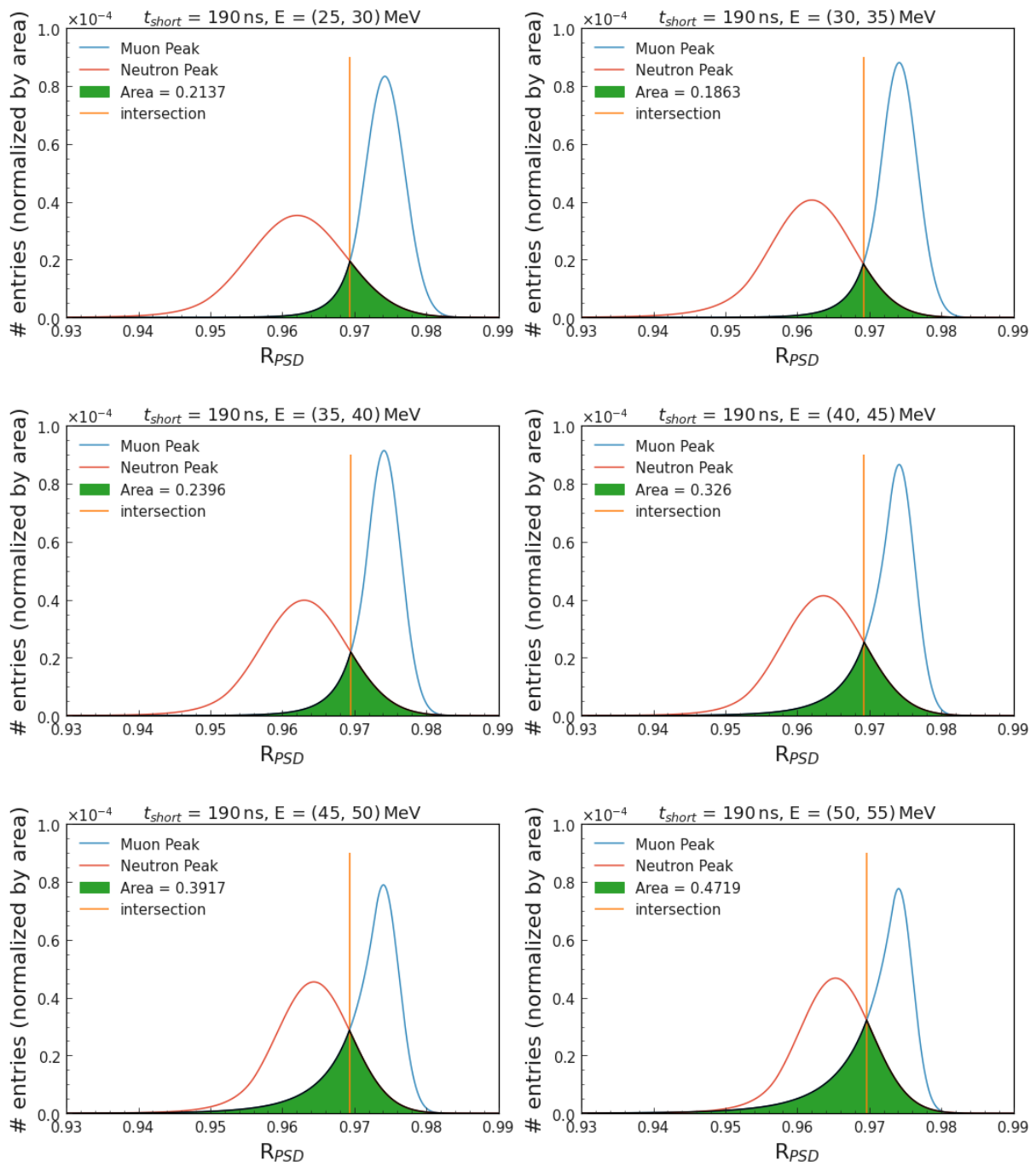


Figure B.32: Same as Figure B.4 but here with a short gate of $t_{short} = 190$ ns.

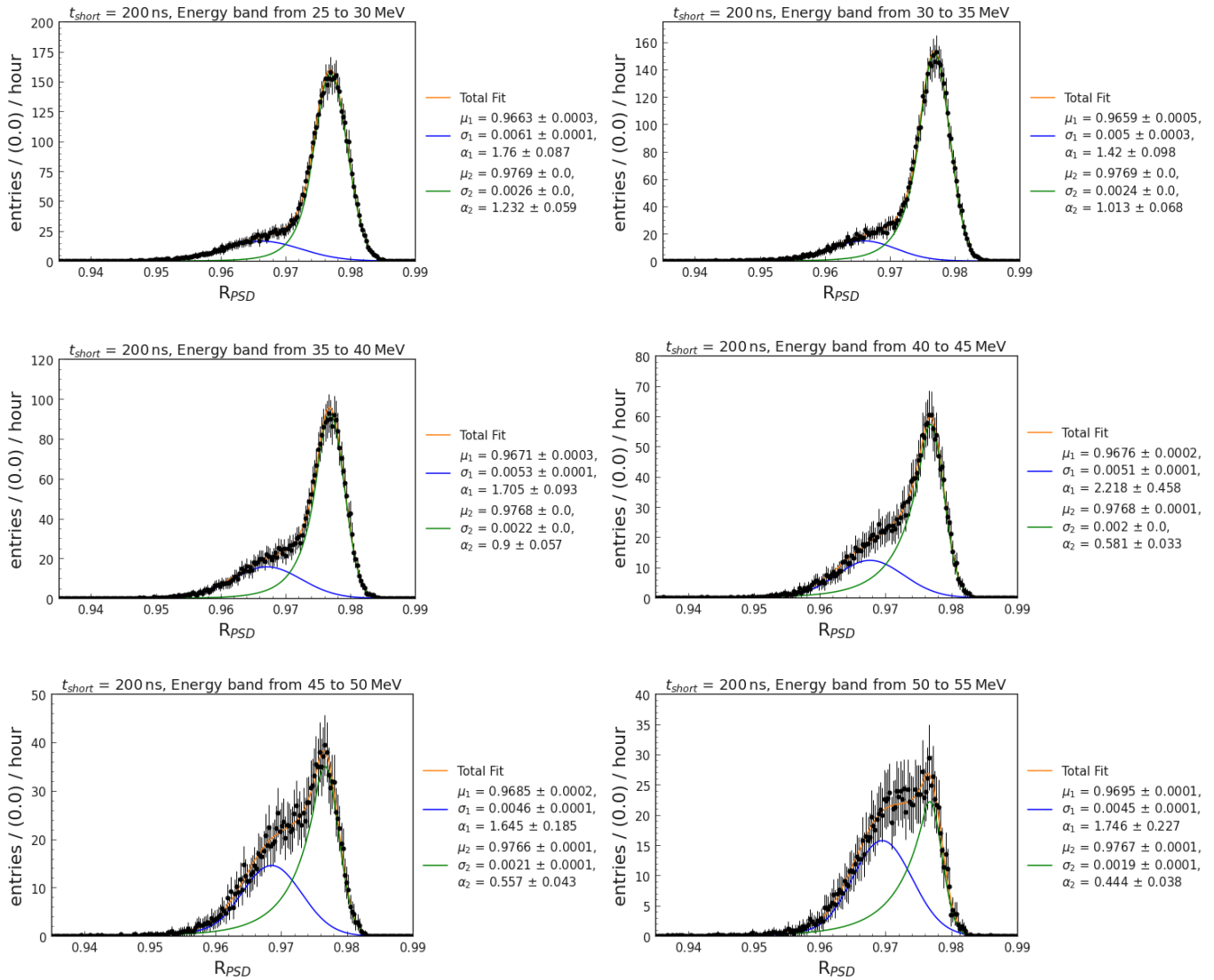


Figure B.33: Same as Figure B.3 but here with a short gate of $t_{short} = 200$ ns.

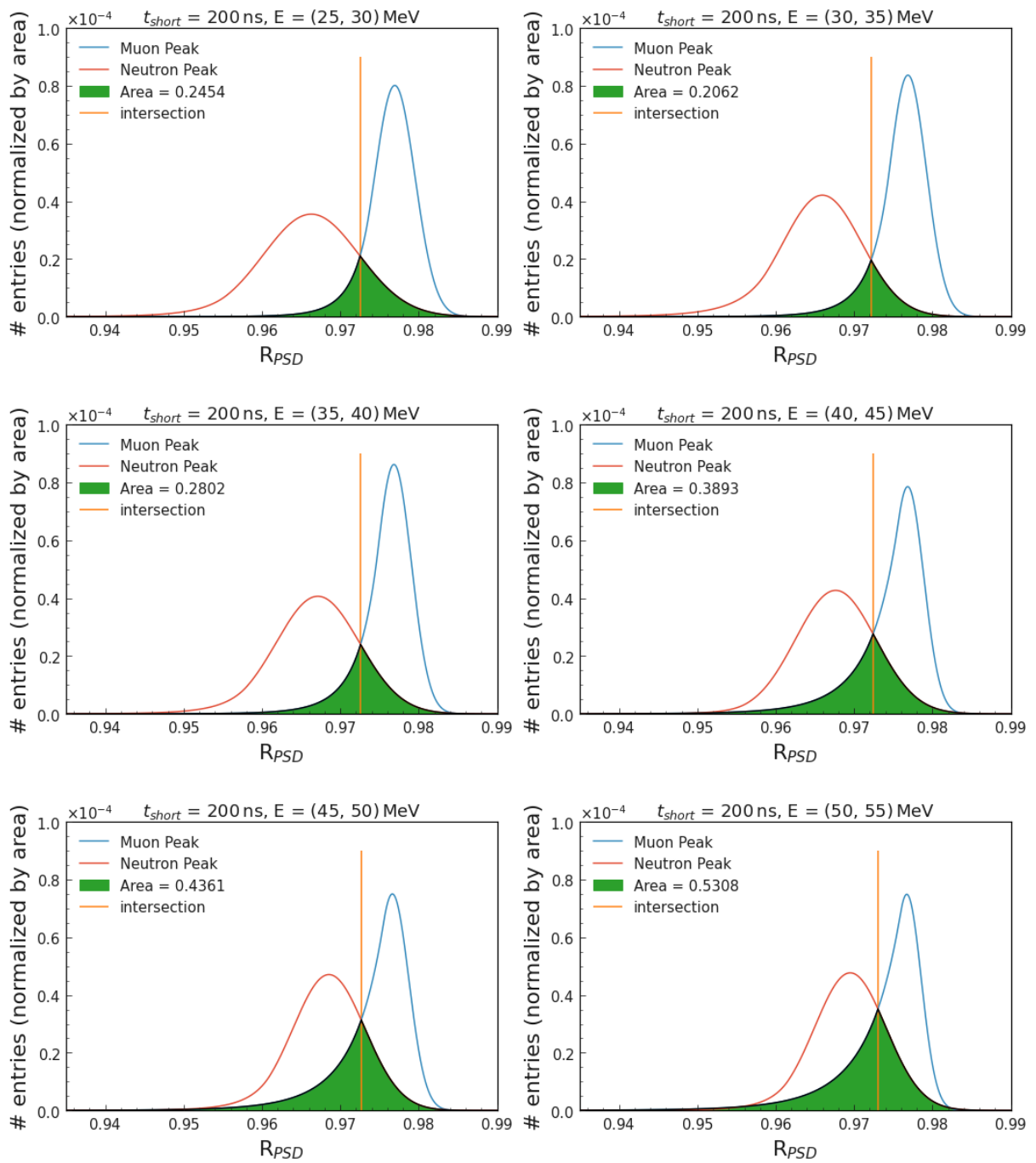


Figure B.34: Same as Figure B.4 but here with a short gate of $t_{short} = 200$ ns.

Bibliography

- [1] Savino Longo et al. CsI(Tl) pulse shape discrimination with the Belle II electromagnetic calorimeter as a novel method to improve particle identification at electron–positron colliders. *Nucl. Instrum. Meth. A*, 982:164562, Dec 2020. doi: 10.1016/j.nima.2020.164562.
- [2] Savino Longo. Measurements of the Radiation Hardness of CsI(Tl) Scintillation Crystals and Comparison Studies with Pure CsI for the Belle II Electromagnetic Calorimeter. Master’s thesis, University of Victoria, September 2015. <https://dspace.library.uvic.ca:8443/handle/1828/6707>.
- [3] N. Atanov et al. The Mu2e undoped CsI crystal calorimeter. *JINST*, 13(02):C02037, 2018. doi: 10.1088/1748-0221/13/02/C02037.
- [4] Y. Sugiyama et al. Pulse shape discrimination of photons and neutrons in the energy range of 0.1 – 2 GeV with the KOTO un-doped CsI calorimeter. *Nucl. Instrum. Meth. A*, 987:164825, 2021. doi: 10.1016/j.nima.2020.164825.
- [5] Mark Thomson. *Modern particle physics*. Cambridge University Press, New York, 2013. ISBN 978-1-107-03426-6.
- [6] Wikipedia: Standard model. https://en.wikipedia.org/wiki/Standard_Model. Accessed: 2021-09-01.
- [7] B. Abi et al. Measurement of the Positive Muon Anomalous Magnetic Moment to 0.46 ppm. *Phys. Rev. Lett.*, 126:141801, April 2021. doi: 10.1103/PhysRevLett.126.141801. URL <https://link.aps.org/doi/10.1103/PhysRevLett.126.141801>.

- [8] Taku Yamanaka. The J-PARC KOTO experiment. *PTEP*, 2012:02B006, 2012. doi: 10.1093/ptep/pts057.
- [9] Melissa A. Hutcheson. Status on the Search for $K_L^0 \rightarrow \pi^0 \nu \bar{\nu}$ with the KOTO Experiment. [*arXiv:1910.07585 [hep-ex]*], October 2019.
- [10] Chieh Lin. Recent Result on the Measurement of $K_L^0 \rightarrow \pi^0 \nu \bar{\nu}$ at the J-PARC KOTO Experiment. *JPS Conf. Proc.*, 33:011105, 2021. doi: 10.7566/JPSCP.33.011105.
- [11] K. Sato et al. CsI calorimeter for the J-PARC KOTO experiment. *Nucl. Instrum. Meth. A*, 982:164527, 2020. doi: 10.1016/j.nima.2020.164527.
- [12] T. Aoyama, N. Asmussen, M. Benayoun, J. Bijnens, T. Blum, M. Bruno, I. Caprini, C.M. Carloni Calame, M. Cè, G. Colangelo, and et al. The anomalous magnetic moment of the muon in the Standard Model. *Physics Reports*, 887:1–166, Dec 2020. ISSN 0370-1573. doi: 10.1016/j.physrep.2020.07.006. URL <http://dx.doi.org/10.1016/j.physrep.2020.07.006>.
- [13] Y. Maeda. Plots for $ee \rightarrow \pi^+\pi^-\gamma$ analysis with phase2 full data. Sep 2018. URL <https://docs.belle2.org/record/1124?ln=en>.
- [14] B. Aubert et al. Precise Measurement of the $e^+e^- \rightarrow \pi^+\pi^-(\gamma)$ Cross Section with the Initial State Radiation Method at BABAR. *Phys. Rev. Lett.*, 103:231801, Dec 2009. doi: 10.1103/PhysRevLett.103.231801. URL <https://link.aps.org/doi/10.1103/PhysRevLett.103.231801>.
- [15] J. P. Lees et al. Precise measurement of the $e^+e^- \rightarrow \pi^+\pi^-(\gamma)$ cross section with the initial-state radiation method at BABAR. *Phys. Rev. D*, 86:032013, Aug 2012. doi: 10.1103/PhysRevD.86.032013. URL <https://link.aps.org/doi/10.1103/PhysRevD.86.032013>.
- [16] T. Abe et al. Belle II Technical Design Report. [*arXiv:1011.0352 [physics.ins-det]*], November 2010.
- [17] P.A. Zyla et al. (Particle Data Group). Review of Particle Physics. *Progress of Theoretical and Experimental Physics*, 2020(8), August 2020. ISSN 2050-3911. doi:

- 10.1093/ptep/ptaa104. URL <https://doi.org/10.1093/ptep/ptaa104.083C01>.
- [18] William R. Leo. *Techniques for Nuclear and Particle Physics Experiments: A How to Approach*. 1987. ISBN 978-3-540-57280-0.
- [19] Nuclear power: Interactions of neutrons with matter. <https://www.nuclear-power.com/nuclear-power/reactor-physics/atomic-nuclear-physics/fundamental-particles/neutron/interactions-neutrons-matter/>. Accessed: 2021-09-03.
- [20] Savino Longo. *First application of CsI(Tl) pulse shape discrimination at an e^+e^- collider to improve particle identification at the Belle II experiment*. PhD thesis, University of Victoria, Oct 2019. <https://dspace.library.uvic.ca//handle/1828/11301>.
- [21] Belle II Collaboration. Belle II Archives. <https://www.belle2.org/archives/>. Accessed: 2021-03-09.
- [22] I. Adachi, T.E. Browder, P. Križan, S. Tanaka, and Y. Ushiroda. Detectors for extreme luminosity: Belle II. *Nuclear Instruments and Methods in Physics Research Section A: Accelerators, Spectrometers, Detectors and Associated Equipment*, 907:46–59, 2018. ISSN 0168-9002. doi: <https://doi.org/10.1016/j.nima.2018.03.068>. URL <https://www.sciencedirect.com/science/article/pii/S0168900218304200>. *Advances in Instrumentation and Experimental Methods (Special Issue in Honour of Kai Siegbahn)*.
- [23] E Kou, P Urquijo, W Altmannshofer, F Beaujean, G Bell, M Beneke, I I Bigi, F Bishara, M Blanke, C Bobeth, et al. The Belle II Physics Book. *Progress of Theoretical and Experimental Physics*, 2019(12), Dec 2019. ISSN 2050-3911. doi: 10.1093/ptep/ptz106. URL <http://dx.doi.org/10.1093/ptep/ptz106>.
- [24] A. J. Bevan et al. The Physics of the B Factories. *The European Physical Journal C*,

- 74(11), Nov 2014. ISSN 1434-6052. doi: 10.1140/epjc/s10052-014-3026-9. URL <http://dx.doi.org/10.1140/epjc/s10052-014-3026-9>.
- [25] Savino Longo and J. Michael Roney. Hadronic vs Electromagnetic Pulse Shape Discrimination in CsI(Tl) for High Energy Physics Experiments. *Journal of Instrumentation*, 13(03):P03018–P03018, 2018. doi: 10.1088/1748-0221/13/03/P03018.
- [26] Thomas D. McLean *et al.* CHELSI: Recent developments in the design and performance of a high-energy neutron spectrometer. *Nuclear Instruments and Methods in Physics Research Section A: Accelerators, Spectrometers, Detectors and Associated Equipment*, 562(2):793–796, 2006. ISSN 0168-9002. doi: <https://doi.org/10.1016/j.nima.2006.02.057>. URL <https://www.sciencedirect.com/science/article/pii/S016890020600297X>. Proceedings of the 7th International Conference on Accelerator Applications.
- [27] Saint Gobain. Pure CsI Data Sheet. https://www.crystals.saint-gobain.com/sites/imdf.crystals.com/files/documents/csi-pure-material-data-sheet_69770.pdf, . Accessed: 2021-09-14.
- [28] Saint Gobain. CsI(Tl) Data Sheet. https://www.crystals.saint-gobain.com/sites/imdf.crystals.com/files/documents/csitl-and-na-material-data-sheet_69771.pdf, . Accessed: 2021-09-14.
- [29] Hamamatsu. PMT R329-02, Data Sheet. <https://www.hamamatsu.com/eu/en/product/type/R329-02/index.html>. Accessed: 2021-09-14.
- [30] CAEN. DT5730. <https://www.caen.it/products/dt5730/>. Accessed: 2021-09-14.
- [31] Reichelt Elektronik Magazine. Measure temperature and air humidity with the Arduino Uno. <https://www.reichelt.com/magazin/en/measure-temperature-air-humidity-arduino-uno/>. Accessed: 2021-09-14.

- [32] Taiee Liang, Albrecht Leuschner et al. Dose rates calculations from electron beam losses on XS1 dump at XFEL. May 2021. Internal report, DESY D3-123.
- [33] Winfried Decking, Frank Brinker, Lars Fröhlich, Raimund Kammering, Torsten Limberg, Shan Liu, Dirk Nölle, Mathieu Omet, Matthias Scholz, and Thomas Wamsat. Status of the European XFEL. page TUPRB020, 2019. doi: 10.18429/JACoW-IPAC2019-TUPRB020.
- [34] Georg Fehrenbacher et al. Spectrometry behind concrete shielding for neutrons produced by 400 mev/u 12c ions impinging on a thick graphite target. 2004. In: Proceedings of the International Radiation Protection Association, IRPA-11-Congress, Madrid.
- [35] Albrecht Leuschner. Dose rate measurements around the electron extraction at FLASH. 2015. https://radsynch15.desy.de/sites/site_radsynch15/content/e268576/e268578/infoboxContent268622/Session03_radsynch15_Leuschner.pdf.
- [36] S. Agostinelli *et al.* Geant4—a simulation toolkit. *Nuclear Instruments and Methods in Physics Research Section A: Accelerators, Spectrometers, Detectors and Associated Equipment*, 506(3):250–303, 2003. ISSN 0168-9002. doi: [https://doi.org/10.1016/S0168-9002\(03\)01368-8](https://doi.org/10.1016/S0168-9002(03)01368-8). URL <https://www.sciencedirect.com/science/article/pii/S0168900203013688>.
- [37] Geant4 Collaboration. Geant4—Book for Application Developers. <https://geant4-userdoc.web.cern.ch/UsersGuides/ForApplicationDeveloper/html/index.html>. Accessed: 2021-09-28.
- [38] Refractive index of CsI. <https://refractiveindex.info/?shelf=main&book=CsI&page=Li>. Accessed: 2021-10-11.
- [39] Physics Simulation Packages: CRY. <https://nuclear.llnl.gov/simulation/main.html>. Accessed: 2021-09-28.

- [40] Chris Hagmann et al. Monte Carlo Simulation of Proton-induced Cosmic-ray Cascades in the Atmosphere. January 2007. https://nuclear.llnl.gov/simulation/doc_cry_v1.7/cry_physics.pdf.
- [41] Caleb W. Fink and Samuel L. Watkins. QETpy. <https://doi.org/10.5281/zenodo.5104856>, July 2021.
- [42] scipy Documentation: `scipy.signal.find_peaks`. https://docs.scipy.org/doc/scipy/reference/generated/scipy.signal.find_peaks.html, . Accessed: 2021-09-22.
- [43] scipy Documentation: `scipy.signal.peak_prominences`. https://docs.scipy.org/doc/scipy/reference/generated/scipy.signal.peak_prominences.html#scipy.signal.peak_prominences, . Accessed: 2021-09-22.
- [44] Radioactivity: Potassium-40. https://www.radioactivity.eu.com/site/pages/Potassium_40.htm. Accessed: 2021-10-07.
- [45] Nguyen V. H. Viet, M. Nomachi, K. Takahisa, T. Shima, B. T. Khai, R. Takaishi, and K. Miyamoto. Pulse Shape Discrimination of CsI(Tl) With a Photomultiplier Tube and Multipixel Photon Counters. *IEEE Trans. Nucl. Sci.*, 68(2):203–210, 2020. doi: 10.1109/TNS.2020.3047615.

Acknowledgements

I would like to thank Prof. Dr. Torben Ferber for giving me the opportunity to work on this project, for teaching me about all kinds of scientific work and for all the guidance and support through this past year. Thanks to my co-supervisor Dr. Savino Longo for teaching me about physics and helping me through every step of this thesis. I am grateful to both of them for letting me benefit from their expertise, experience and knowledge that they shared with me. Special thanks to my supervisor Prof. Dr. Kerstin Tackmann for making it possible for me to work on this thesis.

Thanks to team of DESY D3 for allowing us to do measurements at XFEL. Thanks to Albrecht Leuchner for teaching me about neutron interactions, for giving us access to their detectors and for personally taking us to the measurement location.

Thanks to Sukeerthi Dharani and Belina von Krosigk from the SuperCDMS group for cooperating with us on this project. Thanks for the amazing analysis Sukeerthi performed with the data recorded with this setup. Thanks for all the help with my code for this analysis. Thanks for teaching me and offering such helpful comments on my work.

Thanks to Kasten Gadow and the team of DESY-FH technicians for building the housing for our setup and helping with the experimental setup. Thanks to Thorsten Külper and everyone at the FH E-Lab for helping us with electronics about the setup. Thanks to Andreas Gellrich for helping me with IT stuff.

Thanks to Sam for all the coding related help and for being a great teacher to us students. Thanks to the PXD guys Anselm and Arthur for all their hardware related-help

and for their support. Thanks to Henrikas and Sascha for their help with the data analysis. I also want to thank you guys for being there with me from beginning until the end.

Thanks to Alberto, Fillippo, Maria, Michel, Micheal, Navid, Sam, Sally, Stella and really everyone in the DESY Belle II group. Thank you all for letting me be part of this group.

Huge thanks to my friends and family for all their love and support. I am and always will be very grateful to all of you.

Eidesstattliche Versicherung

Hiermit versichere ich an Eides statt, dass ich die vorliegende Arbeit selbstständig und ohne fremde Hilfe angefertigt und mich anderer als der im beigefügten Verzeichnis angegebenen Hilfsmittel nicht bedient habe. Alle Stellen, die wörtlich oder sinngemäß aus Veröffentlichungen entnommen wurden, sind als solche kenntlich gemacht. Ich versichere weiterhin, dass ich die Arbeit vorher nicht in einem anderen Prüfungsverfahren eingereicht habe und die eingereichte schriftliche Fassung der auf dem elektronischen Speichermedium entspricht.

Ich bin mit einer Einstellung in den Bestand der Bibliothek des Fachbereiches einverstanden.

Hamburg, den _____ Unterschrift: _____